

Observations and Modeling of Tsunamis from Genesis to Inundation Using  
Contemporary Methods

by

Sean R Santellanes

A dissertation accepted and approved in partial fulfillment of the  
requirements for the degree of  
Doctor of Philosophy  
in Earth Sciences

Dissertation Committee:

Diego Melgar, Chair and Advisor

Valerie Sahakian, Core Member

Dave Sutherland, Core Member

Johnny Ryan, Institutional Representative

University of Oregon

Fall 2024

© 2024 Sean R Santellanes  
This work is openly licensed via  
**CC BY-NC-ND 4.0.**

## DISSERTATION ABSTRACT

Sean R Santellanes

Doctor of Philosophy in Earth Sciences

Fall 2024

Title: Observations and Modeling of Tsunamis from Genesis to Inundation Using Contemporary Methods

This dissertation explores broadly the science of tsunamis from genesis to inundation. Tsunami science has been able to produce accurate forecasts of tsunami first arrival and propagation from advancements in deep ocean monitoring and high resolution bathymetry and topography. However, it remains in its infancy compared to its sister discipline — seismology, owing to the lack and sparse instrumentation in the offshore, deep ocean environment. In addition, the lack of understanding of how turbulence and anthropogenic structures affects inundation leaves the most destructive part of the tsunami life cycle remarkably unconstrained.

This dissertation seeks to understand and better constrain several aspects of the tsunami life cycle. In this dissertation, I present an analysis of the tsunami source of the 2022 Hunga Tonga global tsunami, showing from open ocean and coastal sea level stations, the coupled atmospheric conditions that propagated the tsunami globally. Further, I show that the background open ocean tsunami spectrum, vital for understanding tsunami amplification from open ocean to the coast, can experience changes due to atmospherically induced infragravity waves. Next, I present an analysis of the 2020 Sand Point tsunami source. This work shows a novel method for including open ocean instrumentation with geodetic and seismological data to produce finite fault models capable of detecting "hidden" subduction zone events. Finally, I present an analysis of the differences of inundation between homogeneous and heterogeneous tsunami sources along the Cascadia Subduction Zone. This work highlights the importance of using heterogeneous tsunami sources for understanding how inundation may affect the anthropogenic environment. This work may lay the groundwork for probabilistic-based tsunami evacuation rather than relying on deterministic, homogeneous tsunami sources.

This dissertation includes previously published (unpublished) co-authored material.

## CURRICULUM VITAE

NAME OF AUTHOR: Sean R Santellanes

### GRADUATE AND UNDERGRADUATE SCHOOLS ATTENDED:

University of Oregon, Eugene, OR, USA  
Pennsylvania State University, State College, PA, USA  
The University of Texas at Austin, Austin, TX, USA

### DEGREES AWARDED:

Doctor of Philosophy, Earth Sciences, 2024, University of Oregon  
Master of Science, Meteorology and Atmospheric Science, 2020,  
Pennsylvania State University  
Bachelor of Science, Physics, 2017, The University of Texas at Austin

### AREAS OF SPECIAL INTEREST:

Tsunamis  
Earthquakes  
Data Science

### PROFESSIONAL EXPERIENCE:

Graduate Employee, University of Oregon, 2019-2024  
Year-Round Intern, Sandia National Laboratories, 2022-2024  
Alumni Volunteer, GeoFORCE Texas, The University of Texas at Austin,  
2023-2024  
Intern, United States Geological Survey, 2014-2015

### GRANTS, AWARDS AND HONORS:

### PUBLICATIONS:

Santellanes, S. R., Young, G. S., Stensrud, D. J., Kumjian, M. R., & Pan, Y. (2021). Environmental conditions associated with horizontal convective rolls, cellular convection, and no organized circulations. *Monthly Weather Review*, 149(5), 1305-1316.

Santellanes, S. R., Ruiz-Angulo, A., & Melgar, D. (2023). Tsunami waveform stacking and complex tsunami forcings from the Hunga-Tonga eruption. *Pure and Applied Geophysics*, 180(6), 1861-1875.

## ACKNOWLEDGEMENTS

The work done in this dissertation would not have been possible without the help and advice of many people. First, I want to thank my advisor, Diego Melgar, for his endless patience and guidance with the various stuff that came from life and science during the course of this degree. Next, I would like to thank my committee and co-authors Valerie Sahakian, Dave Sutherland, and Dara Goldberg for their help and patience, especially with helping a meteorologist understanding the conventions of seismology. I would like to thank my friends and colleagues that I have made over the course of my degree, specifically, Avigyan Chatterjee, Avery Conner, Kate Scholz, Christina Cauly, Sydney Dybing, Sandia Infrasound Crew, Walker Building 406, and Big Timber Running Club. Additionally, I would like to thank friends and colleagues in the Melgar group, other graduate students, and the Earth Sci front office. And lastly, Sitka for being a good emotional support dog.

Dedicated to friends and family who died along the way...

## TABLE OF CONTENTS

Chapter	Page
I. INTRODUCTION . . . . .	25
II. TSUNAMI WAVEFORM STACKING AND COMPLEX TSUNAMI FORCINGS FROM THE HUNGA-TONGA ERUPTION . . . . .	29
2.1. Introduction . . . . .	31
2.2. Data and Methods . . . . .	37
2.3. Results and Discussion . . . . .	45
2.3.1. Moveout at 315 m/s . . . . .	47
2.3.2. Moveout at 205 m/s . . . . .	49
2.3.3. Moveout at 155 m/s . . . . .	51
2.3.4. Other effects and observations . . . . .	54
2.3.5. Caveats to the interpretation . . . . .	54
2.3.6. Hazards implications . . . . .	55
2.4. Conclusion . . . . .	57
2.5. Data and Resources . . . . .	58
2.6. Declaration of competing interests . . . . .	58
2.7. Acknowledgements . . . . .	58
III. CONTEMPORARY MEASUREMENTS OF THE BACKGROUND OPEN OCEAN TSUNAMI SPECTRUM USING THE DEEP-OCEAN ASSESSMENT AND REPORTING OF TSUNAMI (DART) STATIONS . . . . .	61
3.1. Introduction . . . . .	62
3.2. Data and Methods . . . . .	66

Chapter	Page
3.2.1. The DART station system and PPSD measurements of the BOOTS . . . . .	66
3.2.2. Measuring temporal variations in the BOOTS . . . . .	67
3.2.3. Measurement of IGWs with DART stations . . . . .	69
3.3. Results . . . . .	70
3.3.1. PPSD behavior of the BOOTS . . . . .	70
3.3.2. Spatiotemporal variations in the BOOTS . . . . .	72
3.3.2.1. Temporal variations in the BOOTS . . . . .	73
3.3.2.2. Spatial variations of power in the BOOTS . . . . .	75
3.4. Infragravity waves in the BOOTS . . . . .	78
3.4.1. Spatiotemporal Effects of IGWs . . . . .	78
3.5. Data artifacts in the BOOTS . . . . .	80
3.5.1. Tsunami signals . . . . .	80
3.5.2. Bifurcation of PPSD in short periods . . . . .	83
3.5.3. Meteorological impacts on the BOOTS . . . . .	85
3.6. Discussion . . . . .	89
3.6.1. The magnitude of the BOOTS slope . . . . .	89
3.6.2. Implications of meteorological impacts on the BOOTS . . . . .	90
3.6.3. Implications of a spatiotemporally varying BOOTS . . . . .	92
3.7. Conclusion . . . . .	93
3.8. Data availability . . . . .	94
3.9. Acknowledgements . . . . .	95
IV. AN UNEXPLAINED TSUNAMI: WAS THERE MEGATHRUST SLIP DURING THE 2020 MW7.6 SAND POINT, ALASKA, EARTHQUAKE? . . . . .	97
4.1. Introduction . . . . .	98

Chapter	Page
4.2. The incompatibility of a strike-slip source . . . . .	101
4.2.1. USGS model . . . . .	101
4.2.2. Joint model of on-shore and off-shore observations . . . . .	105
4.3. Deformation requirements of the observed tsunami . . . . .	107
4.4. Allowing coeval megathrust and strike slip rupture . . . . .	111
4.4.1. Megathrust rupture initiation . . . . .	111
4.4.2. Full Kinematic Rupture Modeling . . . . .	114
4.5. Discussion . . . . .	121
4.5.1. Hidden megathrust rupture . . . . .	121
4.5.2. Potential Submarine Landslide . . . . .	123
4.5.3. Regional context and hazard considerations . . . . .	124
4.6. Conclusion . . . . .	129
4.7. Acknowledgements . . . . .	130
4.8. Data and code availability . . . . .	130
V. COMPARISONS OF TSUNAMI INUNDATION BETWEEN HOMOGENEOUS AND HETEROGENEOUS EARTHQUAKE SOURCES AT SELECT SITES FOR THE CASCADIA SUBDUCTION ZONE. . . . .	133
5.1. Motivation . . . . .	133
5.1.1. Source complexity and coupling in local tsunami hazard estimates . . . . .	137
5.1.2. Are the ASCE 7-22 and DOGAMI "t-shirt" models still reasonable sources for hazards estimates? . . . . .	139
5.2. Data and Methods . . . . .	142
5.2.1. Stochastic modeling of geodetically constrained ruptures . . . . .	142
5.2.2. Tsunami modeling . . . . .	144
5.2.3. Comparisons of hazards between homogeneous and heterogeneous ruptures . . . . .	146

Chapter	Page
5.3. Results . . . . .	148
5.3.1. Mean tsunami inundation behavior . . . . .	149
5.3.2. Differences between homogeneous and heterogeneous ruptures. . . . .	153
5.3.3. Tsunami hazard maps . . . . .	156
5.4. Discussion . . . . .	157
5.4.1. Differences of homogeneous and heterogeneous models . . . . .	157
5.4.2. Moving towards a probabilistic maximum considered tsunami . . . . .	161
5.5. Conclusion . . . . .	163
VI. CONCLUSION . . . . .	165
REFERENCES CITED . . . . .	168

## LIST OF FIGURES

Figure		Page
1.	<p>DART buoys and tide gauges analyzed in this work. DART buoys that were operable with data from only the Tohoku tsunami are shown in neon green. DART buoys that were operable with data for both Tohoku and Tonga are shown in dark orange. DART buoys that were operable with data for only the Tonga tsunami are shown in white. Tide gauges used in this analysis are shown in red. The focal mechanism of the Mw 9.1 Tohoku earthquake is plotted along with the location of the HTHH volcano in white. Atmospheric barometer stations are plotted in teal. . . . .</p>	30
2.	<p>Schematic diagram showing the 4 potential tsunamigenic source mechanisms from the eruption of HTHH. From left to right, a flank collapse or explosion would have a tsunami propagation speed of <math>\sim 220</math> m s<sup>-1</sup>. An internal gravity wave would have a propagation speed of <math>\sim 150</math> m s<sup>-1</sup>. A Lamb wave would have a propagation speed of <math>\sim 310</math> m s<sup>-1</sup>. Lastly, an acoustic wave would have a propagation speed of <math>\sim 330</math> m s<sup>-1</sup>. . . . .</p>	35
3.	<p>(a) First arrival amplitudes and peak amplitudes in meters recorded at 22 DART buoys from the M9 Tohoku-Oki tsunami and 34 DART buoys from HTHH. (b) Peak amplitudes in meters recorded at 27 tide gauges from the M9 Tohoku-Oki tsunami and 82 tide gauges from HTHH with clear and obvious tsunami signatures. The 403 tide gauges from Carvajal, Sepúlveda, Gubler, and Garreaud (2022) are plotted to compare our dataset with their results. Only first arrival amplitudes are plotted. . . . .</p>	36

4. a.) Record section of the DART data from the HTHH tsunami. Red line denotes the speed of the first arrival seen at the DARTs. The blue line denotes the speed of potential secondary arrivals. b.) Record section of tide gauge data from the HTHH tsunami. The red line denotes the hypothetical Lamb wave arrival at the tide gauge stations. The blue line denotes the second arrival potentially seen the tide gauge stations. The data are shown for as long as 15 s and 1 min data were available. The tsunami amplitude waveforms are scaled individually to better appreciate the arrivals. . . . . 39

5. Amplitude stack plots with time delays in hours. The plots show the concentration of amplitudes in the 7 azimuth gates and full azimuth range with available DART data. 305 m/s moveout speeds are discernible in all but one – 135-180. 155 m/s moveout speeds are discernible in 3: 90-135, 135-180, 225-270. Moveout speeds in typical tsunami velocities are observable in all azimuth gates. The amplitudes are normalized by the number of DARTs in their respective azimuth gates. . . . . 42

6. Amplitude stack plots with time delays in hours. The plots show the concentration of amplitudes in the 7 azimuth gates and full azimuth range with available DART data. 305 m/s moveout speeds are discernible in all but one – 135-180. 155 m/s moveout speeds are discernible in 3: 90-135, 135-180, 225-270. Moveout speeds in typical tsunami velocities are observable in all azimuth gates. The amplitudes are normalized by the number of DARTs in their respective azimuth gates. . . . . 44

7. a.) The amplitude stack plot of normalized DART waveforms combined assuming a velocity of 215 m s-1. b.) The amplitude stack plot of normalized DART waveforms combined assuming a velocity of 305 m s-1. c.) Peak amplitudes at toffset=0 for the averaged, normalized DART stacked waveforms for velocities from 100 - 400 m s-1 for various azimuth ranges. All azimuths contain 35 stations, 0-45 11 stations, 270-315 8 stations, and 315-360 6 stations. d.) The same as c.) but for tide gauge data. There are 114 stations for all azimuths, 0-45 1 station, 270-315 7 stations, and 315-360 14 stations. . . . . 46

Figure	Page
8. Examples of multi-taper spectral analysis Wigner-Ville spectrograms of equidistant DART buoys. a.) and b.) are about 12 from their respective sources. C.), d.) and e.) are about 95-121 from their respective sources. A.) and c.) show the dispersion of tsunami waves as they move away from the earthquake source. B.), d.) and e.) show how little dispersion there is with the tsunami source from HTHH with the associated Lamb wave front. 21413 is 700 NM ESE of Tokyo, JP. 32412 is 1000 NM W of Lima, Peru. 51425 is 370 NM NW of Apia, Samoa. 42409 is 247 NM S of New Orleans, LA, USA. . . . .	49
9. First arrival amplitudes and peak amplitudes in meters recorded at 22 DART buoys from the M9 Tohoku-Oki tsunami and 34 DART buoys from HTHH are converted to pressure amplitudes via equations 2 and 3. We compare these calculated values to terrestrial barometer station peak amplitudes from 7 coastal barometer stations. . . . .	52
10. Station up-time graphs that show the time spans of data used for each DART in this study. . . . .	64
11. Crosses mark the locations of the DART stations used in this study. DARTs 21420 and 46407 are highlighted because they are emblematic (21320) and non-emblematic (46407) to the reference power law of $\omega^{-2}$ . BOOTS slope values. . . . .	67
12. a.) Probabilistic Power Spectral Density (PPSD) plot for DART 21420 — emblematic of behavior that follows the reference power law of $\omega^{-2}$ . Amplitudes corresponding to noise levels of 1 cm, 0.1 cm, and 0.01 cm are shown as dashed, black lines. Periods corresponding to 120 s, 240 s, and 800 s are delineated by solid, orange lines. b.) PPSD for DART 46407 — emblematic of behavior that does not follow the reference power law of $\omega^{-2}$ . Amplitudes corresponding to noise levels of 1 cm, 0.1 cm, and 0.01 cm are shown as dashed, black lines. Periods corresponding to 120 s, 250 s, and 800 s are delineated by solid, orange lines. . . . .	71
13. a.) 21420 time-series of BOOTS slope (blue) and intercept (orange). b.) 46407 time-series of BOOTS slope (blue) and intercept (orange). Period of low-quality data, resulting in no values for either parameter, is shown in red. . . . .	72

Figure	Page
14. a.) Mean slope of the BOOTS across the Pacific basin for each station’s entire temporal coverage. Color of the circle corresponds to the mean value of the BOOTS slope. Circle size corresponds to the standard deviation of the slop. b.) Intercept of the BOOTS across the Pacific basin. Color of the circle corresponds to the mean value of the intercept. Circle size corresponds to the standard deviation of the intercept. . . .	74
15. a.) Median power in dB at a period of 120 s. Top panel is median power during JJA, and bottom panel is median power during DJF. b.) Median power in dB at a period of 250 s. c.) Median power in dB at a period of 800 s. . . . .	76
16. Infragravity wave heights for the time periods of JJA (red circles) and DJF (green circles). DART locations are shown as black dots. . . . .	79
17. The 2020 Simeonof rupture zone from Crowell and Melgar (2020) is shown in black, the 2021 Chignik rupture zone from the USGS-National Earthquake Information Center (NEIC) finite fault model for the event is shown in dark blue, and the rupture area for the July 15, 2023, Sand Point earthquake from the USGS-NEIC finite fault model is shown in aquamarine (U. S. Geological Survey, 2017). The surface projection of the strike-slip plane associated with the 2020 Sand Point earthquake is delineated by a dashed red line. . . . .	81
18. DART 46407 PPSD. The 2020 M7.8 Simeonof earthquake is shown by a dash-dot-dot magenta line (UTC Day July 22, 2020). The 2020 M7.6 Sand Point earthquake is shown in blue (UTC Day October 19, 2020) and by a dash-dot crimson line (UTC Day October 20, 2020). The 2021 Chignik earthquake is shown by a dashed green line (UTC Day July 21, 2021). . . . .	82

19. a.) PPSD for DART 46407. High noise location (red), low noise location (dash-dot-dot blue), meteorological event (dash-dot green), and tsunami (July 22, 2021 Chignik earthquake, dash magenta) PSDs are plotted for their respective occurrences. Arrows point to their respective phenomena in panels b.) and c.). b.) Meteorological event that occurred on November 16, 2020, at 0600 UTC which produced noise above the 10th percentile in the BOOTS. Maximum/Composite radar reflectivity from the 0600 UTC High Resolution Rapid Refresh (HRRR) model is shown. c.) Location of DART 46407 at a high noise location (UTC Day May 17, 2011, red x) and a low noise location (UTC day July 7, 2021, black x). . . . . 84
20. a.) ECMWF wave height model at  $0.5^\circ$  resolution for February 10, 2022 at 12 UTC. DART 46407 is shown by a black dot. b.) ECMWF model at  $0.5^\circ$  resolution for February 10, 2022 at 12 UTC. Geopotential height at 850 mbar is plotted at 50 m contours. 10 m wind is shown by filled contours. c.) PPSD for DART 46407 for the meteorological event signal during August 13, 2021. The signal is shown by the dashed green line. . . . . 87
21. a.) PPSD for DART 43413. Meteorological event signal for August 13, 2021 is shown by the dashed green line. b.) GEFS model at  $0.5^\circ$  resolution for August 13, 2021 at 12 UTC. 10 m wind is shown to visualize the wind field of the tropical systems. Pressure reduced to mean sea level (MSL) pressure is shown by the black contours. Contours are plotted at 2 mbar intervals. DART 43413 is shown by a white dot. The approximate locations of tropical storm Kevin and Hurricane Linda's cores are shown by white dots. . . . . 88

22. The study area, offshore of the Alaskan peninsula. Demarcations for the Sanak, Shumagin, and Semidi segments from Liu et al. (2020) are shown with dashed black lines. The 2020 Simeonof rupture zone is shown in black (Crowell & Melgar, 2020), the 2021 Chignik rupture zone is shown in dark blue (USGS Earthquake Hazards Program, 2017), and the July 2023 Sand Point rupture zone is shown in aquamarine. The W-phase centroid moment tensors (WCMT) for Simeonof, Chignik, and July 2023 Sand Point are shown in the same colors as their rupture zones. The surface projection of the USGS-NEIC finite fault plane for the 2020 Sand Point earthquake is delineated by a dashed red line. The epicenter and WCMT for the 2020 Sand Point earthquake are shown in gold. The King Cove (KING) and Sand Point (SAND) coastal sea level stations are shown as red triangles. DART stations are shown as light blue triangles. GNSS station AC12 (yellow square) is shown to have undergone 10 cm of subsidence during the 2020 Sand Point earthquake. The inset shows the locations of the coastal sea level stations in Hawai'i and the outline of the main study area in blue. . . . . 99

23. a.) Map showing the vertical deformation resulting from the USGS-NEIC finite fault model (model U0). The dashed black line from A-A' is the surface projection of the causative fault plane, as inferred by the USGS-NEIC. The hypocenter (star) and WCMT are shown in gold. b.) USGS-NEIC finite fault solution. c.) the observed (black) and modeled (red) tsunami waveforms at coastal sea level stations. d.) the observed (black) and modeled (red) tsunami waveforms at DART stations. DART 46403 is shown with slightly muted colors to indicate that it was impacted by Rayleigh wave contamination. . . . . 102

24. The results for model S1. a.) Map of study area showing seafloor deformation implied by model S1a constrained to USGS-NEIC magnitude. Line A-A' shows the surface projection of the strike-slip geometry, with cross section A-A' below showing the modeled slip distribution along the strike-slip geometry. Model S1a is constrained to a magnitude of Mw 7.6. b.) Map of study area showing seafloor deformation implied by model S1b without any magnitude constraint, resulting in slip distribution equivalent to Mw 8.0. Line A-A' shows the surface projection of the strike-slip geometry, with cross section A-A' below showing the modeled slip distribution along the strike-slip geometry. c.) Observed tsunami waveforms (black) with resulting synthetic waveforms from models in (a.) and (b.) shown in red and blue, respectively. . . . . 108

25. The hydrodynamic model (model H0) results. a.) Region map with the 2020 Simeonof and 2021 Chignik rupture zones and associated WCMTs shown in black and blue, respectively (Crowell & Melgar, 2020; U. S. Geological Survey, 2017). The surface projection of the USGS-NEIC finite fault plane for the 2020 Sand Point earthquake is delineated by a dashed red line. The epicenter and WCMT for the 2020 Sand Point earthquake are shown in gold. The King cove (KING) and Sand Point (SAND) sea level stations are shown as red triangles. DART stations are shown as light blue triangles. GNSS station AC12 location shown by yellow square. The red dashed line shows the surface trace for the W-Phase nodal plane used in the USGS-NEIC finite fault model. The top inset shows the locations of the coastal sea level stations in Hawai'i and the outline of the main study area in blue. The bottom inset shows the modeled seafloor deformation (model H0). The black outline denotes an area where a suspected submarine landslide may have occurred, based on the classic dipole sea surface deformation pattern. b.) The tsunami waveforms (observations in black, model synthetics in red) from the coastal sea level stations. Modeled waveforms for Hilo and Kawaehai (KAWA) are shifted by 6.38 min and 2.13 min, respectively, for temporal consistency with the observed data. c.) The tsunami waveforms (observations in black, model synthetics in red) from the DART stations. Gray boxes in a.) and b.) outline the portions of the coastal sea level and DART observations used in the tsunami inversion. . . . . 110
26. Potential megathrust rupture nucleation points. a.) Map view of potential nucleation points (orange triangles), including event hypocenter (N0) and nine additional potential nucleation points (N1-N9). Preferred nucleation point, N3, is shown in blue along with the direction and best fitting speed of propagation, 1 km/s. The 2020 Simeonof and 2021 Chignik rupture zones are shown in black and blue, respectively (Crowell & Melgar, 2020; U. S. Geological Survey, 2017) b.) The weighted RMSE for static triggering at nucleation point N0 compared to RMSEs of nucleation points N1-N9 for four different rupture velocities. . . . . 113

27. Model S2 results. a.) Results of model S2a. Dashed black line delineates the portion of the megathrust considered in the inversion. Magenta contour and shaded area shows the  $\geq 1$  m rupture patch of the inversion rupture zone. Dashed line A-A' shows the surface projection of the strike-slip plane, with slip distribution on the strike-slip plane shown below. The maximum allowable rupture speed is 1.25 km/s for the megathrust and 3.00 km/s for the strike-slip plane. b.) Results of preferred model S2b (nucleation point N3 with maximum allowable rupture velocity of 1 km/s). Dashed black line delineates the subfaults of the megathrust allowed to partake in the inversion. Magenta contour and shaded area shows the  $>1$  m rupture patch of the inversion rupture zone. Nucleation point 3 is shown as a blue inverted triangle. A-A' is the surface projection of the strike-slip plane from the USGS-NEIC WCMT. c.) The observed tsunami waveforms (black) compared to the modeled tsunami waveforms from models S2a and S2b in red and blue, respectively. . . . . 115
28. The associated moment tensors (MTs) for the strike-slip segment and megathrust segment for the four kinematic inversions and their composite MTs. The Kagan angle between each composite MT and the USGS-NEIC WCMT are given for each inversion model. The USGS-NEIC MT is shown for visual comparison. . . . . 117

29. Model K3 results. a.) Map showing the geographical distribution of slip along the megathrust as well as the strike-slip geometry used in inversion K3. Black star show the hypocenter for the strike-slip and a blue star shows the nucleation point for the megathrust. Red lines indicate the updip edge of the two fault orientations. b.) Smoothed slip distribution and rupture time contours for the strike-slip segment. Small gray arrows indicate rake direction, scaled by amplitude of slip. Black star shows the hypocentral location. c.) Same as b.) but for the megathrust segment. Note that the rupture time contours start 29.5 s later, as we assume delayed slip to nucleation point N3. d.) The source time function for the published USGS-NEIC finite fault product (black; USGS Earthquake Hazards Program, 2017), the strike-slip segment of model K3 (green), the megathrust portion of model K3 (yellow), and the total source time function of model K3 (magenta) e.) Observed (black) and model K3 synthetic (red) tsunami waveforms. . . . . 119
30. The observed tsunami waveforms (black) compared to synthetic tsunami waveforms (red) resulting from the combination of kinematic model K3 and a submarine landslide signal obtained from model H0. . . . . 125
31. The proposed rupture zone for the 2020 Sand Point megathrust is shown in gold. The 2020 Simeonof rupture zone from Crowell and Melgar (2020) is shown in black, the 2021 Chignik rupture zone from the USGS-NEIC finite fault model for the event is shown in dark blue, and the rupture area for the July 15, 2023, Sand Point earthquake from the USGS-NEIC finite fault model is shown in aquamarine. The surface projection of the strike-slip plane associated with the 2020 Sand Point earthquake is delineated by a dashed red line. The King cove (KING) and Sand Point (SAND) sea level stations are shown in red. DART stations are shown in light blue. The amount of subsidence at GNSS station AC12 (yellow square) for the 2020 Sand Point earthquake is shown to be 10 cm. The inset shows the locations of the coastal sea level stations in Hawai'i. The blue box shows the location of the main study area. . . . . 128

Figure	Page
32. Map of the study area. Insets show the areas of interest that were used for modeling of tsunami inundation. Black arrows point from the inset to the locations of the areas of interest on the main map. CSZ is denoted by the red subduction zone symbols. The XXL1 "t-shirt" vertical deformation model is shown by the polar plot. Contours are plotted at 5 m intervals. . . . .	140
33. Heterogeneous slip and vertical deformation maps for the four geodetic families used in this study. $M_w$ 9.1 source ruptures for a.) 1 cm/yr, b) Gamma, c) Gauss, and d) Li geodetic models. Subduction zone interface geometry comes from Hayes et al. (2018). . . . .	142
34. Violin plots of the mean tsunami inundation behavior for each geodetic model and all models. Probability distribution functions shows distribution of the mean of all inundated cells for each scenario (see Figures 37 and 38 for approximate inundated cell extent). Red dashed lines delineate the 25 <sup>th</sup> and 75 <sup>th</sup> percentiles. Solid black lines delineates the 50 <sup>th</sup> percentile. Blue line and arrow show the mean value of all inundated grid cells for the XL1 scenario. Likewise, red line and arrow show the mean value of all inundated grid cells for the L1 scenario. The XYZ line and arrow show the mean value of all inundated grid cells for the M3 scenario. Violin plots are shown for a) Ocean Shores, WA; b) Newport, OR; and c) Crescent City, CA. . . . .	150
35. Maps that show the L1 percentile of inundation for each grid cell for a) Ocean Shores, WA; b) Newport, OR; and c) Crescent City, CA. Black lines denote the official tsunami evacuation lines used for by the states of Washington, Oregon, and California. Streets and geographic information tiles are provided by the USGS. . . . .	151
36. Maps that show the XL1 percentile of inundation for each grid cell for a) Ocean Shores, WA; b) Newport, OR; and c) Crescent City, CA. Black lines denote the official tsunami evacuation lines used for by the states of Washington, Oregon, and California. Streets and geographic information tiles are provided by the USGS. . . . .	152

Figure	Page
37. Maps that show the L1 homogeneous where "wet" is $\geq 30$ cm and dry is $< 30$ cm (a)), average of 200 heterogeneous where "wet" is $\geq 30$ cm and dry is $< 30$ cm (b)), and difference between "wet" and "dry" grid cells for Ocean Shores, WA; Newport, OR; and Crescent City, CA. Black lines denote the official tsunami evacuation lines used for by the states of Washington, Oregon, and California. Streets and geographic information tiles are provided by the USGS. . . . .	154
38. Maps that show the XL1 homogeneous where "wet" is $\geq 30$ cm and dry is $< 30$ cm (a)), average of 200 heterogeneous where "wet" is $\geq 30$ cm and dry is $< 30$ cm (b)), and difference between "wet" and "dry" grid cells of a) and b) for Ocean Shores, WA; Newport, OR; and Crescent City, CA. Black lines denote the official tsunami evacuation lines used for by the states of Washington, Oregon, and California. Streets and geographic information tiles are provided by the USGS. . . . .	155
39. Maps that show the 1-in-50, 1-in-100, and 1-in-2475 year exceedences for the L-like heterogeneous sources for a) Ocean Shores, WA; b) Newport, OR; and c) Crescent City, CA. Black lines denote the official tsunami evacuation lines used for by the states of Washington, Oregon, and California. Streets and geographic information tiles are provided by the USGS. . . . .	158
40. Maps that show the 1-in-50, 1-in-100, and 1-in-2475 year exceedences for the XL-like heterogeneous sources for a) Ocean Shores, WA; b) Newport, OR; and c) Crescent City, CA. Black lines denote the official tsunami evacuation lines used for by the states of Washington, Oregon, and California. Streets and geographic information tiles are provided by the USGS. . . . .	159

## LIST OF TABLES

Table	Page
1. The attributes of the inversions considered in this study. SS is strike-slip, MT is megathrust, CSLS is coastal sea level station, SGNSS is static GNSS, HRGNSS is high-rate GNSS, STR is strong motion accelerometer. * denotes unweighted RMSE and †denotes weighted RMSE. . . . .	103
2. Jaccard similarity indices for for Ocean Shores, Newport, and Crescent City of the homogeneous and heterogeneous spatial rasters of "wet" and "dry" tsunami inundation. . . . .	156

# CHAPTER I

## INTRODUCTION

Tsunamis have been among the deadliest natural hazards of the 21<sup>st</sup> century. Regardless of country development status, tsunamis have been able to exact high amounts of casualties from > 230,000 from the 2004 Sumatra tsunami to the > 22,000 from the 2011 Tohoku-Oki tsunami. Differing reasons have been ascribed as to why these earthquakes exacted such high tolls. This dissertation focuses on three such reasons: (1) lack of constraint of the open-ocean background state, (2) source mechanism complexity (non-seismic and seismic sources), and (3) varying inundation behavior.

This dissertation seeks to test the long-held assumption that the background open ocean tsunami spectrum maintains a constant spectral slope of  $\omega^{-2}$  for the entire Pacific basin. The majority of this work was done by myself, with Diego Melgar providing grant funding and minor edits prior to submission to the Natural Hazards and Earth System Sciences journal. This assumption had been applied to spectral analysis and tsunami source inversions for over 20 years. This dissertation finds that the background open ocean tsunami spectrum does not hold constant for the entirety of the Pacific basin; instead, it varies seasonally as function of infragravity waves generated from extra-tropical and tropical cyclones from across the Pacific. This dissertation finds that the North Pacific (from the Alaska Aleutians to off shore of the US Pacific northwest) had significant departures from

the  $\omega^{-2}$  reference slope due to the region being a hotspot for infragravity wave production.

From Santallanes, S. R., Ruiz-Angulo, A., Melgar, D. (2023). Tsunami waveform stacking and complex tsunami forcings from the Hunga-Tonga eruption. *Pure and Applied Geophysics*, 180(6), 1861-1875. This dissertation then examines the tsunami source complexity of non-seismic tsunami sources by investigating the tsunami source of the 2022 Hunga Tonga global tsunami. The tsunami from this event traveled faster and further, seemingly able to propagate without obstruction from landmasses. This dissertation finds that the tsunami source of the global tsunami was transient atmospheric source that traveled with the Lamb wave produced by the violent eruption of Hunga Tonga. This dissertation also finds evidence of gravity wave shedding and dispersion that amplified tsunami signals at regional and global distances. It also finds that resonance with bathymetry and topography may have led to increased tsunami amplitudes along the East Pacific.

Another examination of tsunami source complexity came by way of the 2020 Sand Point Earthquake. Due to the complexity of this earthquake, a global team was headed by me to investigate the tremor. Dara Goldberg and Will Yeck provided USGS data and techniques for analyzing far-field data. Pablo Koch provided the annealing code that was used as the basis for conjoining water level, seismic, and geodetic data. Brendan Crowell provided expertise of the Alaskan Subduction Zone. Jiun-Ting Ling provided advice on how to invert data from

water level data. Diego Melgar was the principle investigator and grant provider. Conceptualization and writing was done by myself. All co-authors provided edits for the manuscript in review, along with two anonymous peer reviewers and Benjamin Brooks, who was the USGS internal reviewer.

The earthquake was classified as a right-lateral strike-slip rupture by the United States Geological Survey National Earthquake Information Center (USGS-NEIC). However, it produced a sizeable tsunami that propagated all the way to Hawai'i, and produced hazardous coastal conditions akin to a subduction zone earthquake. In order to investigate the source complexity of this event, this dissertation combines water level data from open ocean instruments and coastal sea level stations with seismic and geodetic data to create a method capable of discerning it. It finds that the most likely tsunami source came from a sizeable slow subduction zone interface rupture that was concealed by fast left-lateral strike-slip rupture preceding it.

Finally, this dissertation considers the effects of source complexity on tsunami inundation for the US Pacific northwest from potential Cascadia Subduction Zone ruptures. This work was done by myself with Diego Melgar providing guidance and minor edits to grammar. Simple, homogeneous earthquakes have been used by state and federal agencies to constrain the tsunami hazard of the Cascadia Subduction Zone for  $\sim 30$  years. These models have also been used by public-private partnerships to establish the land-use and building codes of coastal

towns through the region local to the subduction zone. Homogeneous sources have been shown to underestimate the hazard of tsunami inundation. This dissertation shows that heterogeneous ruptures based off of various geodetic locking models produce tsunami inundation with significant spatial extent differences. In addition, it is shown that the 1-in-2475 ( $\sim 0.004$ ) exceedence risk of heterogeneous sources also extends further inland than homogeneous sources with the same exceedence risk.

CHAPTER II  
TSUNAMI WAVEFORM STACKING AND COMPLEX TSUNAMI FORCINGS  
FROM THE HUNGA-TONGA ERUPTION

From Santellanes, S. R., Ruiz-Angulo, A., Melgar, D. (2023). Tsunami waveform stacking and complex tsunami forcings from the Hunga-Tonga eruption. *Pure and Applied Geophysics*, 180(6), 1861-1875.

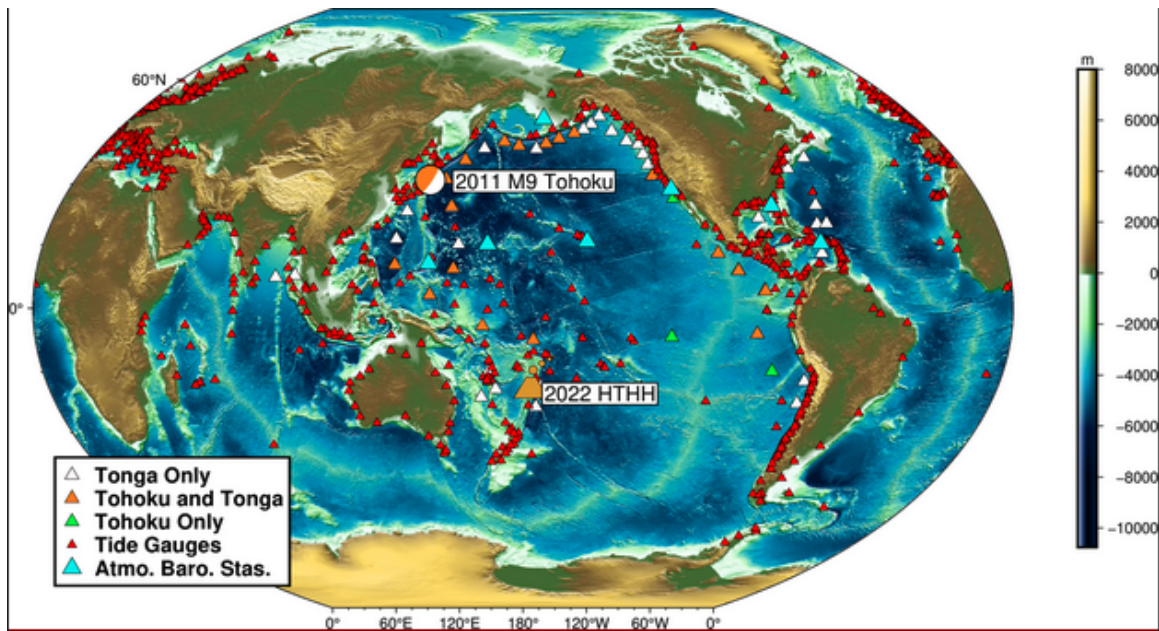


*Figure 1.* DART buoys and tide gauges analyzed in this work. DART buoys that were operable with data from only the Tohoku tsunami are shown in neon green. DART buoys that were operable with data for both Tohoku and Tonga are shown in dark orange. DART buoys that were operable with data for only the Tonga tsunami are shown in white. Tide gauges used in this analysis are shown in red. The focal mechanism of the Mw 9.1 Tohoku earthquake is plotted along with the location of the HTHH volcano in white. Atmospheric barometer stations are plotted in teal.

## 2.1 Introduction

On January 15, 2022 at 04:14:45 UTC, the Hunga Tonga Hunga Ha’apai (HTHH) volcano (Figure 1) erupted violently. The Surtseyan-style eruption likely had a volcano explosivity index (VEI) of 5 (Yuen et al., 2022) and produced an ash cloud that rose into the stratosphere. Teleseismic models from the United States Geological Survey (USGS) ascribed to the eruption an equivalent earthquake magnitude of Ms 5.8. The eruption produced acoustic waves in the audible portion of the spectrum recorded and noticed as far away as Anchorage, AK, USA and The Yukon, Canada at distances over 9,700 km away. Pressure waves from the eruption had an observed maximum value of 7 hPa in New Zealand and had observed values of 2 hPa at various locations around the planet, (Carvajal et al., 2022; Heidarzadeh, Gusman, Ishibe, Sabeti, & Šepić, 2022; Kubota, Saito, & Nishida, 2022; Matoza et al., 2022). The eruption also generated a Pacific wide tsunami along with possible meteotsunamis in the Caribbean Sea, the Gulf of Mexico, and the Mediterranean Sea. Preliminary reports show that in the Pacific wave heights were as small as 0.15 m at Jeju Island, South Korea and as high as 2.5 m impacting Vanuatu (Carvajal et al., 2022). At oceanic basins with almost no connectivity from the source region, the National Oceanic and Atmospheric Administration (NOAA) CO-OPs reported tsunami amplitudes on the order of 0.1 m (Figure 2).

The tsunami is meaningful because it had amplitudes significant enough to produce minor damages worldwide (Carvajal et al., 2022). This global nature of the event is reminiscent of the last great volcano-triggered tsunami, the 1883 Krakatoa

event (Satake et al., 2020). The paroxysmal eruption there had a VEI of 6 and produced widespread tsunami impacts (Harkrider & Press, 1967; Paris et al., 2014; Press & Harkrider, 1966; Yokoyama, 1987). Unlike HTHH, the Krakatoa tsunami had remarkable amplitudes in the near field (41 m reported at Banten, Pararas-Carayannis (2003)). For that event, barographs recorded pressure arrivals around the world as well. That tsunami seems to have been much larger in the near field than HTHH and resulted in significantly more loss of life. Like HTHH, the Krakatoa tsunami was observed worldwide and analog mareograms of it have been studied before (Harkrider & Press, 1967; Press & Harkrider, 1966). The nature of the physical mechanisms leading to tsunamigenesis in 1883 is debated still. Processes at the volcanic edifice (e.g. caldera collapse, pyroclastic flows, and the explosion) have been invoked to explain it (e.g. Nomanbhoy & Satake, 1995), especially because near-field amplitudes were remarkably high. But, it appears that, like with HTHH, Krakatoa had tsunami arrivals in different ocean basins at times before typical tsunami wave speeds would allow, hinting at complex atmosphere/ocean interactions (e.g. Yokoyama, 1987).

The HTHH eruption provides a unique dataset. It is the only volcanic tsunami source to be recorded globally in the modern instrument age of tsunami detection networks. In particular, the increase in deep ocean assessment and reporting of tsunamis (DART) buoys over the past two decades, coupled with a large tide gauge network, has allowed for the tsunami to be characterized on a world wide scale (Figure 1). Here we use these networks to perform an

observational investigation into what physical processes can be invoked as the source or sources for the HTHH tsunami waves. A survey of past studies associated with volcanically triggered tsunamis reveals that there are potentially 3 categories of them (Figure 2).

The first, and simplest, is the possibility of deformation processes at the volcano such as a caldera collapse or other large submarine mass movements. Were this to be the dominant source we would expect large near-field amplitudes (as in 1883 Krakatau), significant dispersion of the tsunami time series (given a comparatively localized source area, (e.g. Saito, Inazu, Miyoshi, & Hino, 2014), and a propagation speed, or “moveout”, of the water-level disturbances according to  $v_{tsun} = \sqrt{gh}$ , where  $g$  is the acceleration due to gravity and  $h$  the depth of the ocean. For the pacific basin assuming a mean depth of  $\sim 4000$ - $5000$  m this leads to  $v_{tsun} \sim 200$ - $220$  m s<sup>-1</sup>.

The second, is the possibility of the tsunami being generated by the force on the water column generated by the underwater component of the eruption or the subsequent collapse of initially sub-aerial pyroclastic density currents into the water (Heidarzadeh et al., 2022). Here too, we’d expect a significant dispersive character and a moveout velocity given by  $v_{tsun} \sim 200$ - $220$  m s<sup>-1</sup>. For both of these types of tsunami sources we would also expect rapid attenuation with distance given the relatively small geographic footprint of the source compared to that of great earthquakes (e.g. Okal & Synolakis, 2003).

Lastly, we have the possibility of pressure disturbances in the troposphere

produced by the initial explosion and by the eruption column generating the sea-surface disturbances. Here, it is not redistribution of mass or deformation processes at the volcano which displace the water column and create the tsunami. Rather, it is pressure perturbations in the troposphere which trigger an ‘inverted barometer’ response of the sea surface, thus creating tsunami waves. This category of atmospherically-driven tsunami source itself can be quite complex and is typically thought to potentially include three kinds of possible perturbations (e.g. Watada & Kanamori, 2010). These are: acoustic waves, internal gravity waves, and Lamb waves, each of these is thought to produce enough pressure anomalies in the troposphere to induce a tsunami response of the sea surface. Acoustic waves are caused by adiabatic compression and expansion, which propagate with a velocity dependent on the speed of sound in the medium ( $v_{air} \sim 330$  m/s). Gravity waves are those whose restoring force is gravity. These are common in the ocean and atmosphere (i.e. tsunamis and convection overtopping), and propagate much more slowly than the speed of sound. Lamb waves meanwhile, are interface waves, like Rayleigh waves in seismology. The difference here is that instead of being an elastic wave trapped in the solid portion of the Earth at the boundary with the atmosphere, it is an acoustic interface wave trapped in the troposphere at the boundary with the ocean or solid Earth. They have been observed before with earthquake and volcanic sources which excite the troposphere (Arai et al., 2011; Watada & Kanamori, 2010) and propagate from the source with a characteristic speed slightly below or equal to that of sound,  $v_{Lamb} = 310\text{-}340$  m s<sup>-1</sup> (Nishida,

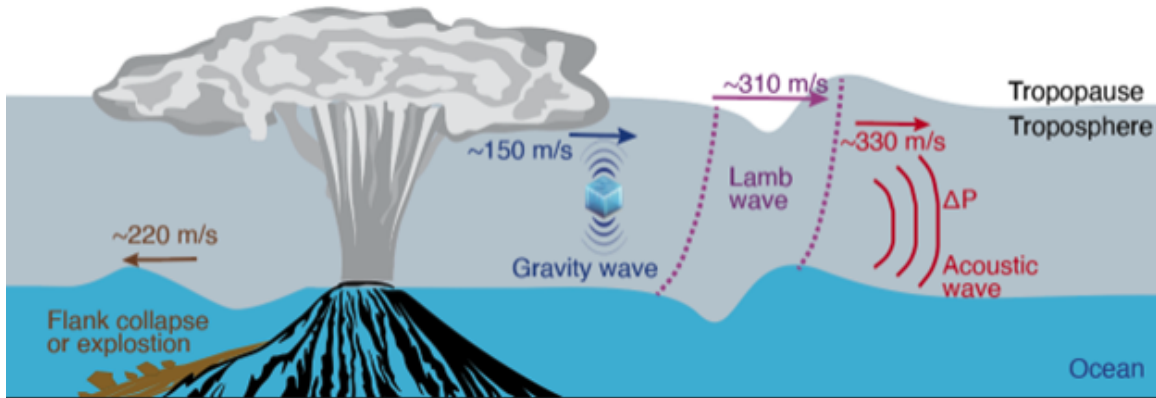
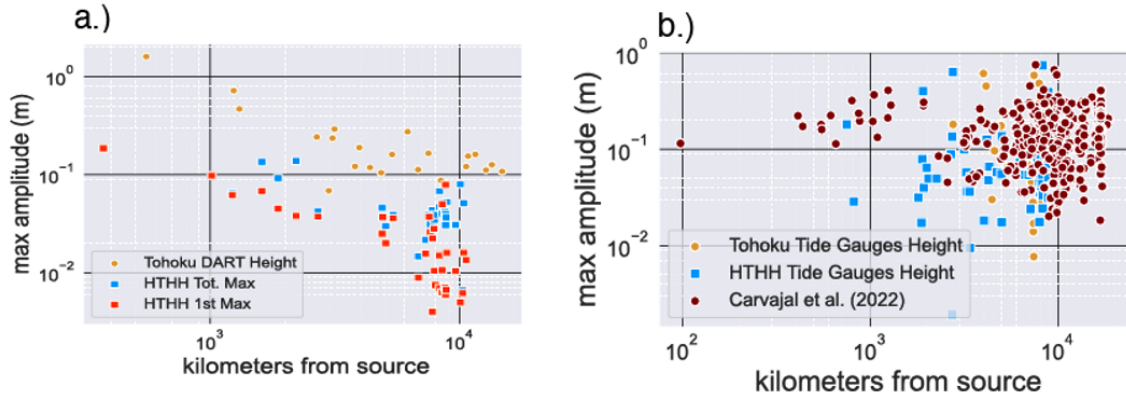


Figure 2. Schematic diagram showing the 4 potential tsunamigenic source mechanisms from the eruption of HTHH. From left to right, a flank collapse or explosion would have a tsunami propagation speed of  $\sim 220$  m s<sup>-1</sup>. An internal gravity wave would have a propagation speed of  $\sim 150$  m s<sup>-1</sup>. A Lamb wave would have a propagation speed of  $\sim 310$  m s<sup>-1</sup>. Lastly, an acoustic wave would have a propagation speed of  $\sim 330$  m s<sup>-1</sup>.

Kobayashi, & Fukao, 2014; Revelle & Whitaker, 1996). Lamb waves are long-period traveling atmospheric disturbances, uncoupled from the water, but that can have enough of a pressure perturbation to induce uplift or subsidence of the sea-surface and generate a tsunami. For these types of atmospheric sources we would not anticipate significant dispersion in the tsunami first arrivals (Nishida et al., 2014; Revelle & Whitaker, 1996). Additionally, it is well-known that all of these atmospheric waves propagate with relatively low attenuation (Hedlin, Walker, Drob, & de Groot-Hedlin, 2012).

In this paper we aim to understand which of these myriad processes contribute to tsunamigenesis. We use hydrodynamic observations from the deep- and shallow-water worldwide networks to attempt to identify these different generation mechanisms. To do this we carry out a moveout stacking analysis, as



*Figure 3.* (a) First arrival amplitudes and peak amplitudes in meters recorded at 22 DART buoys from the M9 Tohoku-Oki tsunami and 34 DART buoys from HTHH. (b) Peak amplitudes in meters recorded at 27 tide gauges from the M9 Tohoku-Oki tsunami and 82 tide gauges from HTHH with clear and obvious tsunami signatures. The 403 tide gauges from Carvajal et al. (2022) are plotted to compare our dataset with their results. Only first arrival amplitudes are plotted.

well as use the spectra of the data at DART buoys to analyze dispersive behavior, and study the amplitude decay characteristics of the event. We will conclude that the first arrival at both deep- and shallow-water stations is almost certainly due to an atmospheric Lamb wave, whose period can be measured at  $\sim 40$  mins, with some potential small contributions from acoustic waves. Heidarzadeh et al. (2022) reported a period band of 30-60 min for atmospheric waves, which is consistent with our results. Significant visible later arrivals, especially in shallow water, may be a superposition of internal tropospheric gravity modes and tsunami modes from sources in the water column. As a point of comparison, we rely on the DART and tide gauge data for the previous significant and well-recorded Pacific-basin scale event — the tsunami from the M9 Tohoku-Oki earthquake ((e.g. Satake, Wang, & Atwater, 2003), Figure 3).

## 2.2 Data and Methods

We use data from 35 deep water sites (DART buoys) and 114 shallow-water stations (tide gauges) for the bulk of our analysis (Bernard & Titov, 2015). The 15 s and 1 min sampled DART data are available from NOAA and GNS Science for the HTHH tsunami. For the Tohoku-oki tsunami, we also use 15 s and 1 min tide gauge data available from NOAA (DOC/NOAA/NOS/CO-OPS, Center for Operational Oceanographic Products and Services, National Ocean Service, NOAA, U.S. Department of Commerce, 2007). The HTHH tide gauge data is available from the Intergovernmental Oceanographic Commission (IOC) at 1 min intervals (Flanders Marine Institute (VLIZ), Belgium & Intergovernmental Oceanographic Commission-UNESCO, France, 2021). The data were de-tided and band-pass filtered from 5 min to 120 min where the tsunami energy is mostly concentrated (e.g. Rabinovich, 1997). Periods shorter than 5 min contain mostly infragravity waves and periods longer than 120 mins are mostly influenced by the tides. We then plot the tsunami waveforms together, offset by great circle distance from HTHH volcano to produce a record section shown in Figure 4. DART data for HTHH is mainly concentrated in the Pacific basin (32 sites). In addition, we utilize 2 DARTs from the Atlantic basin and 1 DART from the Indian basin. In contrast, all the DART stations for the Tohoku-oki earthquake are only in the Pacific basin since the waveforms were not of meaningful amplitude at other oceanic basins. We show only tide gauges that have a signal-to-noise ratio  $> 5$  and no time gaps (i.e., a clear and obvious tsunami signal) (114 stations out of  $>800$ ). We calculate the

arrival times based on the origin time of the eruption from the USGS event page (2022-01-15 04:14:45 UTC). Heidarzadeh et al. (2022) reported an eruption time of 4:15 UTC based on the analysis of nearby seismic data. In Figure 4, we manually picked tsunami phase arrivals and employed simple least-squares to find moveout speeds that aligned waveform features that seemed coherent from visual inspection. We recognize that this is a somewhat ambiguous or qualitative approach, so, to further explore whether there are coherent arrivals at other propagation or moveout speeds we employ a moveout stacking grid search approach which we now describe. Our moveout stacking process is thus: we first propose a candidate propagation or “moveout” velocity,  $v$ . Then, each waveform (deep- and shallow-water) is delayed a certain number of samples by calculating the time delay,  $t_{delay}$ , between the eruption origin time and the expected arrivals given this candidate moveout speed:

$$t_{delay} = \frac{d}{v} + t_{offset} \quad (2.1)$$

where  $d$  is the distance between the source and the station in meters. We explored a range of possible velocities in the interval from 100 m s<sup>-1</sup> to 400 m s<sup>-1</sup>.  $t_{offset}$ , meanwhile, is another free parameter. It is an arbitrary offset time that allows for arrivals whose origin is not exactly at the assumed event origin time, we allow  $t_{offset}$  values in the range of 0 to 6 hours. The goal of this is to explore whether coherent arrivals can be seen originating after the eruption origin time.  $t_{delay}$  is then the total delay time which is divided by the sample spacing of the DART or tide gauge recording,  $dt$ , to obtain an integer number of samples to delay each waveform

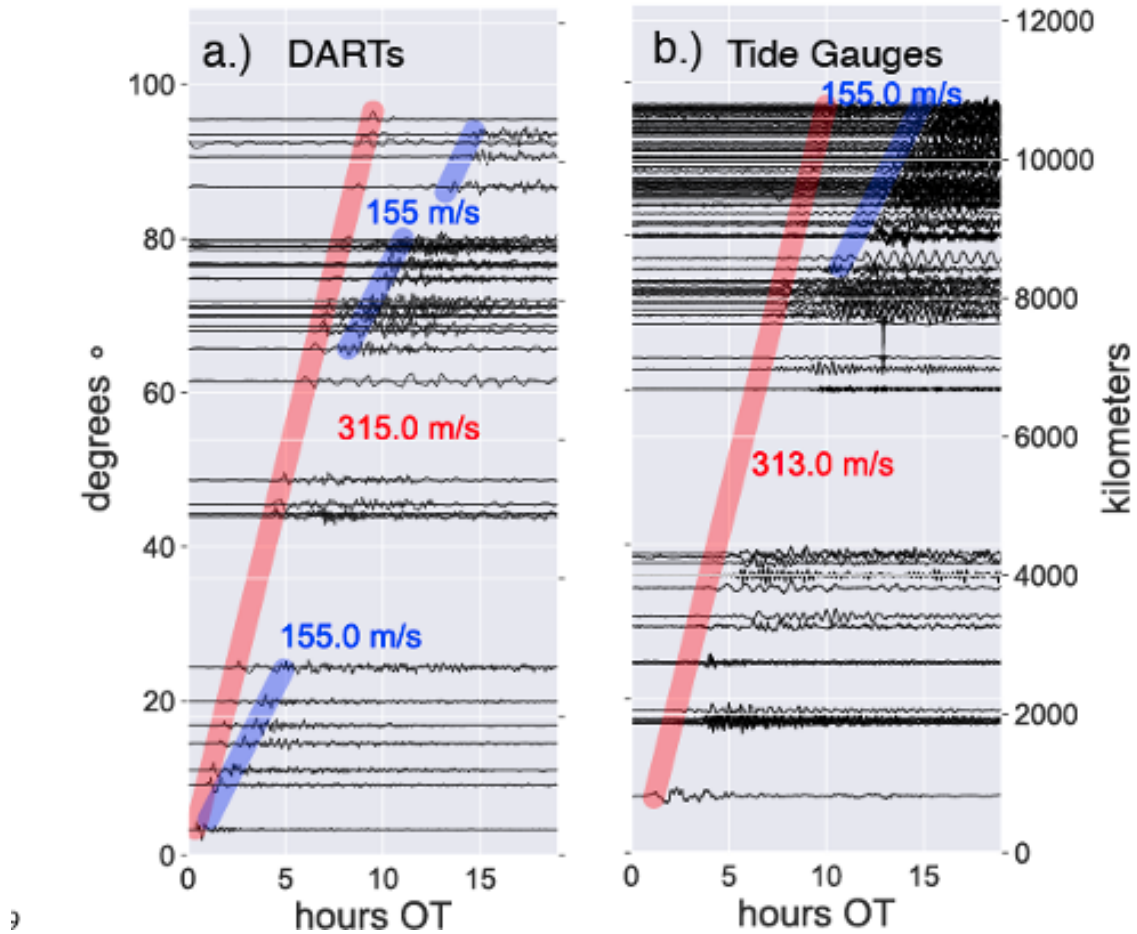


*Figure 4.* a.) Record section of the DART data from the HTHH tsunami. Red line denotes the speed of the first arrival seen at the DARTs. The blue line denotes the speed of potential secondary arrivals. b.) Record section of tide gauge data from the HTHH tsunami. The red line denotes the hypothetical Lamb wave arrival at the tide gauge stations. The blue line denotes the second arrival potentially seen the tide gauge stations. The data are shown for as long as 15 s and 1 min data were available. The tsunami amplitude waveforms are scaled individually to better appreciate the arrivals.

by. After delaying, individual waveforms are normalized by their peak value and then all waveforms from either the DART or tide gauge data sets are summed together. This creates a single “stacked” waveform for a particular combination of  $v$  and  $t_{offset}$  which is then divided by the total number of waveforms in the stack. This results in a maximum theoretical amplitude in any given stack of 1 which would reflect perfect coherence across all waveforms. For interpretation of the results we assume that noticeably high stack amplitudes for a particular combination of parameters this reflects a common physical process as the origin of the “arrivals” or of the “phase” at that particular moveout and offset time. The amplitude of the stacks as a function of moveout speed and offset time can be seen in Figure 5. We are interested as well in whether there are any potential azimuthal patterns so we also separated the waveform stacks into 7  $45^\circ$  azimuth “gates” or “bins” (Figures 5 and 6).

To study the spectral features of the waveforms we use the MTSPEC suite of codes from Prieto, Parker, and Vernon Iii (2009) to produce power spectra using the multi-taper method and investigate the dispersive behavior of the HTHH and Tohoku-oki tsunamis. We also produce spectrograms using the Wigner-Ville (WV) approach and apply it to the tsunami waveforms. Multi-taper techniques use prolate-spheroidal tapers and traditional Fourier techniques and have been demonstrated to be minimum variance, unbiased estimators of power which are much superior to the traditional periodogram approach Prieto et al. (2009).

Additionally, we extract the peak amplitudes of the first arrivals and of the overall waveforms to evaluate their distance decay characteristics (Figure 3).

In addition to the DART buoys and tide gauges, and to understand the nature of the deep-water pressure signals, we analyzed for HTHH, we studied 7 coastal atmosphere barometer stations (locations in Figure 1). This data was bandpass filtered between 12 min and 120 min, to keep comparisons parsimonious with those from the water level data, and to ensure that pressure peaks were not influenced by synoptic scale ( $L > 1000$  km e.g. extra-tropical cyclone) and/or mesoscale (meso-beta and meso-gamma i.e.,  $L < 100$  km e.g. thunderstorms or sea breezes) weather phenomena. These features were confirmed to be present during the event via satellite observation from GOES-17 and Himawari-8, and may impact pressure fluctuation calculations if not accounted for in the analysis.

We use equation 2 as a starting point to see how Lamb waves may interact with the vertical water column:

$$P' = \rho C_s w \tag{2.2}$$

Where  $P'$  is the maximum excess pressure available to drive a tsunami response of the water,  $\rho$  is the ambient air density,  $C_s$  is the air sound speed near the sea surface, and  $w$  is the vertical velocity of the water column.  $w = \frac{\eta}{T}$ , where  $\eta$  is the maximum displacement of the water column in meters and  $T$  is the “rise time”, the period of time water column takes to be displaced in seconds. We vary  $T$

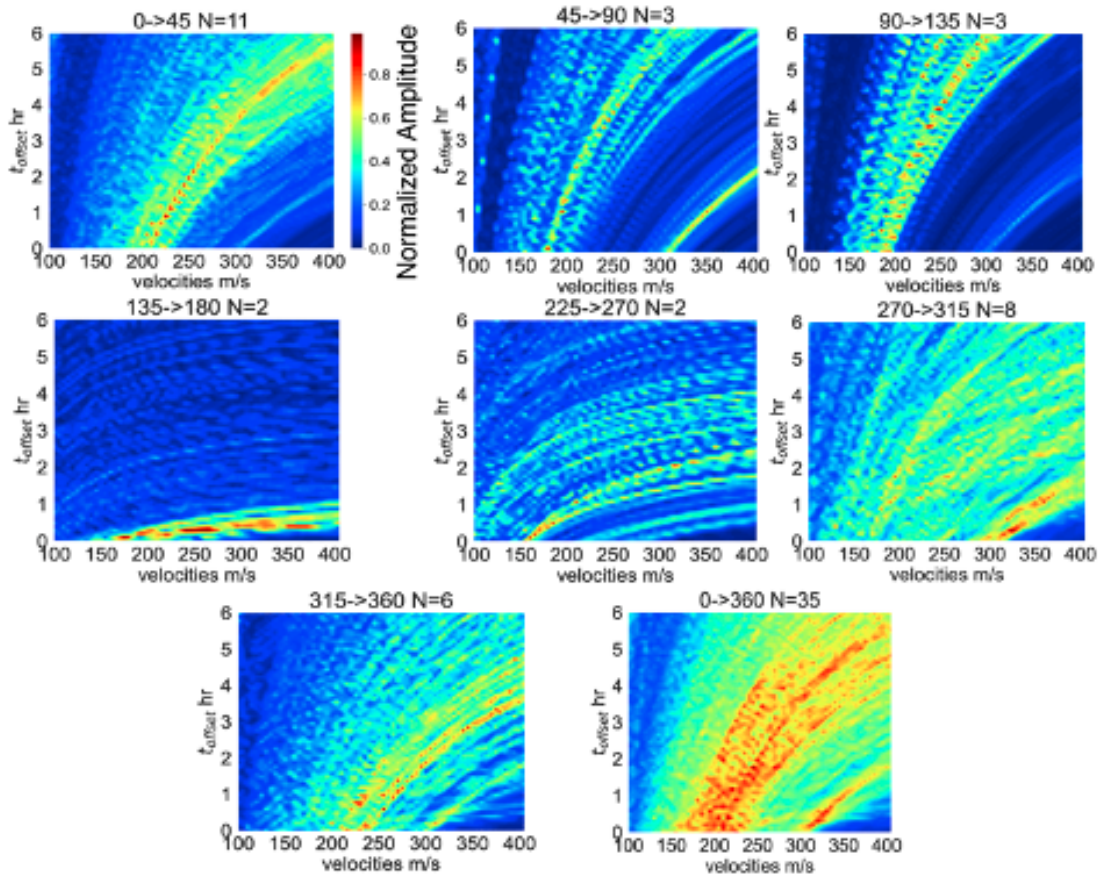


Figure 5. Amplitude stack plots with time delays in hours. The plots show the concentration of amplitudes in the 7 azimuth gates and full azimuth range with available DART data. 305 m/s moveout speeds are discernible in all but one – 135-180. 155 m/s moveout speeds are discernible in 3: 90-135, 135-180, 225-270. Moveout speeds in typical tsunami velocities are observable in all azimuth gates. The amplitudes are normalized by the number of DARTs in their respective azimuth gates.

from 0.0005 s to 5 s to systematically test what value is necessary to converted the DART data to atmospheric pressure, the goals of this iterative process is to obtain pressure values similar to that recorded at sub-aerial atmospheric pressure sites. In effect, we are assuming that there should be a match between pressure anomalies recorded at atmospheric pressure sites and the atmospheric pressures needed to drive the responses of the DART buoys. We assume  $\rho = 1.3 \text{ kg m}^{-3}$  and  $C_s=330 \text{ m s}^{-1}$ . Because the phase speeds of the potential Lamb wave are close to the speed of sound in the case of HTHH, we must employ a correction factor to the equation proposed by Watada (2009) of the form:

$$P' = \rho_o C_s w \frac{N}{k C_s} \frac{1}{\sqrt{1 - (\frac{C_p}{C_s})^2}} \quad (2.3)$$

Where  $C_p$  is the phase speed (305 m s<sup>-1</sup>), N is the buoyancy frequency ( $\sim 0.019 \text{ rad Hz}$ ), and k is the horizontal wavenumber ( $k = \frac{2\pi}{C_p T_\lambda}$ ), and  $T_\lambda$  is the period of the Lamb wave (Watada, 2009). In the results section we will show that  $T_\lambda$  can be measured as  $\sim 40 \text{ min}$  from observation of the DART waveforms tacks. Upon assuming such value for  $T_\lambda$ , we arrive at  $k \sim 8.33 \times 10^{-6} \text{ m}^{-1}$ .

In seismology terms, the duration that the Lamb wave deforms the vertical water column, the rise time, would be equivalent to the period of deformation the vertical water column experiences by seismic sea surface deformation, e.g., for Tohoku-Oki's tsunami this was assumed to be  $\sim 30\text{s}$  (Arai et al., 2011; Fujii, Satake, Sakai, Shinohara, & Kanazawa, 2011). However, in this case, we are

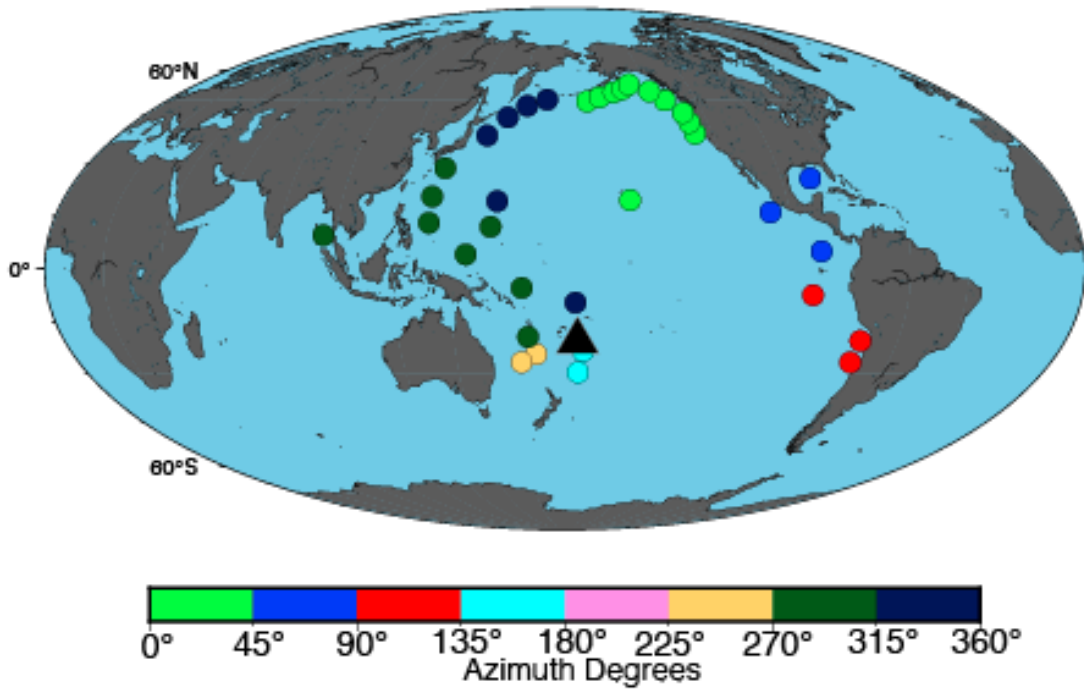


*Figure 6.* Amplitude stack plots with time delays in hours. The plots show the concentration of amplitudes in the 7 azimuth gates and full azimuth range with available DART data. 305 m/s moveout speeds are discernible in all but one – 135-180. 155 m/s moveout speeds are discernible in 3: 90-135, 135-180, 225-270. Moveout speeds in typical tsunami velocities are observable in all azimuth gates. The amplitudes are normalized by the number of DARTs in their respective azimuth gates.

estimating the period of deformation due to an atmospheric source acting on the top of the water column.

### 2.3 Results and Discussion

Previous work on Krakatoa and Mt. Pinatubo (Harkrider & Press, 1967; Press & Harkrider, 1966; Watada & Kanamori, 2010) already highlighted the potential complexity of air-sea coupling from an explosive eruption. There it was found that such subaerial sources should produce pressure perturbations in the atmospheric internal gravity, traditional tsunami, and Lamb wave modes. Indeed, Figure 4 suggests from pure visual inspection that there are at least 2 and potentially 3 different tsunami arrivals or phases, with different speeds of propagation. Ostensibly, each is associated with a different generation mechanism (e.g. Figure 2). Figure 5 also shows that across all azimuths there are preferential combinations of tsunami propagation speeds and offset times that produce preferentially high stack amplitudes. In Figure 7 we show the values of these stacks for the tide gauges and DARTs for  $t_{offset} = 0$ . This represents a single “slice” through the bottom of each subplot in Figure 5 which captures the behavior if one assumes that all tsunami perturbations originate at the time of the HTHH eruption. We do not find compelling evidence that delayed sources are widespread as we will discuss later on. From Figure 7, at the deep ocean stations (e.g., DARTs) the three potential phases are visible; however, the shallow-water tide gauges only stack somewhat coherently (Figure 7b) for one: 155 m s<sup>-1</sup>. Following we discuss each potential moveout speed and its significance.

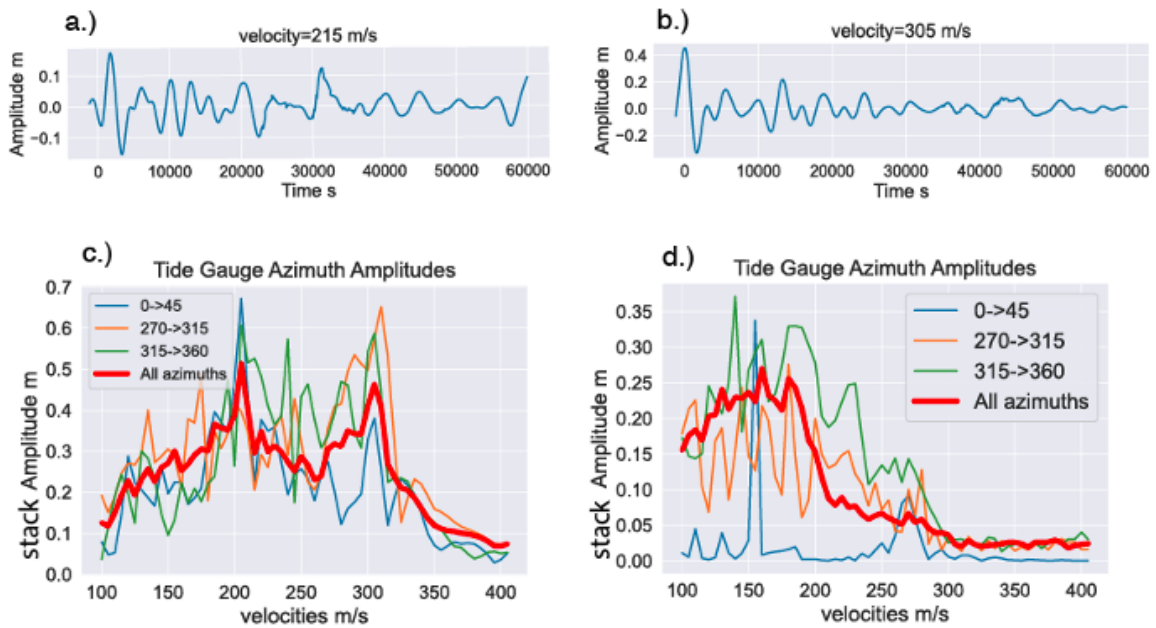


Figure 7. a.) The amplitude stack plot of normalized DART waveforms combined assuming a velocity of 215 m s<sup>-1</sup>. b.) The amplitude stack plot of normalized DART waveforms combined assuming a velocity of 305 m s<sup>-1</sup>. c.) Peak amplitudes at toffset=0 for the averaged, normalized DART stacked waveforms for velocities from 100 - 400 m s<sup>-1</sup> for various azimuth ranges. All azimuths contain 35 stations, 0-45 11 stations, 270-315 8 stations, and 315-360 6 stations. d.) The same as c.) but for tide gauge data. There are 114 stations for all azimuths, 0-45 1 station, 270-315 7 stations, and 315-360 14 stations.

### 2.3.1 Moveout at 315 m/s.

In aggregate, the most obvious feature in the data set is a definite tsunami first arrival moving out from the source with a propagation speed of  $\sim 315$  m s<sup>-1</sup> at DART stations and tide gauges in both the Pacific and Atlantic basins (Figure 4). At the DART buoys it has a far more prominent amplitude than at the tide gauges. It is easily seen in the DART record section as highlighted in red in Figure 4a. The waveform stacks confirm this (Figure 5-7) with a prominent peak in the stack amplitude at these speeds. There is no clear azimuthal variation to the preferential propagation speed and the observed value aligns with what is reported for other observations (Carvajal et al., 2022; Kubota et al., 2022; Matoza et al., 2022) of 300-307 m s<sup>-1</sup> for other related phenomena such as infrasound. This simple observation already likely rules out processes at the volcanic edifice (such as caldera collapse) as the source for the first arrival. Rather that the propagation speed is similar to that of sound in the atmosphere and does not correlate to bathymetry, is consistent with that of a Lamb wave. While Lamb waves from volcanic eruptions have been noted before (e.g. Nishida et al., 2014); this eruption would be the first time that one is observed by the modern tsunami instrument networks. The proposed Lamb wave signature managed to be discerned on all DARTs that were in “event” mode in the Pacific and a few in the Atlantic, which captured it despite not being activated in event mode. Of note as well is that the stack amplitude has azimuthal dependence suggesting perhaps that the Lamb wave generation process has a radiation pattern itself and results in higher amplitudes at certain azimuths. The Lamb wave stack

amplitudes are highest between 270-360 and appear to be at a minimum between 90-180 (Figure 5). Additionally, that the stack is so coherent and results in a relatively simple pulse-like shape is indicative of the relative simple propagation behavior – we can measure the period of the Lamb wave at  $\sim 40$  min from Figure 7.

We measure the amplitudes of the first tsunami arrivals as well as on the full waveform (Figure 3). We observe that the amplitudes decay like  $r^{-1/2}$ , where  $r$  is the distance from the source. This too rules out a localized source area at the volcanic edifice, we would expect much faster attenuation. Note that the HTHH decay is similar to that observed during the Tohoku-oki earthquake. We note as well that while the maximum amplitudes of the Lamb wave are smaller than the maximum amplitude of the overall tsunami waveforms, especially the further the stations are from the source, the pattern of distance decay remains the same.

Spectral analysis (Figure 8) is consistent with this view as well. For example, during the tsunami from the Tohoku-Oki earthquake the first arrivals had little to no dispersive behavior, it was not until long distances ( $>90$  degrees) that dispersion became readily apparent in the DARTs. The same is true for HTHH with only marginal amounts of dispersion in the spectra (Figure 8). Revelle and Whitaker (1996) hypothesized, that for Lamb waves, some small amounts of dispersion could be due to differences in meteorology and topography along the Lamb. Finally, we note that while this initial Lamb wave arrival can be seen in some of the tide gauge recordings (Figures 3B,4B) it is very small throughout that

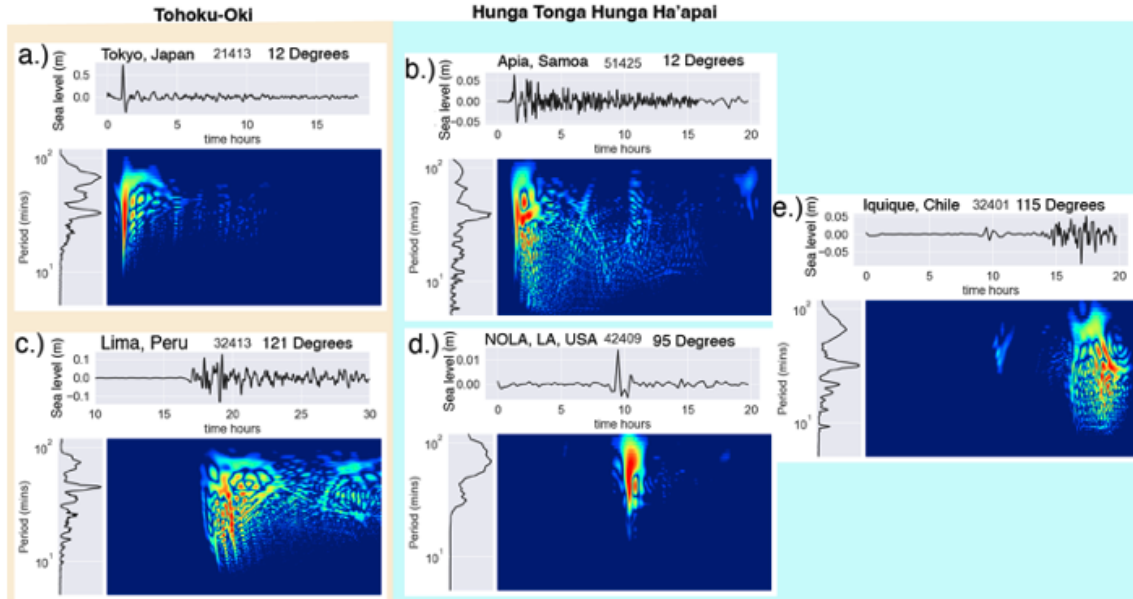


*Figure 8.* Examples of multi-taper spectral analysis Wigner-Ville spectrograms of equidistant DART buoys. a.) and b.) are about 12 from their respective sources. C.), d.) and e.) are about 95-121 from their respective sources. A.) and c.) show the dispersion of tsunami waves as they move away from the earthquake source. B.), d.) and e.) show how little dispersion there is with the tsunami source from HTHH with the associated Lamb wave front. 21413 is 700 NM ESE of Tokyo, JP. 32412 is 1000 NM W of Lima, Peru. 51425 is 370 NM NW of Apia, Samoa. 42409 is 247 NM S of New Orleans, LA, USA.

observational data set. It is not the dominant tsunami source in the near-shore environment.

### 2.3.2 Moveout at 205 m/s.

The stack amplitude analysis (Figure 7a) also indicates a peak in the stack amplitudes at a moveout speed of  $\sim 205$  m s<sup>-1</sup> for the deep-water sites and for all azimuths. Interestingly this speed, however, is not immediately obvious in the record sections (Figure 4). The exact moveout speed varies slightly depending on the azimuth hinting at a process dominated by bathymetry and not by atmospheric

propagation. Azimuths that cross deeper ocean depths have faster values around 220 m s<sup>-1</sup> and shallower depths having values closer to 205 m s<sup>-1</sup>. These speeds are consistent with those typically expected in the Pacific basin for regular tsunami propagation. We note as well that moveout speeds in this range do not stack coherently at the tide gauges (Figure 7b) apart from those in the 315-360 azimuth range, which sees an obvious peak at 220 m s<sup>-1</sup>. There are several peaks in the other azimuth bins that are slightly below 200 m s<sup>-1</sup>, which may be explained by the shallower bathymetry along the path to those tide gauge stations.

This moveout speed is where a “traditional” tsunami generated by processes at the edifice would manifest. That we see a peak in the stacks suggests that there might be indeed some contribution to the recordings from that. However, the distance attenuation pattern proportional to  $r^{-1/2}$  in the peak amplitudes observed in Figure 3, especially for the tide gauges, would indicate that the collapse of the volcanic edifice by itself would be insufficient to account for the basin wide effects observed in Figure 7. Potentially then, some other set of tsunamigenic mechanisms which produce waves that propagate a common tsunami speeds is likely involved. For atmospherically driven events (meteotsuamis) Monserrat, Vilibić, and Rabinovich (2006) detailed 3 potential resonances that may be in play during : Proudman resonance, Greenspan resonance, and shelf resonance.

For the DART buoys, Proudman resonance is the more plausible source of the tsunami waves at this moveout speed. The stations are in the open ocean at distances where shelf resonance and edge wave noise should be negligible. To

generate a tsunami, this result would imply that the atmospheric source was traveling at a speed that matched that of longwave ocean waves in the open ocean. Of which, the 155 m s<sup>-1</sup> and 305 m s<sup>-1</sup> velocities would be too slow and too fast respectively —the velocities from 200-220 m s<sup>-1</sup> are in the correct range. Typical pressures transients needed for meteotsunami processes are of only a few hPa (Monserrat et al., 2006). The HTHH eruption had an initial pressure jump of  $\sim 7$  hPa near the source, and distant atmospheric stations were able to record pressure jumps of  $\sim 2$  hPa. If we use equations 2 and 3 to estimate what atmospheric pressures are needed to force the DART signals to match atmospheric pressures we obtain the results shown in Figure 9. This suggests that it is possible that the atmospheric pressures needed to generate the amplitudes seen at the DARTs are of a similar order to what has already been identified as necessary in past studies of meteotsunamis (Figure 9).

### 2.3.3 Moveout at 155 m/s.

The third possible moveout velocity where we find potentially coherent stacks is slower and less conspicuous. We see from Figure 4a that there is sometimes a secondary arrival that can be observed at many of the DART stations within  $\sim 20$  and between 60-80 and for tide gauges between 70-100 from the source. It propagates with a move-out velocity closer to  $\sim 155$  m s<sup>-1</sup>. Figure 7 shows that for times  $t_{offset} = 0$  this speed does not produce any coherent stacks in the DART data yet appears more strongly in the tide gauge data. Theory and modeling (e.g. Watada & Kanamori, 2010) shows that a more slowly traveling atmospheric

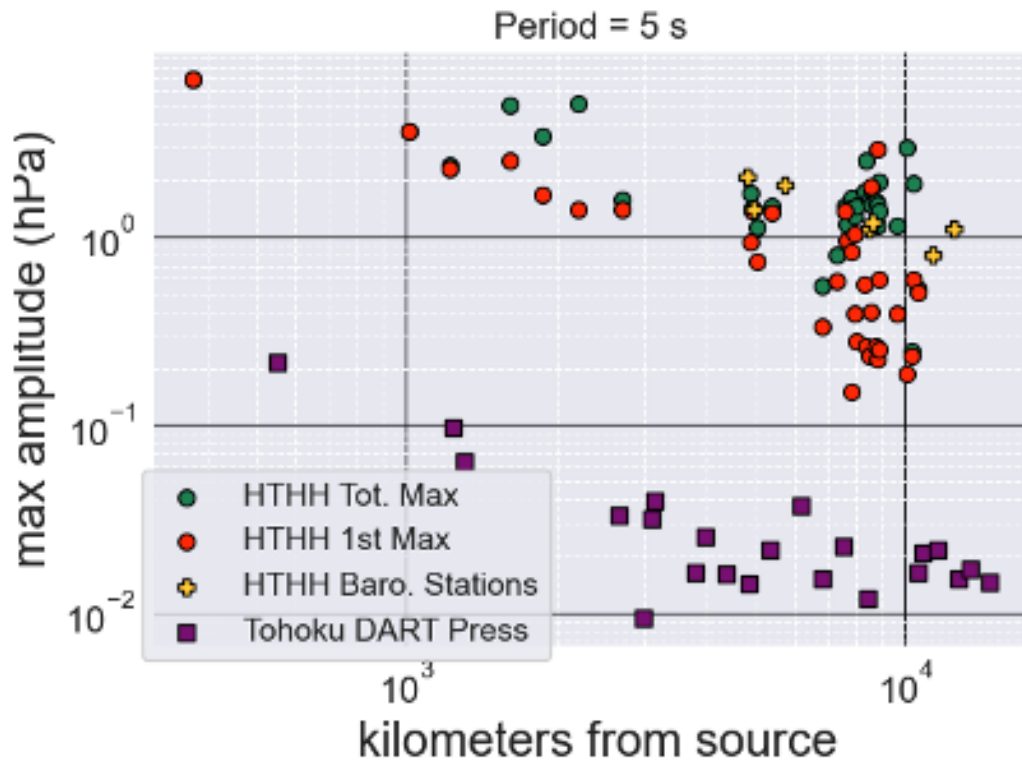


*Figure 9.* First arrival amplitudes and peak amplitudes in meters recorded at 22 DART buoys from the M9 Tohoku-Oki tsunami and 34 DART buoys from HTHH are converted to pressure amplitudes via equations 2 and 3. We compare these calculated values to terrestrial barometer station peak amplitudes from 7 coastal barometer stations.

internal gravity mode should exist but that it can often be too close to the tsunami mode itself to be easily visible in hydrodynamic data. If the  $\sim 155$  ms<sup>-1</sup> mode we observe is indeed a manifestation of the atmospheric internal gravity waves, then it has implications that it is likely generated as a result of the air-sea coupled effects of the Lamb wave. This is speculative, we concede, however note that the  $\sim 155$  m/s arrivals identified in the DART gauges in Figure 4, if extended back in time do not connect back to  $t = 0$ . This suggests that they are generated with some delay from the original source, this is what motivated adding the  $t_{offset}$  term in equation 1, however the stack analysis does not conclusively show delayed sources with propagation speeds of  $\sim 155$  m s<sup>-1</sup>.

Internal gravity wave generation is ubiquitous in the atmosphere. It is possible that the Lamb wave passage displaced air parcels in a process like frontal passage, generating internal gravity waves that emanate from it. This can occur at those periods which coincide with the tsunami band, and indeed internal gravity waves can have periods of up to  $\sim 17$  hours (Ruppert Jr et al., 2022). Using this framework can provides a simple explanation for the internal gravity waves generated far from the volcanic source that we see in Figure 4. However, it doesn't explain their constant speed of propagation. It may be that the constant speed and period of the Lamb wave and its passage are what lead to the near universal speed of the internal gravity waves when generated around the world. Some of these complexities were discussed by Heidarzadeh et al. (2022), where they showed that the characteristics of the tsunami waves recorded on DARTS and tide gauges

were significantly different. The mechanism for how this may be is unknown in the tsunami sciences. Analogs from meteorology may be useful as a starting point.

**2.3.4 Other effects and observations.** Beyond Proudman resonance and its potential contribution to the deep-water records, the long-duration effects of the meteotsunami at tide gauges is another feature of the HTHH tsunami that warrants an explanation. Without a fully coupled atmospheric-oceanic model it is difficult to ascertain its nature, however it may have been enabled by excitation of Greenspan and shelf resonance. These two resonant effects acting would explain the amplification of tsunami amplitudes in certain areas of the Pacific basin. This longer duration of the event compared to traditional tectonic tsunamis (e.g. Kohler, Bowden, Ampuero, & Shi, 2020) is also apparent in deep water; the codas of the HTHH DART records are significantly longer than for the Tohoku case (Figure 8). This is only true in the Pacific, however, as DART 42409 in the Gulf of Mexico see the Lamb wave passage with no significant tsunami coda being generated.

### **2.3.5 Caveats to the interpretation.**

It is clear that the HTHH tsunami is complex and has potentially many processes contributing to its generation. We admit that, as hinted in the previous section, a difficulty in a final interpretation of the event is the lack of a fully coupled atmospheric-oceanic propagation model. Here we have relied on observational evidence to distinguish between different mechanisms. We think the basic interpretation is sufficiently compelling, that the first arrival is a Lamb wave

propagating in the atmosphere but that secondary arrivals result from complex atmospheric and oceanic sources perhaps aided by different resonant phenomena. But, ultimately designing a model that replicates the observations will be the final proof of this interpretation. For example, while the waveforms stacks in Figure 1 show slower traveling tsunami phases that do not seem to originate at event origin time, the stacking procedure was inconclusive in ascertaining whether this could indeed be justified. A fully coupled model that replicates the observation is missing. Additionally, we note that the potential source processes at the volcanic edifice are extremely complex. The eruptive plume and its interactions with the ocean and the atmosphere, its time history and the energetics of how it excites both are still a subject of vigorous investigation. Uncertainty in this regard also limits the interpretations we have made here.

### **2.3.6 Hazards implications.**

The hazard implications of these complex and simultaneously acting effects are important. Typical basin-scale tsunami warning (Bernard & Titov, 2015) relies on tsunami modeling based on earthquake source parameters and assuming long-waves in the water which have propagation speeds controlled by the bathymetry. For the case of HTHH, there is evidence of a complex set of processes with sources in the water column, such as caldera collapse or the explosion itself contributing only for later arrivals and probably with modest energy while the first tsunami perturbation is due to atmospheric phenomena exclusively. As a result, this first tsunami arrives much earlier than expected at far-field measurement stations and

shores. Its propagation speed is faster as it is controlled by the acoustic properties of the troposphere, thus, leading to difficulty in forecasting and communicating the threat of the tsunami to the public. Compounding the problem is that while this first arrival is prominent in deep water sites, its contribution to coastal hazards is indubitably very small. So, forecasting amplitudes and arrival times at sites of interest where people and assets might be at risk is doubly challenging. Future efforts to gauge the hazard of future volcanic tsunamis would benefit from incorporating meteorological and infrasound data. It has been shown in ours and recent works (e.g. Heidarzadeh et al., 2022) that meteorological processes may influence the propagation of air-sea coupled waves, as is the case with infrasound waves (Blom, Dannemann, & Marcillo, 2018). While the number of volcanic tsunamis is sparse, it is possible to model atmospheric profiles under varying conditions with global weather models (e.g., the Global Forecasting System – Finite-Volume Cubed-Sphere Dynamical Core (GFS-FV3)). GFS-FV3 serves as the dynamical core for the Goddard Earth Observing System (GEOS) model, which may serve as a starting point to model varying volcanic sources. It may potentially lead to a probabilistic hazard map of volcanic tsunamis.

Overall, the coastal effects of HTHH were small, at least compared to great earthquake tsunamis such as the Tohoku-oki event. However, conditions may still allow for tsunamis and tsunami effects to be hazardous, even at oceanic basins disconnected from the original tsunami source and on a worldwide scale. Events

like HTHH are rare “edge cases” but modeling improvements coupled with rapid identification of the source as volcanic in nature could abate the problem

## **2.4 Conclusion**

Here we have described in detail the data collected from the worldwide tsunami observing network for the HTHH event including 35 DART buoys and 114 tide gauge stations. The eruption of HTHH produced the largest volcanic source tsunami in the modern age of tsunami observation and it was recorded on a global scale. We have identified three potential phases of the tsunami. The first arrival is almost certainly a Lamb wave phase which travels faster than a traditional tsunami. Secondary phases are most likely a complex amalgam of traditional tsunami and atmospheric effects such as internal gravity waves. Additionally, the tsunami codas are long, we posit that the Pacific basin portion of the tsunami is likely to have been the result of processes like those in meteotsunamis such as Proudman resonance induced by the Lamb wave front, with various coastal areas seeing also effects from Greenspan and shelf resonance. Overall, we believe, that, while processes at the volcanic edifice, such as caldera collapse, likely contribute to tsunamigenesis, the evidence does not support this being responsible the predominant source mechanism. The hazards implications of this are important, the tsunami traveled faster than expected making characterizing it and communicating the threat to the public very challenging.

## 2.5 Data and Resources

DART data was accessed from two different API's: NOAA and GNS New Zealand. Information concerning the GNS New Zealand GeoNet API and DART data availability can be found at the following: <https://github.com/GeoNet/data-tutorials/blob/main/TILDE/README.md> . The DOI for GeoNet's DART is: <https://doi.org/10.21420/8tcz-tv02>. NOAA DART data is available from the following: [http://www.ndbc.noaa.gov/dart\\_data.php](http://www.ndbc.noaa.gov/dart_data.php). The data used in this study are archived on GitHub ([https://github.com/ssantellanes/Hunga\\_Tonga\\_Water\\_Level](https://github.com/ssantellanes/Hunga_Tonga_Water_Level)) and archived on Zenodo (Santellanes et al., 2022).

## 2.6 Declaration of competing interests

The authors declare no competing interests.

## 2.7 Acknowledgements

We acknowledge the New Zealand GeoNet project and its sponsors EQC, GNS Science, LINZ, NEMA and MBIE for providing data/images used in this study. The work of their engineers and software developers allowed for deep insights into their DART data. Their work provided us with extremely high quality and performance data unparalleled in other areas of the DART network. We also acknowledge Josef Dufek and Thomas Giachetti for providing insights into the processes involved with volcanic eruptions. We also acknowledge the Flanders Marine Institute (VLIZ); Intergovernmental Oceanographic Commission (IOC); Sea level station monitoring facility for the tide gauge data as well as the Center

for Operational Oceanographic Products and Services (CO-OPS/NOAA) for the historical tide gauge data.



CHAPTER III

CONTEMPORARY MEASUREMENTS OF THE BACKGROUND OPEN  
OCEAN TSUNAMI SPECTRUM USING THE DEEP-OCEAN ASSESSMENT  
AND REPORTING OF TSUNAMI (DART) STATIONS

From Santallanes, S. R. & Melgar, D. In review. Contemporary measurements of the background open ocean tsunami spectrum using the Deep-ocean Assessment and Reporting of Tsunami (DART) stations. *Natural Hazards and Earth System Sciences*.

### 3.1 Introduction

Among the challenges affecting tsunami science today is the need for accurate and expedient source models of tsunamigenic earthquakes. Studies have been undertaken to constrain the aleatory and epistemic uncertainty of the seismic portion of tsunami source models (i.e. via GNSS (Melgar & Bock, 2015)); however, there has been less focus on constraining these uncertainties for the oceanographic portion (i.e, via ocean bottom instruments (Tsushima, Hino, Fujimoto, Tanioka, & Imamura, 2009)). Rabinovich (1997) described a method to derive tsunami source spectra given by the spectral ratio of the observed coastal tsunami spectrum and the atmospheric-induced wave spectrum convolved with the background open ocean spectrum (BOOTS) and a constant. This method is useful because, if correct, it has the ability to allow separation of path (from bathymetry/topography) and source effects. However, its assertion that the BOOTS slope follows — consistently — a reference power law of  $\omega^{-2}$ , where  $\omega$  is angular frequency, is itself a potential source of aleatory and epistemic uncertainty. The basis of this reference power law can be found in the interpretations of the bottom pressure recorder (BPR) data for the open ocean for deployments of a few sites that spanned 1-11 months presented by Kulikov, Rabinovich, Spirin, Poole, and Soloviev (1983) and Filloux, Luther, and Chave (1991).

Following those findings, the simple log-linear spectral decay shape for the BOOTS has been traditionally used for tsunami studies focusing on the period band 10 mins to 120 mins. However, there is compelling evidence of a

myriad of forcings (Aucan & Ardhuin, 2013; Rawat et al., 2014; Webb, Zhang, & Crawford, 1991) that can potentially be impacting these and shorter periods of the BOOTS and potentially introduce deviations from this simple model (Filloux et al., 1991; Kulikov et al., 1983; Rabinovich, 1997; Rabinovich, Candella, & Thomson, 2013; Webb et al., 1991). The reference power law for the BOOTS has presented a precarious situation by ignoring the short periods of the tsunami spectrum. There is no change from oceanographic forcings; infragravity waves do not appear to influence its shape; and most puzzling of all, atmospheric forcings have been assumed to have no impact despite their purported involvement in the shorter periods by earlier literature (Filloux et al., 1991; Kulikov et al., 1983). The two simplest interpretations of these observations are: (1) The BOOTS characterizes an inherent energy cascade from low frequencies to high frequencies regardless of short period forcings within it, or (2) Previous measurements lack the spatiotemporal longevity to discern the impact of these short period forcings on its shape. Although it is surprising that no deviations have been demonstrated from a reference power law of  $\omega^{-2}$ . It seems certain, from the work done in this study, that variations in the BOOTS are relatively small at these spatiotemporal scales. Here we will find that, if variations in the BOOTS can be observed, we can only infer these characteristics by using instruments that are not confined to short, modest deployments with modest spatial coverage. Fortunately, instruments, such as the Deep-ocean Assessment and Reporting of Tsunamis (DART) stations, have been designed to handle the rough nature of observation in the open ocean to

provide information for tsunami early warning systems and record continuously. We leverage these instruments to measure the long-term behavior of the BOOTS on time scales of 1-10+ years, (Figure 10, Figure 11).

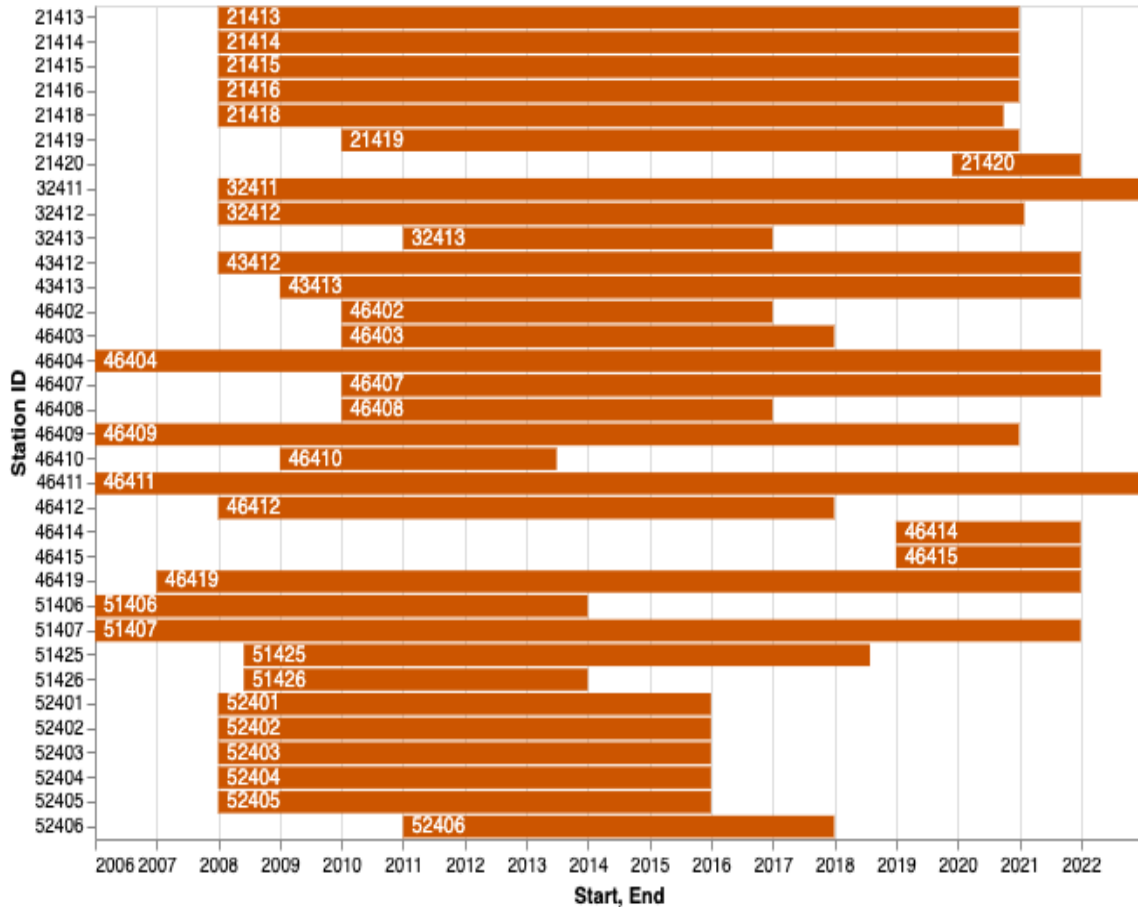


Figure 10. Station up-time graphs that show the time spans of data used for each DART in this study.

The tsunami community continues to make significant progress towards constraining epistemic uncertainty in source models (Mori et al., 2022). However, a potential complication these efforts may face is the lack of constraint of the open ocean background noise necessary to produce tsunami source models. Constraining this noise is necessary for understanding probabilistic effects of tsunamis as they

propagate from the open ocean to coastal locations. As pointed out by Rabinovich (1997), the BOOTS slope and intercept are vital for reconstructing tsunami source spectra, which allows for higher fidelity tsunami source models from the DART stations. They can then be used to diagnose — quickly — tsunami hazards and effects. It is imperative that the BOOTS slope be measured to ensure that its effects on coastal locations can be lead to reductions in epistemic uncertainty.

Here, we report that the BOOTS slope varies substantially from the  $\omega^{-2}$  reference power law used by previous literature. In fact a simple log-linear power law decays is too simplified a view of the long term behavior of the BOOTS. We find that, while the power law can be suitable for some areas of the Pacific basin and for shorter time spans, it performs poorly in other regions (e.g., the Gulf of Alaska and the Cascadia Subduction Zone). We find that the areas that deviate from the reference power law are in areas where infragravity wave (IGW) production is significant during the time periods of December, January, and February (DJF) or June, July, and August (JJA). We further show that these time periods of IGW production correspond most likely to meteorologically significant events (e.g., bombogenesis, extra-tropical cyclones, etc.). Additionally, we observe potential IGW effects on observed tsunami signal power from periods of 120 s - 800 s. We also identify several artifacts in the PPSD, most notably a bimodal behavior, or a bifurcation, in power for periods  $<80$  s, in some DART stations. We conclude that this is most likely due to changes in the DART stations themselves

(i.e., upgrades of the bottom pressure recorder to DART II or DART 4G). Finally, we discuss the implications of spatiotemporal varying BOOTS slope.

## 3.2 Data and Methods

**3.2.1 The DART station system and PPSD measurements of the BOOTS.** To test the hypothesis of the  $\omega^{-2}$  reference power advocated by previous literature, we utilize the DART bottom pressure recorder (BPR) quality-controlled data provided by the National Centers for Environmental Information (NCEI) (*Deep-Ocean Assessment and Reporting of Tsunamis (DART(R))*, 2005). In real-time operations, DART stations operate using event detection to trigger changes in sampling rate. This variability in sample rates is unsuitable for this study, however, the bottom pressure recorder (BPR) component of the DART system continuously logs 15 s sampled data. This data is periodically retrieved by NOAA oceanographic vessels and archived. We thus limit our analysis to include the time periods where BPR data with a 15 s sampling rate are available (Figure 10). We do not use days where data are at sampling rates  $> 15$  s. We then ingest day long segments of the time series into the PPSD calculation following the approach detailed by McNamara and Buland (2004). This approach is desirable because it does not require any cleaning or removal of artifacts in the data. No filter or removal of tidal signals is applied to the data — data are quality-controlled. We measure the PPSD from the periods of 30 s to 2 hrs, and then calculate the PPSDs for the 34 DART stations shown in Figure 11. We elect to

use period in seconds in order to be parsimonious with the various methods applied by referenced literature and this study.

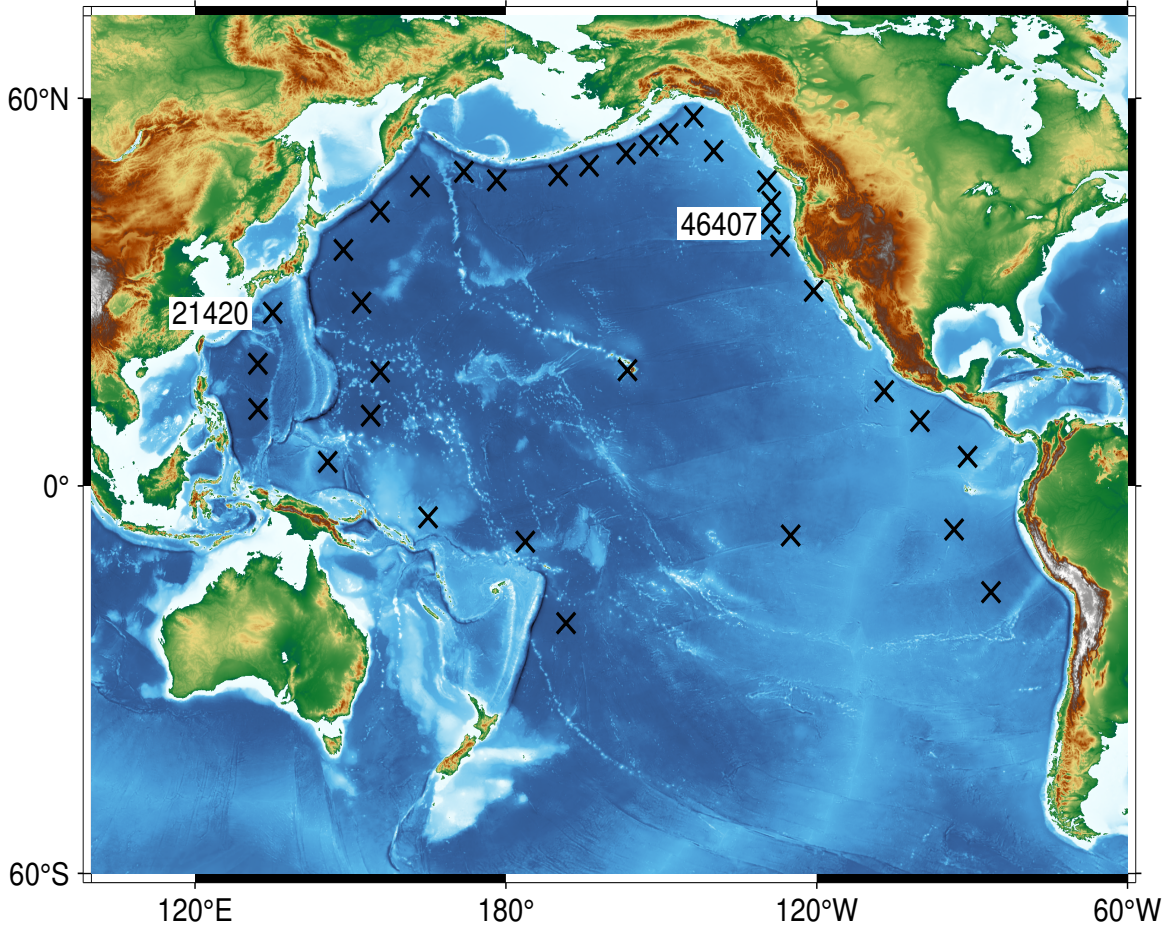


*Figure 11.* Crosses mark the locations of the DART stations used in this study. DARTs 21420 and 46407 are highlighted because they are emblematic (21320) and non-emblematic (46407) to the reference power law of  $\omega^{-2}$ . BOOTS slope values.

### 3.2.2 Measuring temporal variations in the BOOTS. We

calculate the spectral slope and intercept of the BOOTS in two week intervals with the multitaper spectral power spectral density (MT-PSD) methods detailed in Prieto (2022). We calculate the BOOTS intercept, as it provides a simple single parameter reference for the amount and type of noise present in the sampled time

period (Rabinovich, 1997). We choose two week intervals to capture the apparent seasonal variations of the BOOTS and to minimize noise from daily and weekly oceanographic and meteorologic phenomena. We perform a least squares fit of the BOOTS spectral slope between the periods of 12 min - 100 min. We find that, generally speaking, the PPSDs for the DART stations fit on a spectrum between two archetypal behaviors: BOOTS with mostly linear behavior (Figure 12a) with slope values near what the earlier literature (Filloux et al., 1991; Kulikov et al., 1983; Rabinovich, 1997) described (a shape we refer to as "convex") and those that experience a large amount of variation and departure from the log-linear model (what we refer to as "dromedary") (Figure 12b), particularly between the periods of 120 s - 800 s. The lower bound of 12 min was selected as it is the period when the dromedary shape of the PPSD (see Figure 12b) begins to taper off, and it is outside of the upper limit of 600 s (10 min) in the IGW band described by Aucan and Ardhuin (2013). We select an upper limit of 100 min to minimize any long period noise effects. As with the PPSD method, we use only data when sampling rates are at 15 s. In order to minimize tsunami effects, we do not calculate the BOOTS slope when a tsunami occurs within a two week measuring period and for the next two week period afterwards. Tsunami coda effects can be discernible for days after tsunamigenesis due to bathymetric and coastline effects both regionally (Melgar & Ruiz-Angulo, 2018) and globally (Kohler et al., 2020). We use the tsunami database provided by the *National Geophysical Data Center / World Data Service: NCEI/WDS Global Historical Tsunami Database* (n.d.) to filter

out tsunamis generated by earthquakes  $\geq M_w 7.0$ , landslides, and volcanoes. This procedure ensures that we are measuring background noise.

**3.2.3 Measurement of IGWs with DART stations.** Rawat et al. (2014) utilize numerical models and in situ measurements of DART data to track IGW events across the Pacific basin. There they show via tracking of IGW burst events that IGW production is highest in the area of the CSZ, producing some of the largest IGW values in the Pacific basin. We use the data preparation method from Aucan and Ardhuin (2013) which assumes that bottom pressure recordings at IGW periods are free of pressure effects from wind-driven waves and thus that the DART BPR data can be used to extract IGW heights at those periods. Following their approach, we consider that we are examining free monochromatic waves of wavenumber  $k$  and that we can relate the bottom pressure amplitude  $p_b$  to the surface amplitude elevation  $a$  via a transfer function  $M$ , which is a function of water depth  $D$ , with the equation:

$$p_b = aM = a \frac{\rho g}{\cosh(kD)}, \quad (3.1)$$

where  $\rho$  is water density and  $g$  is gravity acceleration. We relate wavenumber  $k$  to wave frequency  $f$  via Laplace's dispersion relation,  $(2\pi f)^2 = gk \tanh(kD)$ . We use Prieto (2022)'s multitaper code to produce power spectral densities  $F_p(f)$  of the DART BPR data. The BPR data are subject to the same constraints as to when the BOOTS slope and intercept were calculated in section 2.2. The transfer

function  $M$  is applied to the power spectral densities to obtain the surface elevation spectral density:

$$E(f) = M^2 F_p(f). \quad (3.2)$$

We then solve for the significant IGW height, which is defined as the partially integrated spectrum:

$$H_{IG} = 4 \sqrt{\int_{f_{min}}^{f_{max}} E(f) df}. \quad (3.3)$$

We choose the same  $f_{min}$  and  $f_{max}$  as Aucan and Ardhuin (2013), setting them to  $8.3 \times 10^{-4}$  Hz and  $1.1 \times 10^{-2}$  Hz, respectively. As we did not remove tsunami signals prior to calculating the significant IGW heights, we remove them and the 6 following days from the dataset. For each station, we calculate the time averaged  $H_{IG}$  for the time periods of JJA and DJF.

### 3.3 Results

**3.3.1 PPSD behavior of the BOOTS.** The BOOTS intersects with what is traditionally considered the IGW band in the periods from 60 s to 600 s (Aucan & Ardhuin, 2013; Rawat et al., 2014; Webb et al., 1991). Figure 12a shows the PPSD for DART 21420 — located 480 km southeast of Miyazaki-shi, Japan, Figure 11. This station’s behavior is best emblematic of the behavior expected from the  $\omega^{-2}$  reference power law. Its mean slope value is  $2.03 \pm 0.19$ , and its mean intercept value is  $10^{-4.48 \pm 0.35}$  (Table S1). We observe from Figure 12a that even

for this relatively "well behaved" site the PPSD is not an exact straight line; it can have non-negligible variation of as much as 5-10 dB in the 120 s - 250 s band, giving the PPSD a convex appearance.

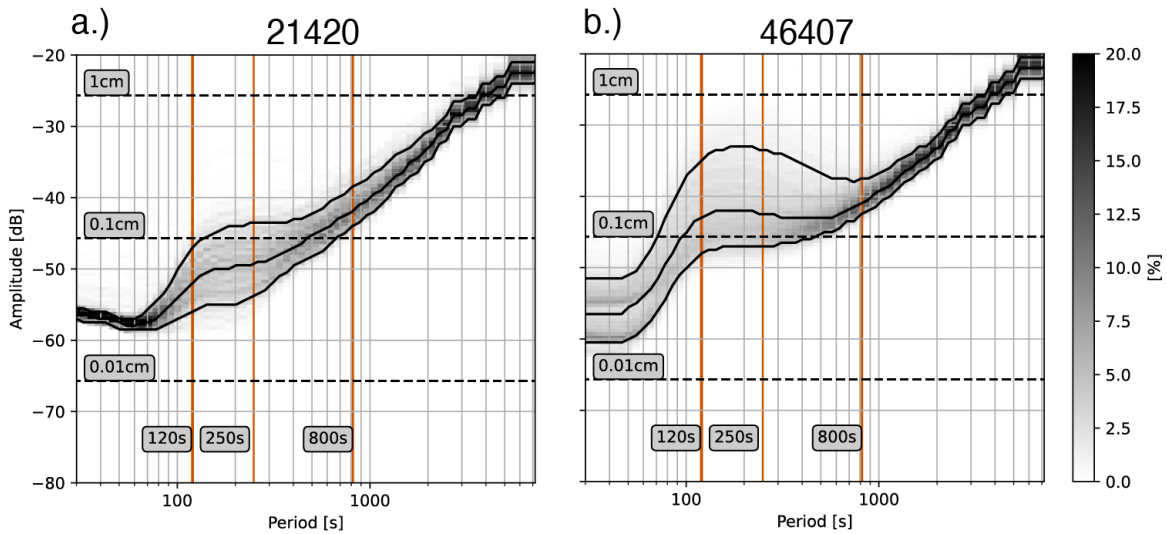


Figure 12. a.) Probabilistic Power Spectral Density (PPSD) plot for DART 21420 — emblematic of behavior that follows the reference power law of  $\omega^{-2}$ . Amplitudes corresponding to noise levels of 1 cm, 0.1 cm, and 0.01 cm are shown as dashed, black lines. Periods corresponding to 120 s, 240 s, and 800 s are delineated by solid, orange lines. b.) PPSD for DART 46407 — emblematic of behavior that does not follow the reference power law of  $\omega^{-2}$ . Amplitudes corresponding to noise levels of 1 cm, 0.1 cm, and 0.01 cm are shown as dashed, black lines. Periods corresponding to 120 s, 250 s, and 800 s are delineated by solid, orange lines.

Figure 12b shows the PPSD for DART 46407 — located 390 km to the west of Coos Bay, OR (Figure 11). Its behavior is dromedary in appearance — with variability as high as  $\sim 15$  dB variability and hummocky between the periods 120 s - 800 s — and a significant departure from the  $\omega^{-2}$  reference power law, in stark contrast of DART 21420 ( Figure 12a). Its mean slope value is  $1.90 \pm 0.22$ , and its mean intercept value is  $10^{-4.25 \pm 0.40}$  (Table S1). Critically, Figure 12b indicates that amplitude spread for periods between 120 s - 800 s is considerable between the

10<sup>th</sup> percentile and the 90<sup>th</sup> percentile, which may be evidence of external forcing. Lastly, DART 46407 has an enigmatic bifurcation in its PPSD for periods < 80 s. Something that is not observed in the PPSD of DART 21420 (12).

DART 46407’s PPSD suggests that the  $\omega^{-2}$  power law is a poor fit for modeling the BOOTS between the periods of 120 s - 800 s, coincident with the IGW band’s 60 s - 600 s ((Aucan & Arduin, 2013)). This deviation from the expected trend has been noted in previous literature, resulting in them only using the reference power law from periods of only 10 mins - 120 mins (Rabinovich, Candella, & Thomson, 2011; Rabinovich & Eblé, 2015). However, it can be seen in Figure 12 that there are possible effects even in the shorter periods of that range, potentially from IGW power leaking into this band. The BOOTS extends from 2 mins - 120 mins — which includes potential IGW interactions — so it is imperative to constrain what these effects are for shorter periods within the BOOTS.

### 3.3.2 Spatiotemporal variations in the BOOTS.

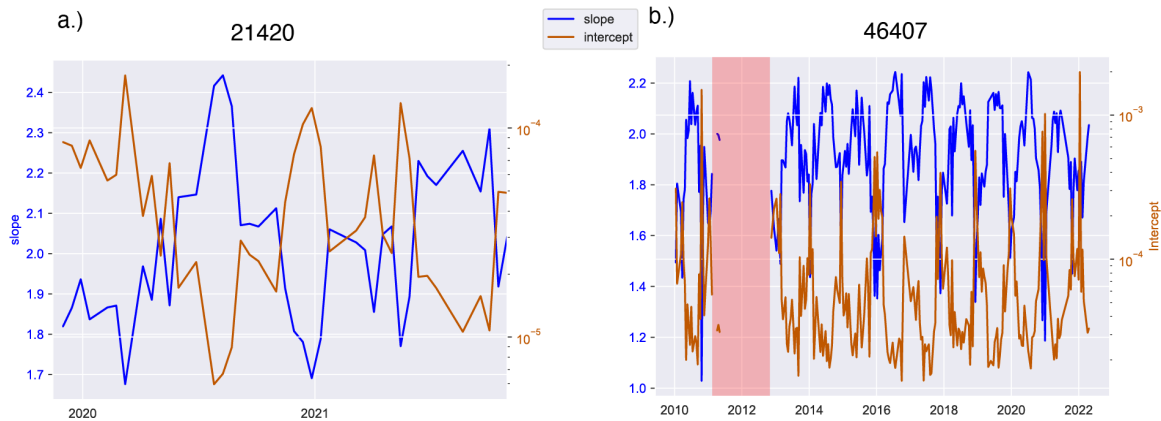
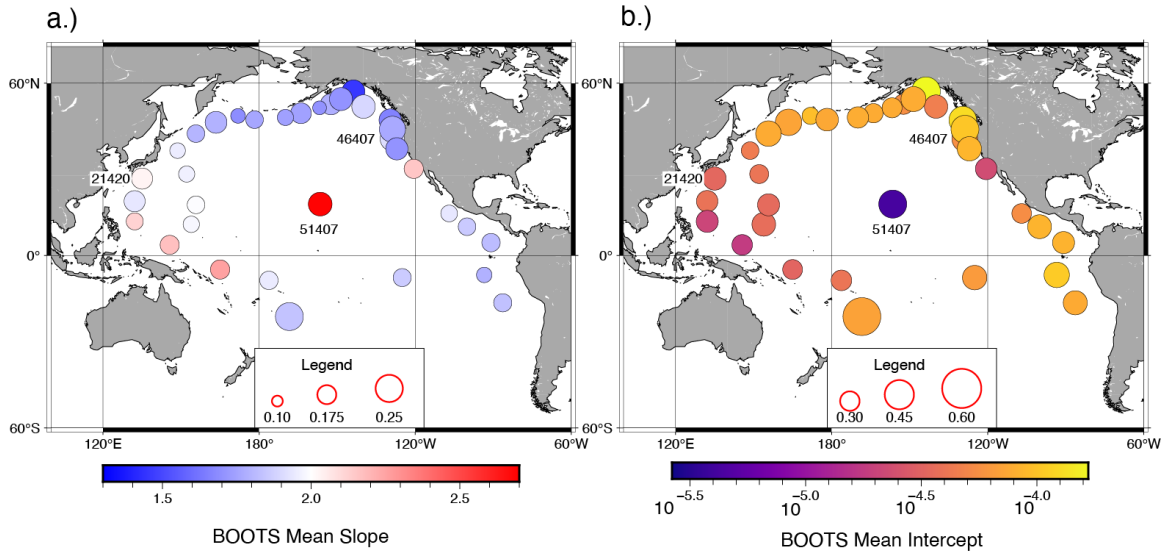


Figure 13. a.) 21420 time-series of BOOTS slope (blue) and intercept (orange). b.) 46407 time-series of BOOTS slope (blue) and intercept (orange). Period of low-quality data, resulting in no values for either parameter, is shown in red.

**3.3.2.1 Temporal variations in the BOOTS.** We observe from Figure 13a that DART 21420 experiences some amount of seasonal variation over the course of its deployment from December 2019 to October 2021. It achieves maximum slope values  $> 2.3$  during the time period of JJA; meanwhile, it obtains minimum slope values  $< 1.8$  during the time period of DJF. We note that there is a seemingly inverse relationship between the maximum/minimum values for the BOOTS slope and intercept. Lower magnitude intercept values have been attributed to periods of less atmospheric noise (Rabinovich, 1997), meaning periods of calm weather correspond to high BOOTS slope values. We note that the period of minimum BOOTS slope values corresponds to extratropical cyclone season for the north Pacific. However, the length of record for DART 21420 is a modest 2 years long compared to other stations we analyze (Figure 10).

Figure 13b shows a much longer 12 year time series showcasing rich seasonal variation of bottom pressure for DART 46407. It obtains maximum slope values in JJA  $> 2.2$  and minimum slope values in DJF  $< 1.4$ . While partially evident in Figure 13a, Figure 13b demonstrates the seemingly inverse nature of the BOOTS slope and intercept over a much longer period of record — January 2010 - April 2022. As discussed earlier, lower magnitude intercept values correspond with less atmospheric noise and vice versa. Figure 13b indicates that JJA is period of seasonally calm atmospheric noise while DJF is a period of disturbed atmospheric noise. Similar to DART 21420, DART 46407's seasonality appears to coincide with the extratropical cyclone season in the north Pacific, which multiple sources

attribute to producing IGW events (Aucan & Ardhuin, 2013; Rabinovich & Eblé, 2015; Rawat et al., 2014; Webb et al., 1991).



*Figure 14.* a.) Mean slope of the BOOTS across the Pacific basin for each station's entire temporal coverage. Color of the circle corresponds to the mean value of the BOOTS slope. Circle size corresponds to the standard deviation of the slope. b.) Intercept of the BOOTS across the Pacific basin. Color of the circle corresponds to the mean value of the intercept. Circle size corresponds to the standard deviation of the intercept.

We demonstrate in Figure 14 that the other DART stations fall somewhere between the previously demonstrated behaviors. We note that sites with behavior similar those similar to DART 21420 are its neighbors in the southwest Pacific. Similarly, DART 46407's neighbors in the northeast Pacific exhibit similar behaviors. The exception to this trend is DART 51407 — the DART nearest Hawai'i, Figure 11. This station is notable for the sheltering effect it experiences from the Big Island (Rawat et al., 2014; Webb et al., 1991). It is not affected like other DART stations by meteorological events in the north Pacific, naturally

filtering out the noise in the BOOTS. However, we find it is susceptible to meteorologically induced IGW events from the south Pacific and the east Pacific — west of Mexico and Central America.

**3.3.2.2 *Spatial variations of power in the BOOTS.*** As previously mentioned, DART stations 21420 and 46407 experience varying degrees of seasonal variations with other stations falling on a spectrum between the two. We show that the stations in the north Pacific experience to varying degrees maximum slope values during JJA and minimum slope values during DJF (Figure 15). The trend is reversed for stations from off the coast of Mexico to off the coast of Peru and in the south-central Pacific. For these reasons, for examining the spatial variations of the BOOTS, we split the time periods into DJF and JJA. We further focus our attention to the periods of 120 s (the start of the tsunami band), 250 s (the middle of the dromedary hump), and 800 s (where the dromedary hump abates and end of the IGW band).

We see from Figure 15a that the median power at the period of 120 s is in the -55 - -50 dB range for most of the north Pacific. The southwest Pacific is where background noise is at a global minimum for the JJA and DJF months. The region of the Cascadia Subduction Zone (CSZ) has higher power than the rest of the north Pacific, being between -50 dB - -45 dB during JJA. The area has the highest powers for the Pacific basin being <-40 dB during DJF. The DART stations in the southern hemisphere and off the coast of Central and South America achieve their highest power values at 120 s during JJA and lessens only slightly during DJF. The

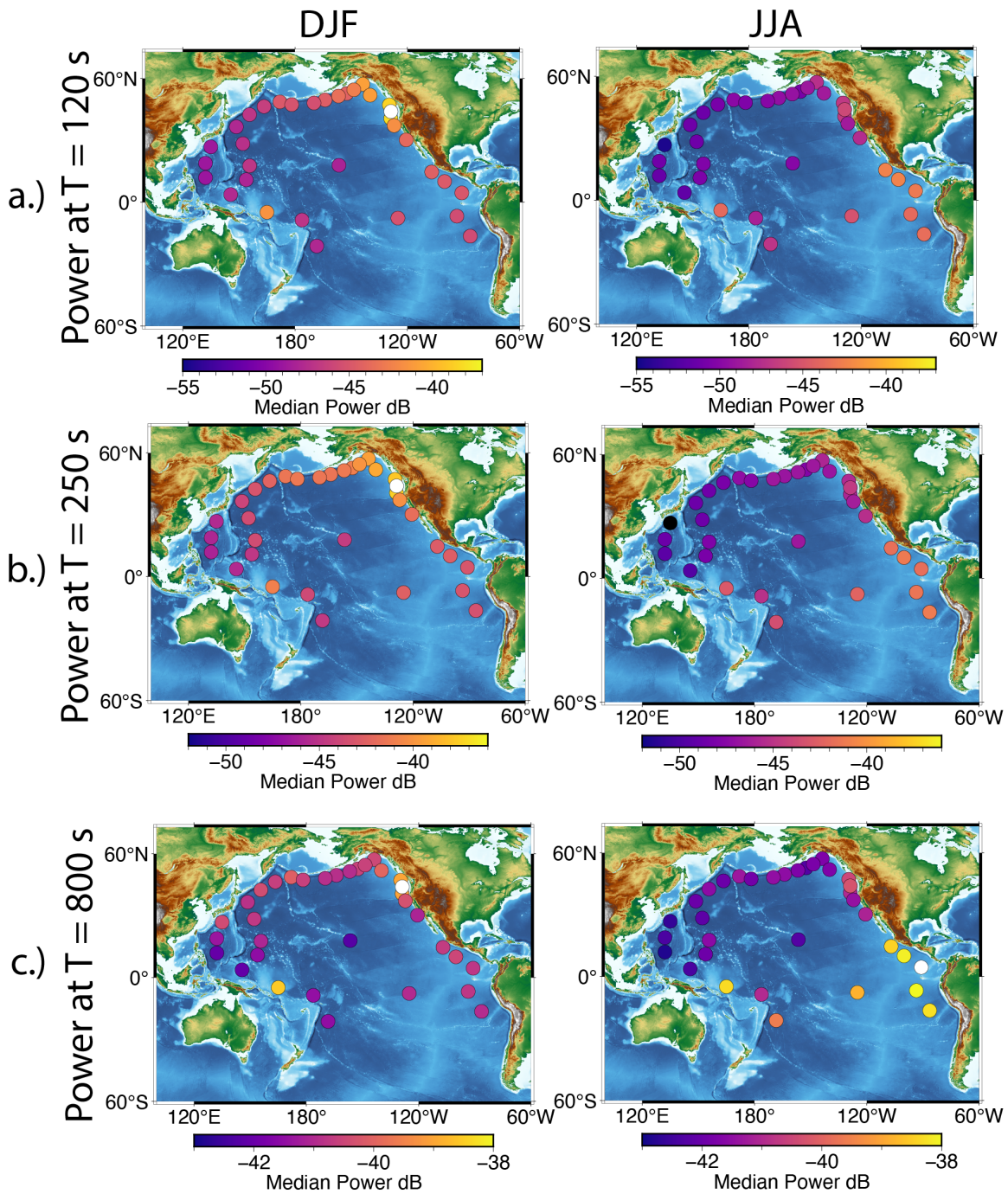


Figure 15. a.) Median power in dB at a period of 120 s. Top panel is median power during JJA, and bottom panel is median power during DJF. b.) Median power in dB at a period of 250 s. c.) Median power in dB at a period of 800 s.

DJF period demonstrates that there is an apparent eastward increase in power for the 120 s period, which is not present during JJA.

For the median power at the period of 250 s, we observe a similar behavior to that of 120 s period. At this period the Aleutian Islands and Gulf of Alaska DART stations join the stations off of the CSZ in having values  $< -41$  dB. Whereas at 120 s, there was a gradual increase in power, they are in the same range of  $-41$ – $-38$  dB, Table S1. The CSZ DART stations still produce the maximum power value of  $-35.7$  dB at DART 46404. The DART stations east of the Izu-Ogasawara and Marianas Trenches have higher power than those to the west. This could be due to the sheltering effect the trenches and their islands produce from storms in the open ocean during DJF. This effect appears to be minimal.

We find that when the PPSDs are mostly no longer affected by the dromedary hump at the longer periods. For example, at 800 s a more unique spatial variation is present. In the vicinity of DART 21420, the stations closest to Japan have a higher value than those to the south during DJF. In fact, the power is higher at the stations from 21420 all the way to the stations in the far east Aleutian islands. We espy that the dromedary hump has not completely relaxed at the period of 800 s for these stations. Whereas there was a minimal sheltering effect produced by the Izu-Ogasawara and Marianas Trenches during DJF in the other periods, this effect is not present for the period of 800 s. We discern that DART 52406, in the south Pacific, is a station with power  $> -39$  dB in both JJA and DJF for the region. We recognize that the station's BPR is located in comparatively

shallow water (1800 m) which may play a role in why it has higher power than its neighboring stations. Generally, it follows from Laplace’s dispersion relation that the deeper a station is, the more the more the water column attenuates short period signals. Since the depth of this BPR is shallower than those of other stations, it is more susceptible to short period noise that would otherwise be attenuated. Hemispherical differences in power are the most apparent of all periods at a period of 800 s in JJA. As with the previous periods, the CSZ DART stations continue to be the region of highest power during DJF. Finally, we pinpoint, again, that DART 51407 has low power during both JJA and DJF due to the sheltering effect of the Hawaiian Islands.

### 3.4 Infragravity waves in the BOOTS

Next, we show that the chief driver of the spatiotemporal variability of the BOOTS slope and intercept are most likely IGW.

#### 3.4.1 Spatiotemporal Effects of IGWs.

We find that the highest values of  $H_{IG}$  and the strongest seasonality are in the northeast Pacific within the Gulf of Alaska and in the area of the CSZ (Figure 16).  $H_{IG,DJF}$  is a factor of 2-3 larger in these regions than  $H_{IG,JJA}$ . We observe that  $H_{IG}$  values decrease westward from the Gulf of Alaska and the CSZ. Aucan and Ardhuin (2013) attribute this effect to the convex shape of the Alaska peninsula and the Aleutian Islands, where IGW free energy can disperse over a wider ocean region. Our areas of high  $H_{IG}$  are in line with the values measured by Aucan and Ardhuin (2013) and Rawat et al. (2014).

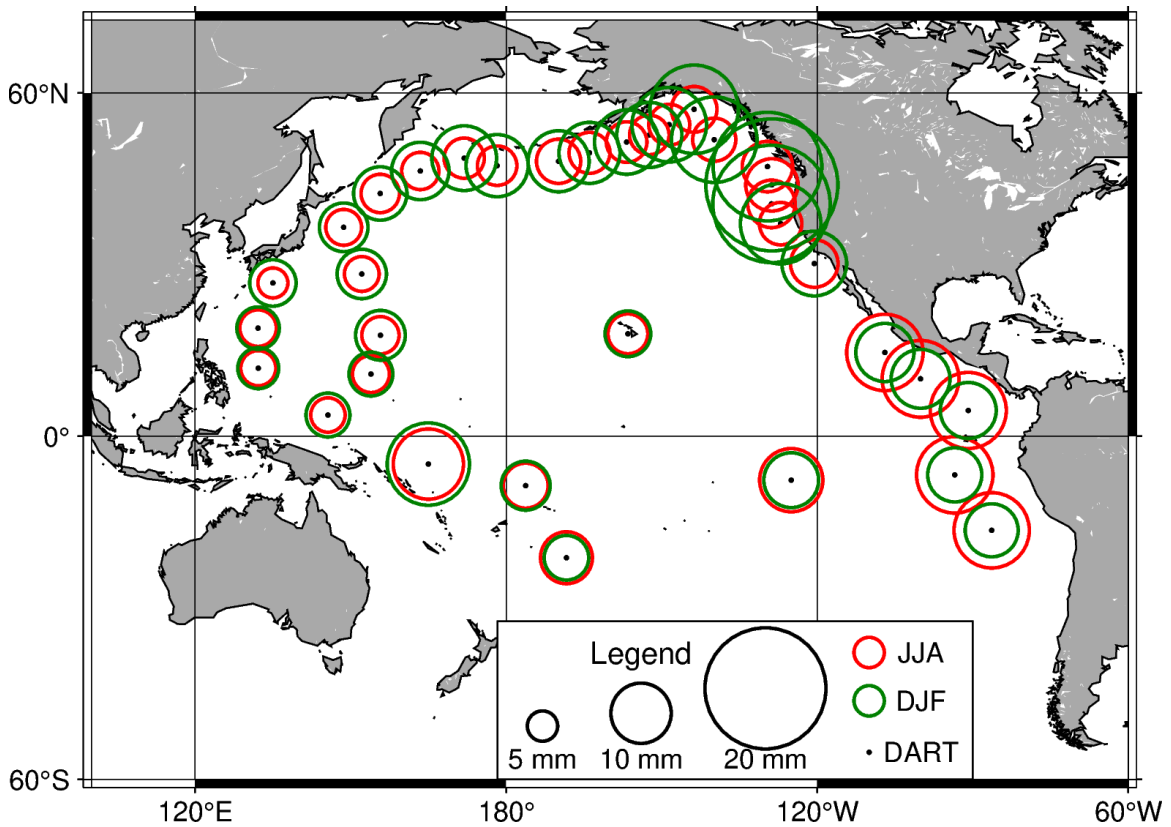


*Figure 16.* Infragravity wave heights for the time periods of JJA (red circles) and DJF (green circles). DART locations are shown as black dots.

We find that, in the lower latitudes of the Pacific, the values of  $H_{IG}$  are lower and have a less pronounced seasonality. From Mexico to Peru,  $H_{IG}$  have a reversed seasonality signal. This result is in line with the results of Aucan and Ardhuin (2013); Filloux et al. (1991); Rawat et al. (2014). However, we find, in addition to austral winter storms in the south Pacific, that tropical systems are another likely source of IGW events.

### 3.5 Data artifacts in the BOOTS

#### 3.5.1 Tsunami signals.

We have shown that there are other signals present in the BOOTS that are not tsunami signals that produce significant variations in amplitude between the periods of 120 s - 800 s. However, what remains to be clear are potential impacts of these signals on tsunami signals. In order to do so, we pick out 3 tsunamigenic earthquakes to observe the type of signals they produce in the DART stations' PPSDs. We focus our attention on DART 46407, since it is among the stations that experiences the highest  $H_{IG}$  values in the period of DJF.

We choose the 2020  $M_w$ 7.8 Simeonof, 2020  $M_w$ 7.6 Sand Point, and 2021  $M_w$ 8.2 Chignik earthquakes (17). The  $M_w$ 7.8 Simeonof and  $M_w$ 8.2 Chignik earthquakes both occur in July, which is when  $H_{IG}$  are at their lowest values for the Aleutians and the CSZ. The  $M_w$ 7.6 Sand Point earthquakes occurs in October, which is when  $H_{IG}$  begin to become higher leading into DJF, Figure 12. The  $M_w$ 7.6 Sand Point signals are shown twice, as the earthquake occurred near the end of the UTC day. We see from Figure 18 that Simeonof experiences a slight

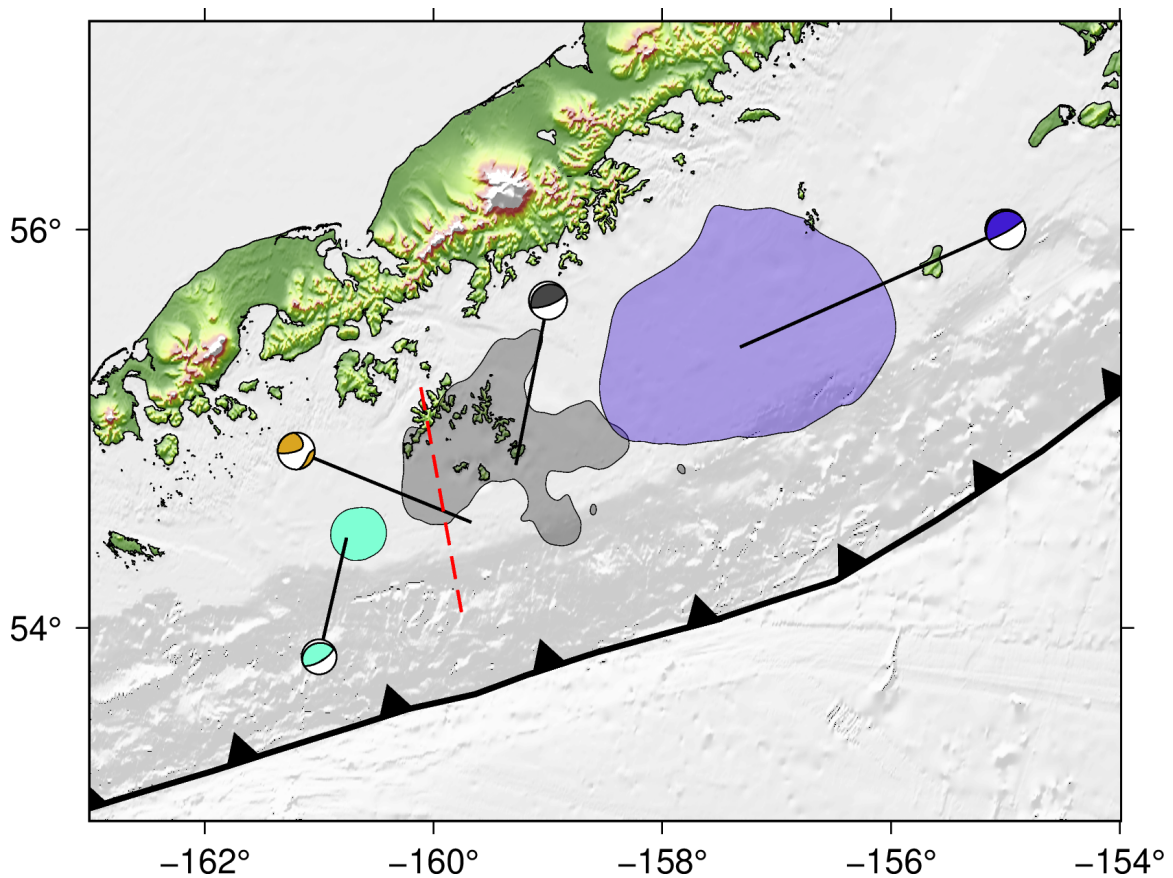


*Figure 17.* The 2020 Simeonof rupture zone from Crowell and Melgar (2020) is shown in black, the 2021 Chignik rupture zone from the USGS-National Earthquake Information Center (NEIC) finite fault model for the event is shown in dark blue, and the rupture area for the July 15, 2023, Sand Point earthquake from the USGS-NEIC finite fault model is shown in aquamarine (U. S. Geological Survey, 2017). The surface projection of the strike-slip plane associated with the 2020 Sand Point earthquake is delineated by a dashed red line.

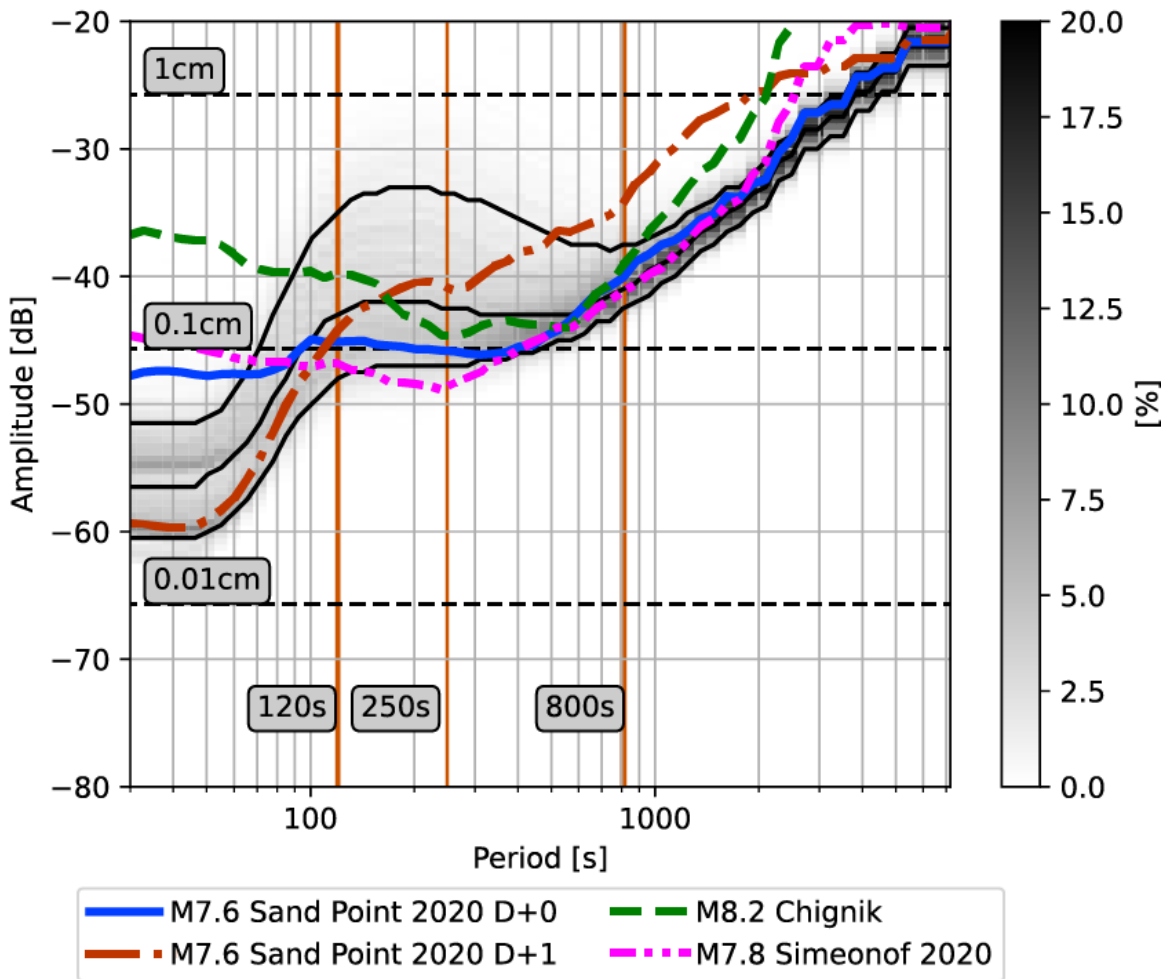


Figure 18. DART 46407 PPSD. The 2020 M7.8 Simeonof earthquake is shown by a dash-dot-dot magenta line (UTC Day July 22, 2020). The 2020 M7.6 Sand Point earthquake is shown in blue (UTC Day October 19, 2020) and by a dash-dot crimson line (UTC Day October 20, 2020). The 2021 Chignik earthquake is shown by a dashed green line (UTC Day July 21, 2021).

reduction in power at 250 s, and it is below the 10<sup>th</sup> percentile of noise between 120 s - 400 s. Sand Point's apparent short period signal is slightly lower in power than that of Simeonof and Chignik. Yet, its signal between 170 s - 1100 s is larger than either event. We note that there is no reduction in power in the signal between 120 s - 400 s like with Simeonof or Chignik. Chignik's short period power is larger than both Simeonof and Sand Point, but as mentioned previously with Simeonof, its power between 120 s - 800 s experiences a similar reduction in power.

$H_{IG}$  values 24 hours prior to the Simeonof earthquake were between 6-7 mm. The event itself did not elevate  $H_{IG}$  by a noticeable amount, even in the days immediately after the event. Whereas,  $H_{IG}$  values after the Sand Point and Chignik earthquakes have amplitudes of 15 mm and 13 mm, respectively. The difference for Sand Point and Chignik is that the background  $H_{IG}$  values were 1-2 mm higher in the days before Sand Point than in the days prior to Chignik. We discuss ,later, potential impacts of the IGW band on the BOOTS.

**3.5.2 Bifurcation of PPSD in short periods.** The apparent bifurcation of the PPSD for 46407, as with other stations where it occurs, at first seems complex. We investigate whether it is the result of differing deployment locations of the DART BPR. Frequently, after a DART site is maintained or overhauled the new buoy and BPR can end up in a different location than prior to the work being done on it. We find, at maximum, that new BPR deployments are between 20-30 km of the previous deployment location. In the example of 46407, its location is on the abyssal plain — far from any complex structures, as seen

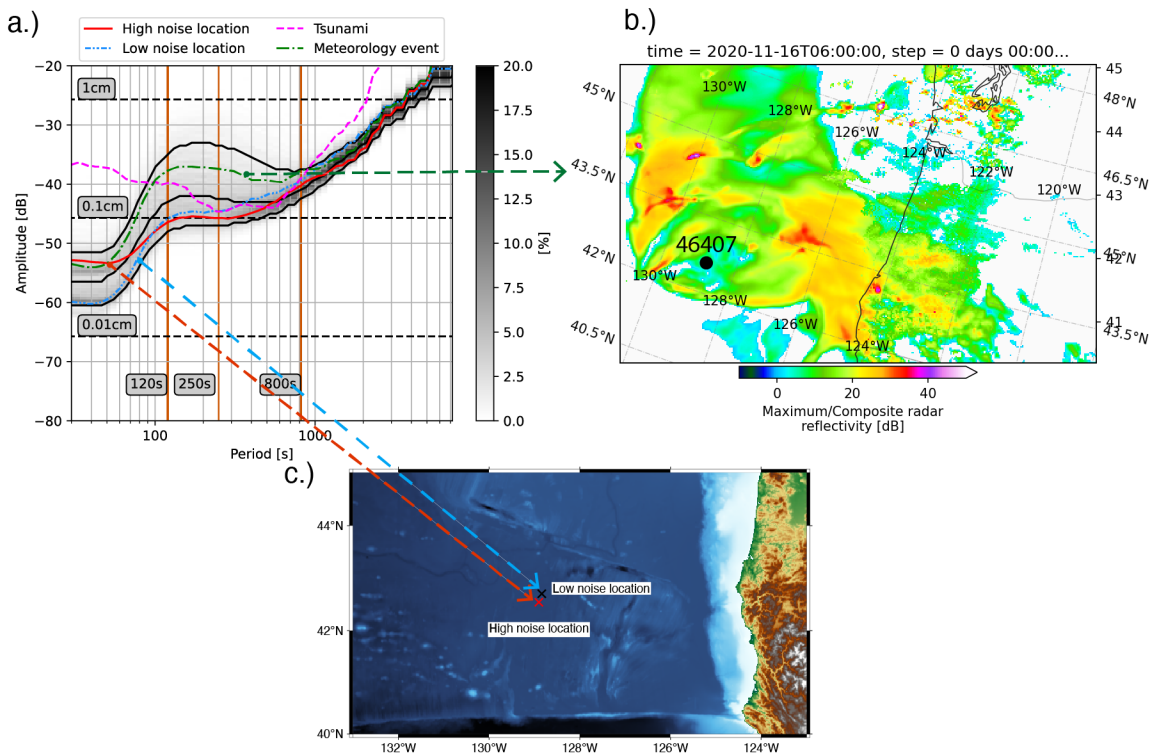


Figure 19. a.) PPSD for DART 46407. High noise location (red), low noise location (dash-dot-dot blue), meteorological event (dash-dot green), and tsunami (July 22, 2021 Chignik earthquake, dash magenta) PSDs are plotted for their respective occurrences. Arrows point to their respective phenomena in panels b.) and c.). b.) Meteorological event that occurred on November 16, 2020, at 0600 UTC which produced noise above the 10th percentile in the BOOTS. Maximum/Composite radar reflectivity from the 0600 UTC High Resolution Rapid Refresh (HRRR) model is shown. c.) Location of DART 46407 at a high noise location (UTC Day May 17, 2011, red x) and a low noise location (UTC day July 7, 2021, black x).

in Figure 19c. We choose two days and compare their PPSD signals with each other. One when the DART was located in a high noise location (2011/05/17) and in a low noise location (2021/07/07). Ultimately, we find the solution to the bifurcation in the metadata for the BPR data. It was upgraded to a lower noise floor instrument over the span of 10 years, so the apparent bifurcation is a symptom of the sensor itself being upgraded and not due to a change in location. We find that this is the case for all BPR data that spans  $>5$  years. The apparent bifurcation abates for periods longer than 80 s, so it does not pose an issue for examining signals that reside in the BOOTS. Although, it may pose an issue to those using the data for long term investigations of IGW events.

### 3.5.3 Meteorological impacts on the BOOTS.

Numerous works in the literature describes that IGWs and the BOOTS are impacted by meteorological events yet refrain from showing these systems' meteorological set ups (Aucan & Ardhuin, 2013; Filloux et al., 1991; Kulikov et al., 1983; Rabinovich, 1997; Rawat et al., 2014). Here we use weather model output to connect days of high  $H_{IG}$  values to specific types of meteorological systems. We choose the High Resolution Rapid Refresh (HRRR), European Centre for Medium-Range Weather Forecasts (ECMWF) weather and wave models, and the Global Ensemble Forecast System (GEFS) to investigate storm systems across the Pacific, where we have shown in earlier sections that  $H_{IG}$  values are high. We utilize a variety of models due to the varying availability of model output for the time duration of our study. Model output is not always available for the time period

of 2006-2022 due to storage or open data availability issues. Model output are processed using Herbie (Blaylock, 2024; Blaylock, Horel, & Liston, 2017).

For the HRRR model, we visualize storms systems by using the maximum/composite radar reflectivity. For the ECMWF wave model, we visualize storm systems with the significant height of combined wind waves and swell forecast and geopotential height at 850 mb pressure level with 10 m winds plotted to visualize the wind field of the tropical and extratropical systems. For the GEFS, we use the mean member pressure reduced to mean sea level with 10 m winds plotted to visualize the wind field of the tropical and extratropical systems.

Figure 19b shows an archetypal, modest extratropical storm that affects the CSZ during November. These types of storm systems occur frequently during this time of the year; however, their strength is variable. This storm system was responsible for  $H_{IG}$  of 11 mm for November 16, 2021. In the immediate days ahead of the storm system,  $H_{IG}$  values were as high as 14 mm. These systems do not need to transit directly over the DARTs to elicit such high  $H_{IG}$  values. As noted by Hanafin et al. (2012), storm track and intensity are crucial factors in IGW event generation for this region. We find that events that make landfall on the North American coast between  $40^\circ$  and  $60^\circ$  produce IGW events of varying intensity.

Figure 9a shows the ECMWF significant height of combined wind waves and swell for an extratropical storm that transits through the Gulf of Alaska during February. Storm systems that transit through this region are strong enough to elicit high  $H_{IG}$  values at the CSZ DART stations. They have significant height of

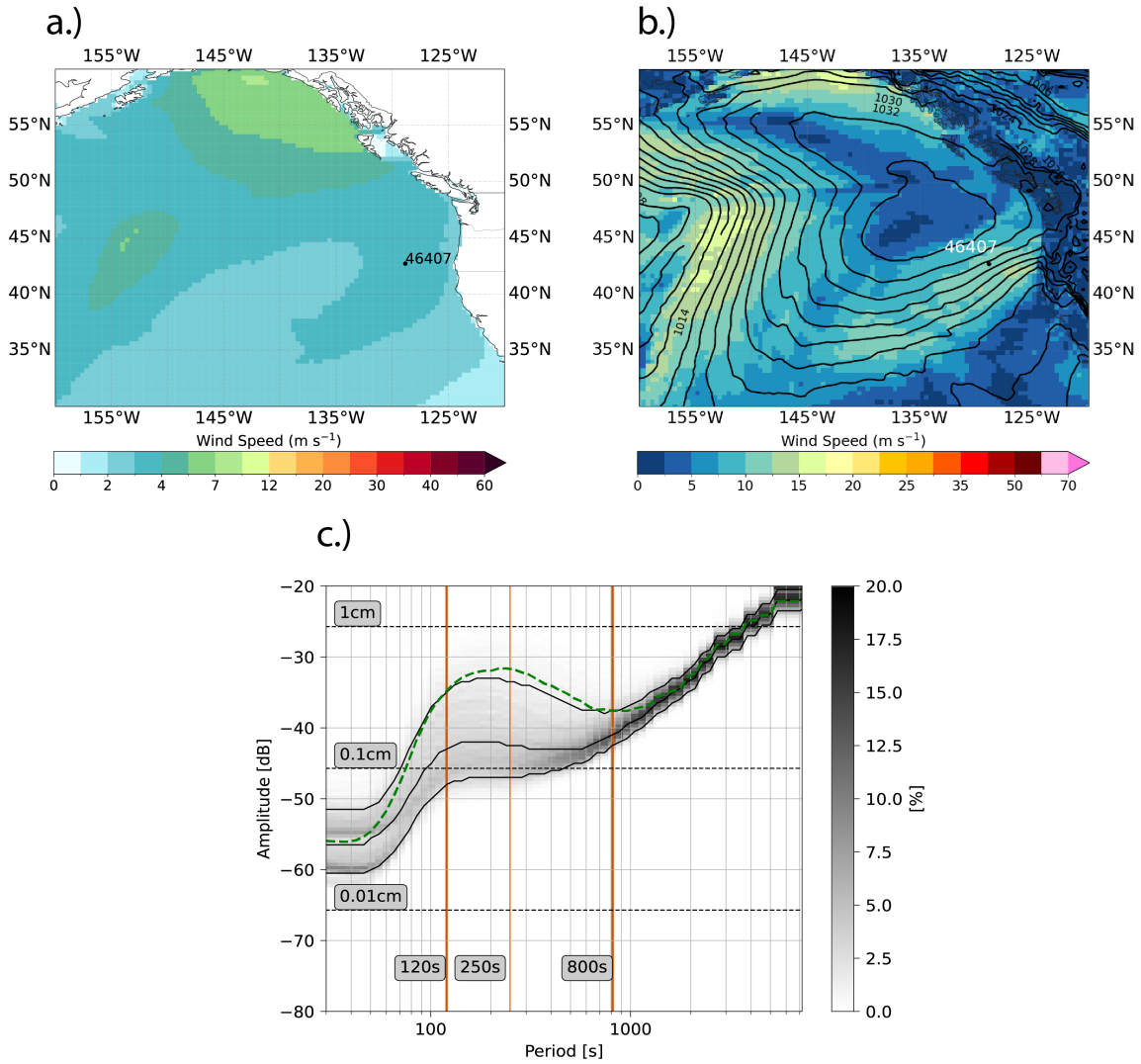


Figure 20. a.) ECMWF wave height model at  $0.5^\circ$  resolution for February 10, 2022 at 12 UTC. DART 46407 is shown by a black dot. b.) ECMWF model at  $0.5^\circ$  resolution for February 10, 2022 at 12 UTC. Geopotential height at 850 mbar is plotted at 50 m contours. 10 m wind is shown by filled contours. c.) PPSD for DART 46407 for the meteorological event signal during August 13, 2021. The signal is shown by the dashed green line.

combined wind waves and swell of 10-12 m in the Gulf of Alaska, yet only produce heights of 3-4 m over the CSZ. As Aucan and Ardhuin (2013) and Rawat et al. (2014) note, these storm systems produce conditions favorable for IGWs due to their storm track and intensity. For the February 10, 2022 storm, the system's center is located at 142°W and 60°N, yet it is producing widespread IGW impacts across the area, in spite of a high pressure system that has set up at 135°W and 45°N, Figure 9b and 9c. Low wind speeds in the high pressure area do not efficiently generate wind waves, so the wind generated waves and swell from the extratropical system can transit across the area with little to no impact.

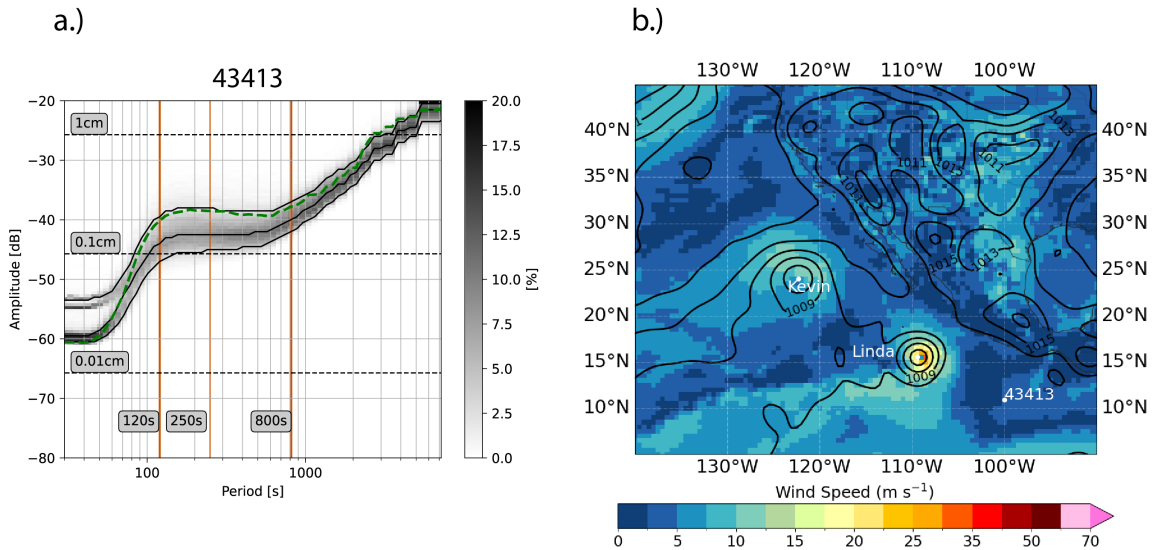


Figure 21. a.) PPSD for DART 43413. Meteorological event signal for August 13, 2021 is shown by the dashed green line. b.) GEFS model at 0.5° resolution for August 13, 2021 at 12 UTC. 10 m wind is shown to visualize the wind field of the tropical systems. Pressure reduced to mean sea level (MSL) pressure is shown by the black contours. Contours are plotted at 2 mbar intervals. DART 43413 is shown by a white dot. The approximate locations of tropical storm Kevin and Hurricane Linda's cores are shown by white dots.

In contrast, DARTs 43413 and 43412 show evidence for IGW events forced

by tropical systems. Figure 10 shows the PPSD and PPSD signal for DART 43413 as Tropical Storm Kevin and Hurricane Linda pass to the northwest of the station. As seen with the CSZ DARTs, the stations along the Middle and South America Trenches experience higher  $H_{IG}$  values when transit close to the stations. Higher  $H_{IG}$  values for the DART stations off of South America are also experienced due to austral winter storms in JJA in the southern hemisphere.

### 3.6 Discussion

#### 3.6.1 The magnitude of the BOOTS slope.

The variety of data used in this study lead to an inescapable conclusion: the BOOTS slope does not uniformly follow a reference power law of  $\omega^{-2}$ , even when we limit its use to periods where IGW forcing is minimal from the PPSD. Therefore, we posit that the BOOTS varies spatiotemporally, majorly as a function of IGW forcings going from short period to long period within the BOOTS. Characteristic of this effect is the presence of a dromedary hump for periods of 120 s - 800 s at DART stations in the north and east Pacific regions. We recognize that this hypothesis is seemingly at odds with earlier literature. However, we find that certain regions of the Pacific (i.e., the southwest and south central Pacific and offshore California), where PPSD follows an convex behavior, do follow, to some degree the reference power law. In fact, variations from the reference law are smallest during March, April, May (MAM) and September, October, and November (SON) when seasonal signals in the CSZ, Gulf of Alaska, Central America, and South America are in transition seasonal maximums and minimums. Yet still,

other areas, as is the case for DART 21420, experience little variations about the reference law for the whole year.

Explaining the differing behaviors between dromedary and convex background profiles has a simple solution: IGW effects. When we combine our results with the results from Aucan and Ardhuin (2013) and Rawat et al. (2014), we find that stations with dromedary PPSD shapes directly correlate with areas of intense IGW production, Figure 16. And, we find that stations with convex PPSD shapes correspond to those where sheltering from nearby bathymetric and topographic features occur (Rawat et al., 2014). Our results in Figure 16 are in harmony with earlier IGW literature.

### **3.6.2 Implications of meteorological impacts on the BOOTS.**

IGW-genesis from meteorological forcings has long been established from the work of Webb et al. (1991). Kulikov et al. (1983) even refer to the effects of transient weather systems on the noise they recorded during their expeditions. Aucan and Ardhuin (2013) and Rawat et al. (2014) add that winter storms in the Gulf of Alaska and the CSZ as being the biggest producers of high  $H_{IG}$  values in the time frames considered by their studies. Hanafin et al. (2012) found that intensity, duration, and storm track are biggest indicators of large IGW bursts. We have shown that normal extratropical intensification is enough to elicit high values of  $H_{IG}$  in the Gulf of Alaska and CSZ. In addition, we have shown that for stations off the coast of Mexico, Central America, and South America have high  $H_{IG}$  values

due to the East Pacific hurricane season in JJA. In addition elevated values due to austral winter storms in the South Pacific.

Explanations for the high  $H_{IG}$  values in the Gulf of Alaska and the CSZ have already been covered by Rawat et al. (2014). Where they found that extratropical cyclones with predominant westerly winds and waves cause significant IGW events. Figures 9 and 10 show examples of common types of extratropical storm systems. We posit that storm track and duration are the chief contributors to IGW heights in this area. These storms deepened over the Gulf of Alaska and made landfall between  $45^\circ$  and  $60^\circ$  and transited through the Gulf of Alaska over a period of 3-5 days. We found that storm systems that underwent bombogenesis — a 25 mbar drop over a period of 24 hours — prior to landfall did not produce higher than normal  $H_{IG}$  values for DJF. Often these systems deepened within 12-24 hours of landfall right off the coast such that there was not enough time to induce a wide wind field.

We posit that high values of  $H_{IG}$  from Mexico to Peru follow a similar generating mechanism; however, with tropical systems rather than extratropical systems. These systems with predominant easterly winds and waves cause significant IGW bursts for the area. Figure 10 shows a common meteorological set up for the East Pacific in JJA — multiple tropical systems off the coast of Mexico. These storm systems produce winds and waves that radiate outward inducing  $H_{IG} > 15$  mm for the stations in the area. These storm systems even induce seasonal high values in  $H_{IG}$  for stations in the CSZ and even DART 51407 near Hawai'i,

which is sheltered by the Big Island of Hawai'i from extratropical IGW events in the Gulf of Alaska and the CSZ during DJF.

Meteorological forcings that drive IGW bursts are sources of aleatory and epistemic uncertainty in the BOOTS, and, thus, tsunami source models. While it is not possible to know the exact state of these forcings when a potential tsunamigenic earthquake occurs, it is possible to forecast events that drive IGW bursts up to 7 days of lead time (Kalnay, 2002). Future work can focus on combining GFS and ECMWF wave forecasts with the PPSD models of the DARTs to further refine the aleatory and epistemic uncertainty effects of meteorologic effects on tsunami propagation from the open ocean to coastal sites.

### **3.6.3 Implications of a spatiotemporally varying BOOTS.**

We have shown that IGWs have an impact on the BOOTS from 120 s - 800 s, and that these impacts affect the BOOTS slope even when measuring it from 12 mins - 120 mins to reduce IGW effects. We have posited, in agreement with previous literature, that extraoical and tropical systems can lead to IGW generation events. In addition, we have shown that IGW affect the BOOTS slope from 120 s - 800 s. Figure 7 shows the PPSD signatures of 3 earthquakes that produced tsunamis in the Gulf of Alaska and propagated as far as Hawai'i. The 2020 Simeonof and 2021 Chignik earthquakes occurred in July when IGW generation is at yearly low in the north Pacific. From the periods of 120 s - 800 s, these earthquakes' tsunami PPSD signatures experience a reduction in power. In contrast, the 2020 Sand Point Earthquake's tsunami PPSD signature experiences

no similar reduction in power; it appears to increase through the range of periods, Figure 7. The BOOTS slope during July 2020 and July 2021 was  $>2.2$  while the slope was  $<1.8$  during October 2020, Figure 3.

We posit that the IGW band and the BOOTS interact with one another. This hypothesis is not extreme. As Rawat et al. (2014) notes, IGWs are only a few periods shorter than those of large tsunamis. And, both have similar propagation speeds and spatial distribution of amplitudes caused by shoaling and refraction. These similar physical characteristics may lead to interesting interactions. It is possible that the IGW band and tsunami band destructively interfere with one another when the BOOTS slope is  $>2$  and constructively interfere when it is  $<2$ . It would therefore be imperative for tsunami source reconstruction and inversion to take into account these effects in order to obtain high fidelity tsunami source spectra and source regions.

High fidelity BOOTS noise models must take into account IGW effects for automatic detection of tsunami waves. The similar nature of IGWs to tsunamis from 120 s - 800 s, could potentially lead to false positive tsunami detections during meteorological caused IGW events or lead to false negative tsunami detections when IGW events cause large amounts of background noise.

### **3.7 Conclusion**

We have shown that the BOOTS slope does not universally follow a reference power law of  $\omega^{-2}$ . We found that it experiences substantial seasonal variations in the east Pacific from the Gulf of Alaska down to Peru. The chief

contributor to its variation are meteorologically induced IGW events. These events interact with the BOOTS to lower the slope value to be  $< 2$ . In the absence of these events, BOOTS slope values are  $\geq 2$ , with values being closer to 2 in areas outside of the east Pacific. We have proposed that IGW events and their absence may have some interactions with tsunami events that may affect aleatory and epistemic uncertainties for tsunami source models. We have shown that, in addition to extratropical systems in the north and south Pacific, tropical systems in the east Pacific cause IGW events that can be recorded across the Pacific. Finally, we recommend that automatic detection algorithms take into account IGW events, particularly in the Gulf of Alaska and CSZ, as they may eclipse small tsunami signals.

### 3.8 Data availability

DART BPR data is available at <https://www.ngdc.noaa.gov/hazard/dart/>. Records of tsunamis in the Pacific basin are available at <https://data.noaa.gov/metaview/page?xml=NOAA/NESDIS/NGDC/MGG/Hazards/iso/xml/G02151.xml&view=getDataView>. The Herbie python code is available from GitHub at <https://github.com/blaylockbk/Herbie> and archived on Zenodo at Blaylock (2024). The PPSDs were generated using the multitaper python package available from GitHub at <https://github.com/gaprieto/multitaper> and documented by Prieto (2022). Table S1 and other codes necessary for the study are available from GitHub at <https://github.com/ssantellanes/BOOTS> and archived on Zenodo at Santellanes (2024).

### 3.9 Acknowledgements

We would like to thank Aaron Sweeney for helpful discussions on processing DART data. A portion of this work used code generously provided by Brian Blaylock's Herbie python package (<https://doi.org/10.5281/zenodo.4567540>).



## CHAPTER IV

# AN UNEXPLAINED TSUNAMI: WAS THERE MEGATHRUST SLIP DURING THE 2020 MW7.6 SAND POINT, ALASKA, EARTHQUAKE?

From Santallanes, S. R., Goldberg, D. G., Koch, P. K., Melgar, D., Yeck, W. L., Crowell, B. W., & Lin, J. T. In review. An unexplained tsunami: Was there megathrust slip during the 2020 Mw7.6 Sand Point, Alaska, earthquake?. *Seismica*.

## 4.1 Introduction

Tsunamis are most often the result of earthquake sources at subduction zones. Megathrust slip is a key process for tsunamigenesis as it can produce large enough vertical motion to result in hazardous waves. The Shumagin segment of the Alaskan Subduction Zone (Figure 22) has been characterized as an area largely devoid of great earthquakes ( $M_w \geq 8.0$ ) for at least the past 100 years (Davies, Sykes, House, & Jacob, 1981). This may be due to the location being in transition between the fully creeping Sanak segment to the west and the fully locked Semedi segment to the east (Li & Freymueller, 2018). The Shumagin segment's seismic history is in stark contrast to its neighboring segments; great earthquakes have been observed in the Sanak segment (1946 Mw8.6) and the Semedi segment (1938 Mw8.3) in the past century, each producing large, devastating tsunamis (Davies et al., 1981; Witter et al., 2014; Li and Freymueller, 2018)(Davies et al., 1981; Li & Freymueller, 2018; Witter et al., 2014). Meanwhile, the last suspected great earthquake in the Shumagin segment is commonly thought to have occurred in 1788; however, geologic observations are more consistent with two earthquakes between Mw7.7-8.1 occurring under a month apart (Witter et al., 2014).

The October 19, 2020, Mw7.6 Sand Point earthquake was the second of three large earthquakes to affect the Alaskan peninsula over a 12-month period. First, the July 22, 2020, Mw7.8 ( $M_o = 6.91 \times 10^{20}$  N-m) Simeonof earthquake occurred on the megathrust near Simeonof Island (Figure 22, Crowell & Melgar, 2020). It produced a small tsunami with  $\sim 30$  cm maximum amplitude (relative

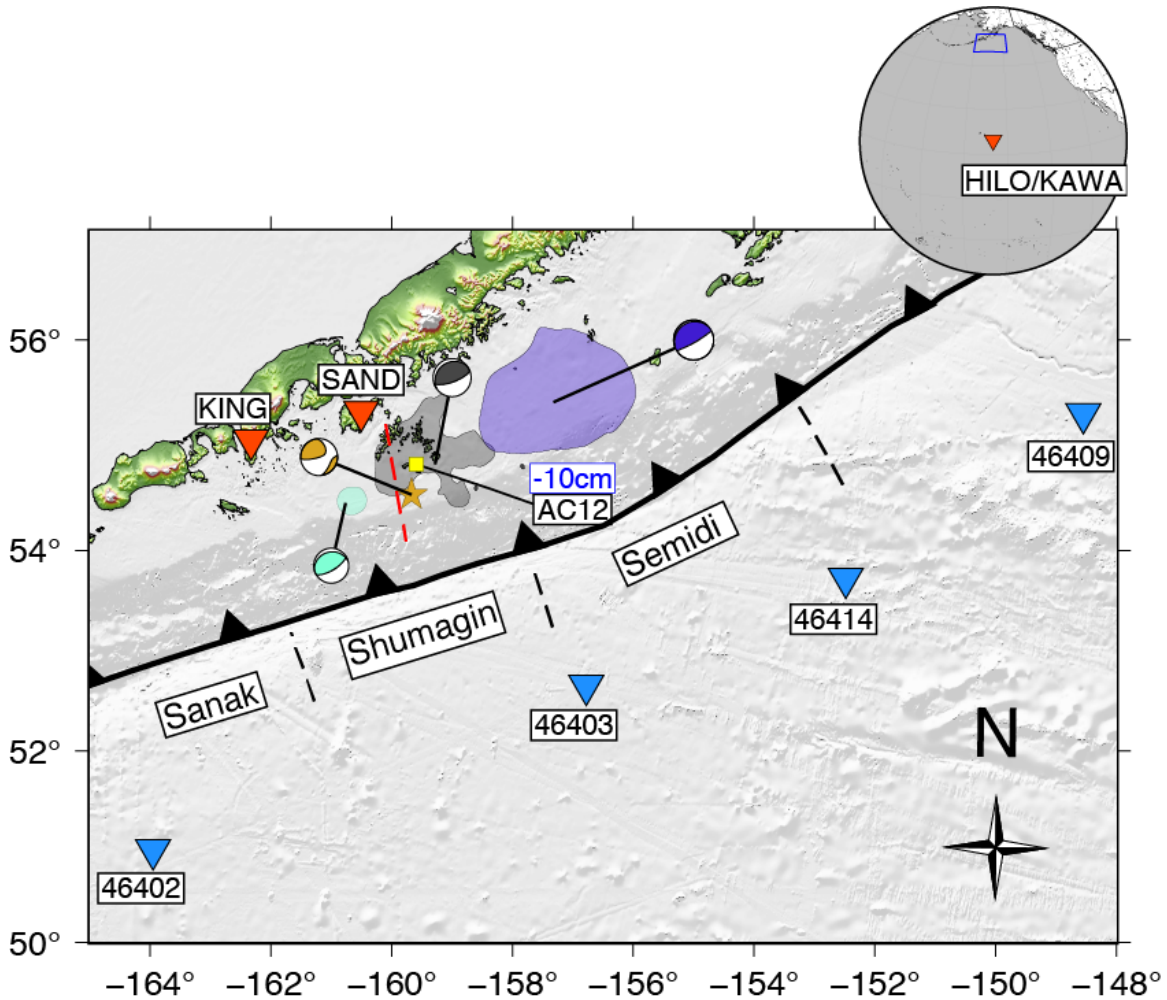


Figure 22. The study area, offshore of the Alaskan peninsula. Demarcations for the Sanak, Shumagin, and Semidi segments from Liu et al. (2020) are shown with dashed black lines. The 2020 Simeonof rupture zone is shown in black (Crowell & Melgar, 2020), the 2021 Chignik rupture zone is shown in dark blue (USGS Earthquake Hazards Program, 2017), and the July 2023 Sand Point rupture zone is shown in aquamarine. The W-phase centroid moment tensors (WCMT) for Simeonof, Chignik, and July 2023 Sand Point are shown in the same colors as their rupture zones. The surface projection of the USGS-NEIC finite fault plane for the 2020 Sand Point earthquake is delineated by a dashed red line. The epicenter and WCMT for the 2020 Sand Point earthquake are shown in gold. The King Cove (KING) and Sand Point (SAND) coastal sea level stations are shown as red triangles. DART stations are shown as light blue triangles. GNSS station AC12 (yellow square) is shown to have undergone 10 cm of subsidence during the 2020 Sand Point earthquake. The inset shows the locations of the coastal sea level stations in Hawai'i and the outline of the main study area in blue.

to typical sea level) at the nearby Sand Point, Alaska, coastal sea level station (Larson et al., 2021; Liu, Lay, & Xiong, 2022) and was barely measurable (<1 cm amplitude) at the Deep-ocean Assessment and Reporting of Tsunamis (DART) stations in the surrounding area.

In stark contrast, the October 19, 2020, Mw7.6 ( $M_o = 2.82 \times 10^{20}$  N-m) Sand Point earthquake produced a tsunami with maximum amplitude of 76 cm at the same Sand Point coastal sea level station and a  $\sim 30$  cm maximum amplitude at the Hilo, Hawai'i, coastal sea level station more than 3800 km away. The Sand Point tsunami was also recorded clearly by four DART stations (1-4 cm amplitudes; Figure 23d). The causative fault plane of this earthquake, based on the United States Geological Survey (USGS) National Earthquake Information Center (NEIC) W-Phase centroid moment tensor (WCMT), was a north-striking, 49 east-dipping, right-lateral, strike-slip fault with a 71% double-couple component (Figure 22). Strike-slip earthquakes typically do not produce large enough vertical deformation to generate tsunamis with amplitudes  $>30$  cm in the near- or far-field. It is therefore enigmatic that the Sand Point event produced a significantly larger local and trans-oceanic tsunami than the Simeonof event, given that (1) it is  $\sim 2.5$  times smaller by scalar moment, and (2) it has a strike-slip, rather than dip-slip, mechanism.

The peculiar nature of the Sand Point earthquake's tsunami was highlighted again by the July 29, 2021, Mw8.2 ( $M_o = 2.36 \times 10^{21}$  N-m) Chignik, Alaska, earthquake. The Chignik earthquake was a low angle thrust event and produced

a similar trans-oceanic tsunami to the Sand Point earthquake, despite its larger magnitude and rupture area (Liu et al., 2022). Comparison to the tsunamis generated by these larger magnitude megathrust events suggest that there must be additional factors contributing to the Sand Point earthquake’s tsunami generation.

## 4.2 The incompatibility of a strike-slip source

### 4.2.1 USGS model.

To test the hypothesis that strike-slip activation alone is insufficient to generate the observed Sand Point tsunami, we model the vertical seafloor deformation implied by the USGS finite fault model (model U0, Table 1) using the Okada model (Okada, 1985) and forward model the resulting tsunami waves using GeoClaw (LeVeque, George, & Berger, 2011). GeoClaw solves the non-linear shallow-water equations using adaptive mesh refinement so that areas of high tsunami complexity, such as the coastal sea level station locations, can be refined to higher discretization. We use the Shuttle Radar Topography Mission 15 (450 m pixels) for the model domain (Figure 22) (Tozer et al., 2019). We also use  $\frac{1}{13}$  arcsec ( $\sim 10$  m pixels) bathymetry/topography to provide greater detail for the areas around the coastal sea level stations. The tsunami simulations are run at 4 levels of mesh refinement starting at 5 arcmin ( $\sim 7.5$  km) and ending at 3 arcsecs ( $\sim 90$  m). We choose to use GeoClaw’s kinematic rupture feature for all models for faithful comparisons amongst them.

We prescribe Gaussian-shaped sea surface deformation unit source areas in a 2-dimensional grid with 10 km spacing across the region of interest; 428 sources

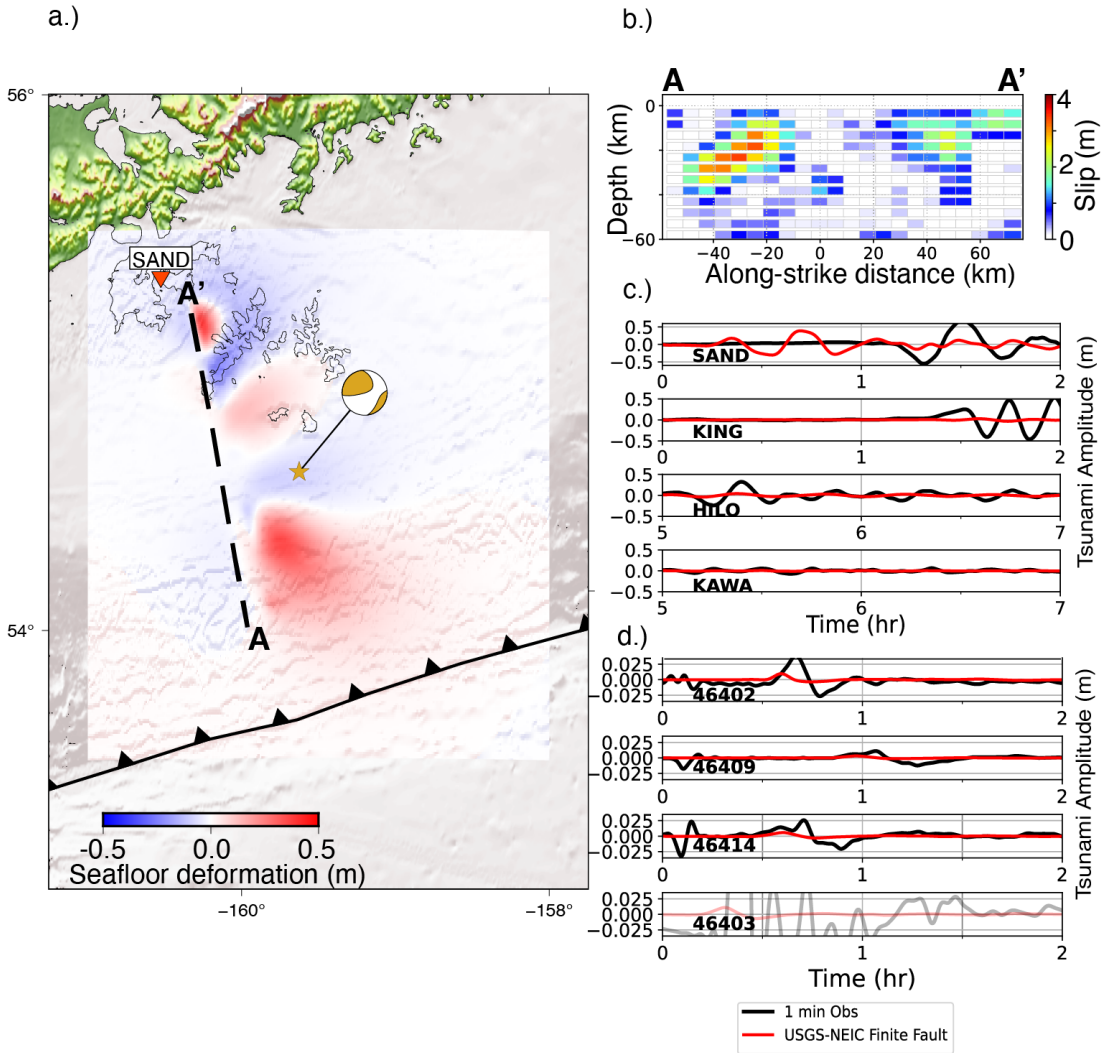


Figure 23. a.) Map showing the vertical deformation resulting from the USGS-NEIC finite fault model (model U0). The dashed black line from A-A' is the surface projection of the causative fault plane, as inferred by the USGS-NEIC. The hypocenter (star) and WCMT are shown in gold. b.) USGS-NEIC finite fault solution. c.) the observed (black) and modeled (red) tsunami waveforms at coastal sea level stations. d.) the observed (black) and modeled (red) tsunami waveforms at DART stations. DART 46403 is shown with slightly muted colors to indicate that it was impacted by Rayleigh wave contamination.

Model Name	Segments	Data Types	Allowable Rise Times	RMSE(s) [cm]
USGS-NEIC	SS	Teleseismic	–	9.0*
Static (S1)	SS	DART, CSLS, SGNSS	N/A	S1a:3.8* S1b:4.7*
Hydrodynamic (H0)	N/A	DART, CSLS	N/A	3.0*
Static (S2)	SS,MT	DART, CSLS, SGNSS	N/A	S2a: 82.3† S2b: 77.8†
Kinematic (K1)	SS, MT	DART	”Standard” (0-30 s)	4.0*
Kinematic (K2)	SS, MT	DART, SGNSS, HRGNSS, Teleseismic, STR	”Long” (0-60 s)	4.1*
Kinematic (K3)	SS, MT	DART, SGNSS, HRGNSS, Teleseismic, STR	MT: ”Very Long” (0-120 s) SS: ”Standard” (0-30 s)	4.2*

Table 1. The attributes of the inversions considered in this study. SS is strike-slip, MT is megathrust, CSLS is coastal sea level station, SGNSS is static GNSS, HRGNSS is high-rate GNSS, STR is strong motion accelerometer. \* denotes unweighted RMSE and †denotes weighted RMSE.

in total (Figure S1). These unit source areas have an amplitude of 1 m and a standard deviation of 5 km. The Gaussian nature of the tsunami source elements ensures that they overlap at the margins, such that smooth variations of sea surface displacements can be expressed with a sum of these discrete sources. Each tsunami source element is run independently in GeoClaw to compute the Green's function from each source to each of eight observing stations: two near-field coastal sea level stations on the Aleutian Islands (Sand Point and King Cove), two far-field coastal sea level stations on the island of Hawai'i (Hilo and Kawaehai), and four DART stations (Figure 22) (Titov et al., 2005).

The vertical seafloor deformation pattern derived from the USGS strike-slip model has a peak subsidence of 0.2 m and a peak uplift of 0.4 m (Figure 23a), which is insufficient to produce the observed tsunami amplitudes (Figure 23c, d). The unweighted root mean squared error (RMSE) of the tsunami waveforms is 9.0 cm. Not only is the modeled amplitude at the Sand Point coastal sea level station much smaller than the recorded amplitude (0.4 m versus 1.3 m trough to crest), the forward-modeled tsunami also arrives  $\sim 1$  hour earlier than the observed tsunami. While timing discrepancies are expected at far-field sites due to unmodeled effects of the compressional seafloor (Tsai, Ampuero, Kanamori, & Stevenson, 2013), the large timing discrepancy at the near-field Sand Point site suggests that this strike-slip model does not accurately represent the tsunamigenic deformation.

The USGS model itself has unphysical qualities that suggest it is a poor representation of the true earthquake source. The published model on the USGS

Event page is accompanied by text that reads, “[w]e note that the depth to the top of the slab at the location of the epicenter is about 26 km, yet our model strongly prefers slip at shallower depths. Rupture extending through the top of the slab is non-physical and is likely indicative of some greater rupture complexity (e.g., multi-fault rupture) not considered in this model.” In addition, this model includes only teleseismic broadband observations, and does not directly consider the tsunami signal. It is therefore unsurprising that the USGS model is incompatible with the tsunami observations.

#### **4.2.2 Joint model of on-shore and off-shore observations.**

To that end, we perform an additional slip inversion on the strike-slip fault orientation using observations of both the earthquake and the tsunami: DART, near-field coastal sea level, and 11 onshore static Global Navigation Satellite System (GNSS) observations estimated by Central Washington University (Herring et al., 2016). We de-tide the coastal sea level observations and model synthetics with a bandpass filter from 2 min to 120 min. We apply a simple cross-correlation time shift to the synthetic data at the Hawai’i coastal sea level stations to correct the far-field travel time error introduced by unmodeled effects from a compressible seafloor (Tsai et al., 2013). Tsunami propagation in shallow water is non-linear, so only the first  $\sim 1$ -1.5 wavelengths can be reliably considered; the non-linearity makes later arrivals too difficult to account for in linear inversions (Melgar & Bock, 2013; Yue et al., 2015). DART station observations are typically sampled at 15 min intervals; however, the earthquake signal caused these stations to switch into

“event mode”, meaning they are temporarily sampled between 15 sec and 1 min. We de-tide the DART observations and model synthetics with a bandpass filter from 5 min to 120 min. DART station data are recorded by a bottom pressure recorder. Seismic arrivals, such as Rayleigh waves and acoustic phases, introduce pressure signals that are separate from tsunami energy. As a result, it is important to mask out these earthquake signals and use only the portions of the waveform that reflect the tsunami itself. At DART station 46403 (Figure 22), the tsunami’s arrival overlapped with seismic/acoustic signals and therefore that station could not be used in this study’s inversions. Regardless, the forward models in this study estimate the tsunami signal at all four DART station locations. We down-weight the King Cove coastal sea level station and DART station 46402 relative to the remaining sites because those observations appear to include an additional non-tectonic source (discussed in Section 5).

We use the MudPy slip inversion code (Melgar & Bock, 2013), regularized using a zeroth order Tikhonov approach and selecting the optimal regularization parameter from the L-curve criterion. The weighting scheme for the geodetic and coastal sea level data follows (Melgar, LeVeque, Dreger, & Allen, 2016), allotting importance only to the linear portion of the waveform data. DART station and static GNSS data were weighted 10 times higher than the coastal sea level station data. We use the 1-dimensional crustal velocity model (Pasyanos, Masters, Laske, & Ma, 2014) to calculate the static Green’s functions for the GNSS stations.

Initially, we constrain the model to the USGS magnitude (model S1a, Figure 24a,

Table 1), resulting in tsunami waveform fits with an average unweighted RMSE of 3.8 cm (Table 1). Next, we relax the moment constraint to test whether a larger magnitude strike-slip event can account for the observed tsunami signals (model S1b, Figure 24b, Table 1). Model S1b prefers an Mw8.0 source yet results in degradation of the tsunami waveform fits (Figure 24c) with an unweighted RMSE of 4.7 cm. These results bolster the interpretation that a single, planar strike-slip fault with the geometry of the USGS WCMT cannot be the sole source of the observed tsunami.

### **4.3 Deformation requirements of the observed tsunami**

Given that the WCMT strike-slip geometry cannot generate the observed tsunami, we use coastal sea level and DART data to invert directly for the sea floor deformation required to produce the observed tsunami signals, independent of a slip distribution. We refer to this hydrodynamic model as model H0 (Table 1). This approach is useful because it requires few assumptions and directly solves for the required hydrodynamic initial condition, the seafloor deformation (Lin, Aslam, Thomas, & Melgar, 2020; Tsushima et al., 2009). The inversion does not consider the geophysical process responsible for the modeled deformation (e.g., fault geometry, multi-fault ruptures, or non-seismic sources such as landslides). We invert sea level data from the three DART stations and the two near-field coastal sea level stations. Figure 25 shows the time intervals of the sea-level data used in the inversion as shaded gray regions. We regularize the inversion with a Tikhonov operator of zeroth order and then employ an L-curve criterion from the inversions

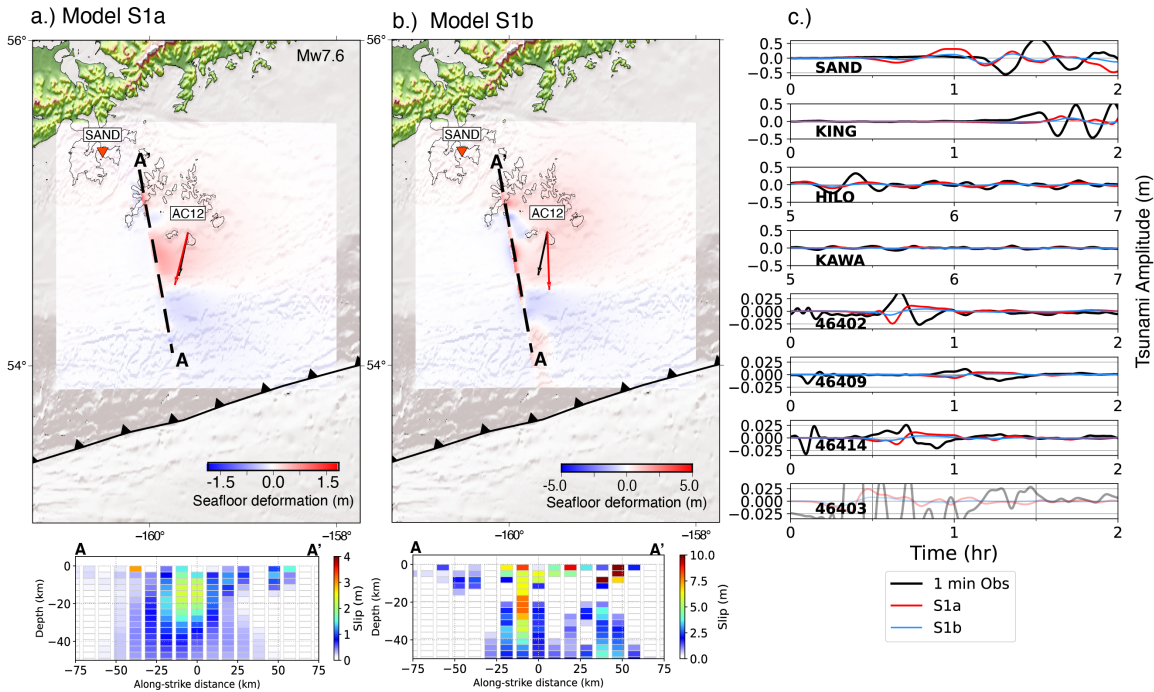


*Figure 24.* The results for model S1. a.) Map of study area showing seafloor deformation implied by model S1a constrained to USGS-NEIC magnitude. Line A-A' shows the surface projection of the strike-slip geometry, with cross section A-A' below showing the modeled slip distribution along the strike-slip geometry. Model S1a is constrained to a magnitude of Mw 7.6. b.) Map of study area showing seafloor deformation implied by model S1b without any magnitude constraint, resulting in slip distribution equivalent to Mw 8.0. Line A-A' shows the surface projection of the strike-slip geometry, with cross section A-A' below showing the modeled slip distribution along the strike-slip geometry. c.) Observed tsunami waveforms (black) with resulting synthetic waveforms from models in (a.) and (b.) shown in red and blue, respectively.

to find the optimal trade-off between smoothing and misfit (Figure S2) (Aster, Borchers, & Thurber, 2018).

We note an interesting feature of the DART data included in this inversion. Sea level data in the deep ocean from a megathrust rupture can usually be modeled as a solitary gaussian lump; DART station 46402 exemplifies this typical character (Figure 25c). However, the sea level records at DARTs 46414 and 46409 are more complex. These stations contain what appears to be two partially overlapping gaussian signals; the first requiring a smaller-amplitude source and the second requiring a larger source arriving after the first, suggesting kinematic complexity of the tsunami source (Figure 25c). The hydrodynamic solution clarifies that the vertical seafloor deformation necessary to produce the sea level observations is larger than the USGS model produces (1.4 m versus 0.4 m maximum displacement for models H0 and U0, respectively; Figures 4 and 2). The tsunami waveform fits have an unweighted RMSE of 3.0 cm for the H0 model, one-third the value for model U0. Importantly, using model H0 as the initial condition in a fully non-hydrostatic trans-oceanic tsunami forward model produces good fits to the far-field tsunami waveforms at Hilo and Kawaehai, Hawai'i (Figure 25b), observations that were not used in the inversion itself. Critically, the primary seafloor deformation signal resulting from model H0 is trench-parallel (Figure 25a), which is inconsistent with the expected pattern for a trench-perpendicular strike-slip fault. This pattern does not definitively rule out strike-slip faulting altogether but suggests that deformation from the strike-slip geometry is not the dominant signal for tsunami

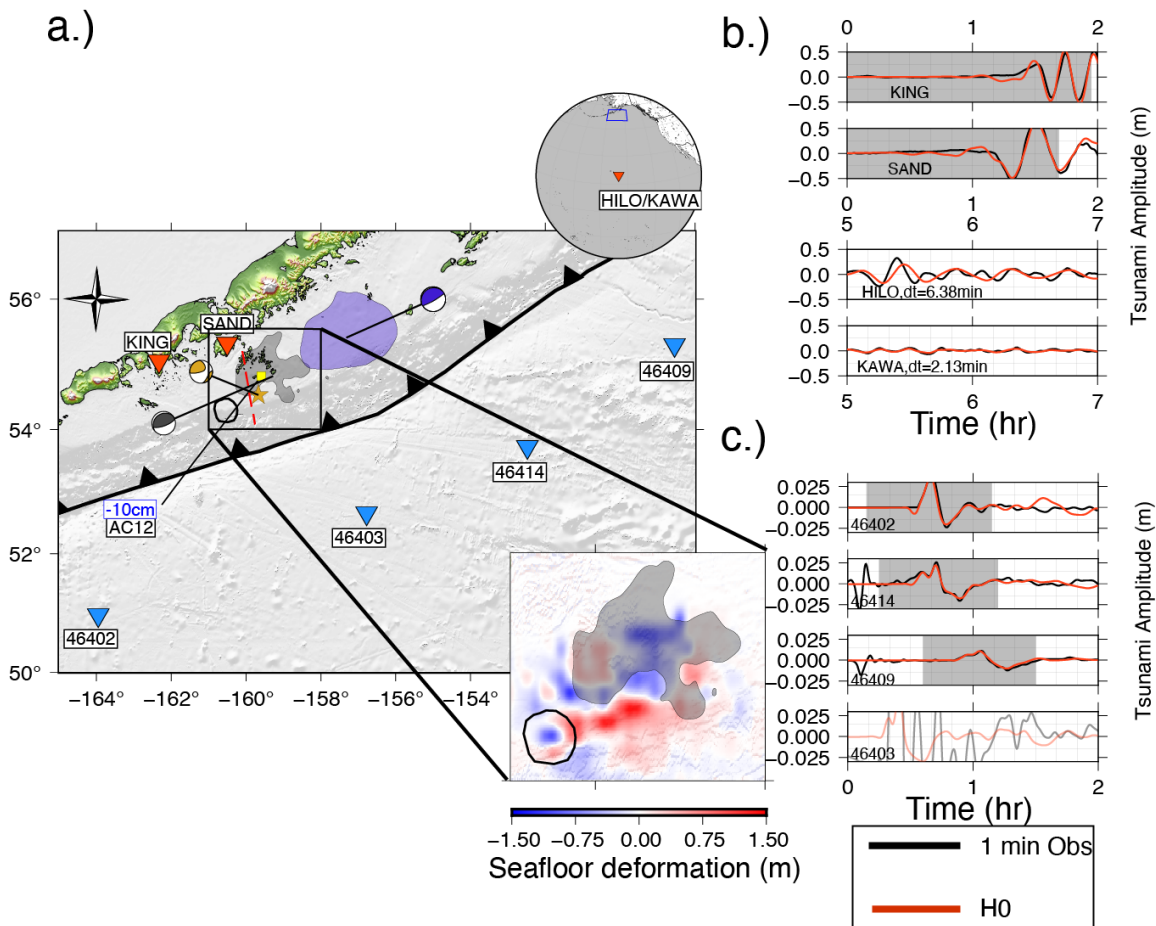


Figure 25. The hydrodynamic model (model H0) results. a.) Region map with the 2020 Simeonof and 2021 Chignik rupture zones and associated WCMTs shown in black and blue, respectively (Crowell & Melgar, 2020; U. S. Geological Survey, 2017). The surface projection of the USGS-NEIC finite fault plane for the 2020 Sand Point earthquake is delineated by a dashed red line. The epicenter and WCMT for the 2020 Sand Point earthquake are shown in gold. The King cove (KING) and Sand Point (SAND) sea level stations are shown as red triangles. DART stations are shown as light blue triangles. GNSS station AC12 location shown by yellow square. The red dashed line shows the surface trace for the W-Phase nodal plane used in the USGS-NEIC finite fault model. The top inset shows the locations of the coastal sea level stations in Hawai'i and the outline of the main study area in blue. The bottom inset shows the modeled seafloor deformation (model H0). The black outline denotes an area where a suspected submarine landslide may have occurred, based on the classic dipole sea surface deformation pattern. b.) The tsunami waveforms (observations in black, model synthetics in red) from the coastal sea level stations. Modeled waveforms for Hilo and Kawaehai (KAWA) are shifted by 6.38 min and 2.13 min, respectively, for temporal consistency with the observed data. c.) The tsunami waveforms (observations in black, model synthetics in red) from the DART stations. Gray boxes in a.) and b.) outline the portions of the coastal sea level and DART observations used in the tsunami inversion.

generation. Checkerboard tests of the hydrodynamic inversion reveal that the resolution is low across the inversion area, so some smearing of the main inversion features is to be expected, especially in the regions of smaller signals (Figure S3). Finally, we find that the trench-parallel deformation is well constrained by the Simeonof rupture zone (Figure 25a inset).

We note that model H0 has an apparent secondary signal that is neither trench-parallel nor trench-perpendicular. The signal area is dominated by a zone of subsidence to the north, with a concentrated area of uplift immediately to its south (Figure 25a inset, outlined in black). This positive-negative dipole pattern is reminiscent of a submarine landslide signal. The area is located on the steep part of the shelf-break and occurs somewhere within an area  $\sim 1300$  km<sup>2</sup>, however since the model resolution is low, this feature may be smeared, and the true size may be smaller. This apparent landslide signal is discussed in more detail in section 5.

#### **4.4 Allowing coeval megathrust and strike slip rupture**

##### **4.4.1 Megathrust rupture initiation.**

Next, we consider the relative timing of rupture on this strike slip and megathrust fault orientation. Megathrust rupture may have initiated coincident with strike slip rupture or may have been initiated by dynamic triggering from the strike-slip rupture. We consider DART, coastal sea level, and static GNSS sites to compute a suite of slip models testing potential locations for megathrust initiation. The data weights are the same as in model S1, wherein DART station and static GNSS data were weighted 10 times higher than the coastal sea level station data.

Our first model assumes megathrust initiation coincident with the NEIC event hypocenter (model S2a, nucleation point N0 in Figure 26a). Nine additional models consider a grid of potential megathrust nucleation points surrounding the hypocenter (models S2b): three nucleation points are to the west of the strike-slip fault where the megathrust is thought to be creeping (Li & Freymueller, 2018) three are along the intersection with the strike-slip fault, and three are to the east, within and up-dip of the 2020 Simeonof earthquake rupture zone (Crowell & Melgar, 2020) and in proximity to the contact of the 2020 Simeonof and 2021 Chignik rupture zones (Figure 26). We assume that dynamic triggering of the megathrust would take place when an S-wave front traveling from the hypocenter at 3.0 km/s reaches the nucleation site. We do not model the full rupture kinematics, rather we assume a constant rupture velocity from the nucleation point across the megathrust, such that slip on each subfault occurs instantaneously upon the passing of the rupture front. This assumption is valid because of the slow tsunami propagation speeds relative to earthquake slip durations (e.g., A. Williamson, Melgar, & Rim, 2019).

Low megathrust rupture propagation speeds are consistent with observations of “tsunami earthquakes”, those seismic sources that produce larger amplitude tsunamis than expected for their magnitude. Slow rupture propagation may also explain a dearth of high-frequency ( $\sim 1$  Hz) energy related to the megathrust, and therefore, difficulty in observing the source with typical seismic monitoring tools. To that end, we consider megathrust rupture speeds between 0.50 and 1.25 km/s.

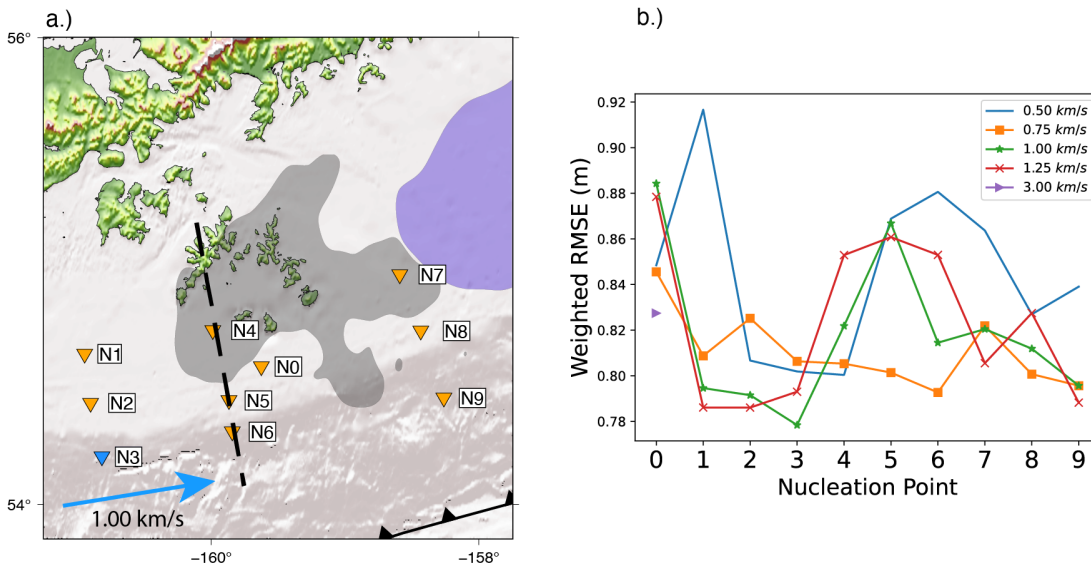


Figure 26. Potential megathrust rupture nucleation points. a.) Map view of potential nucleation points (orange triangles), including event hypocenter (N0) and nine additional potential nucleation points (N1-N9). Preferred nucleation point, N3, is shown in blue along with the direction and best fitting speed of propagation, 1 km/s. The 2020 Simeonof and 2021 Chignik rupture zones are shown in black and blue, respectively (Crowell & Melgar, 2020; U. S. Geological Survey, 2017) b.) The weighted RMSE for static triggering at nucleation point N0 compared to RMSEs of nucleation points N1-N9 for four different rupture velocities.

We assume the strike-slip plane ruptures at more traditional speeds, allowing a maximum rupture velocity of 3 km/s.

We calculate the weighted RMSE for each combination of nucleation point and rupture velocity to determine the most likely scenario. Instantaneous, coincident rupture of both the strike-slip and megathrust geometries (model S2a) results in a weighted RMSE of 82.3 cm (Figure 26b). The minimum weighted RMSE (77.8 cm) occurs for the scenario of megathrust rupture initiation at a location 79 km southwest of the event hypocenter and propagating at 1 km/s toward the northeast of the proposed rupture domain (location N3, Figure 26). These results show that the observations are best explained by delayed initiation (dynamic triggering) of the megathrust, rather than coincident rupture of the strike-slip and megathrust geometries (Figures 26 and 27).

#### **4.4.2 Full Kinematic Rupture Modeling.**

We have demonstrated that the tsunami observations can allow for slip on both a strike-slip fault and the subduction interface. On its face, however, megathrust rupture seems incongruous with the WCMT produced by the NEIC that prefers a strike-slip rupture. The WCMT is calculated to idealize the earthquake as a point source and is therefore insensitive to complex slip, including multiple causative faults. Ultimately, the sum of slip contributed from any combination of faults must be consistent with the overall observed WCMT. Following the Monte Carlo approach of Yeck, Shelly, Materna, Goldberg, and Earle (2023), we determine that there is a right-lateral strike-slip fault geometry, that

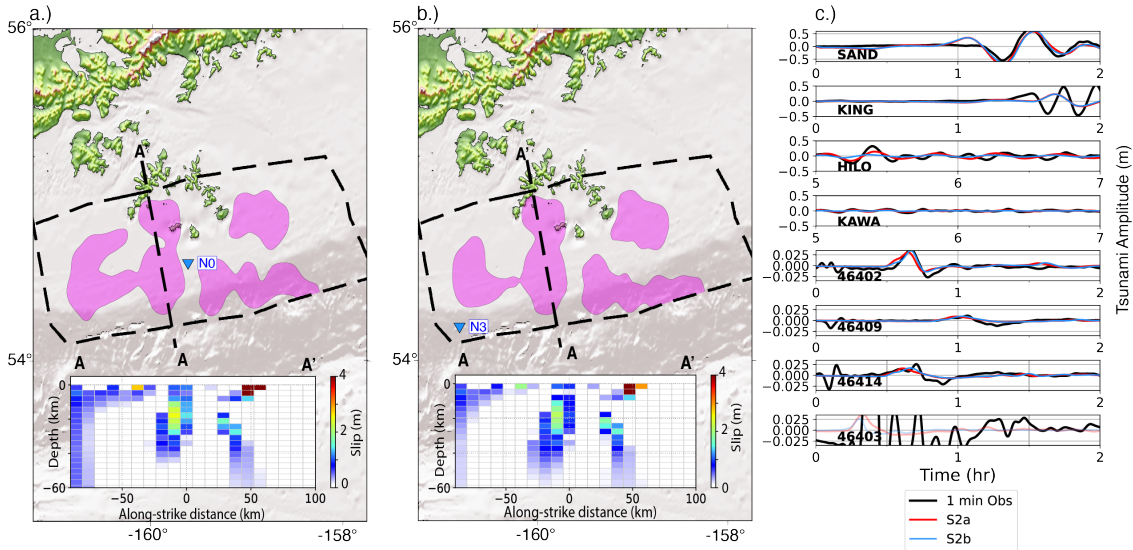


Figure 27. Model S2 results. a.) Results of model S2a. Dashed black line delineates the portion of the megathrust considered in the inversion. Magenta contour and shaded area shows the  $>1$  m rupture patch of the inversion rupture zone. Dashed line A-A' shows the surface projection of the strike-slip plane, with slip distribution on the strike-slip plane shown below. The maximum allowable rupture speed is 1.25 km/s for the megathrust and 3.00 km/s for the strike-slip plane. b.) Results of preferred model S2b (nucleation point N3 with maximum allowable rupture velocity of 1 km/s). Dashed black line delineates the subfaults of the megathrust allowed to partake in the inversion. Magenta contour and shaded area shows the  $>1$  m rupture patch of the inversion rupture zone. Nucleation point 3 is shown as a blue inverted triangle. A-A' is the surface projection of the strike-slip plane from the USGS-NEIC WCMT. c.) The observed tsunami waveforms (black) compared to the modeled tsunami waveforms from models S2a and S2b in red and blue, respectively.

when combined with the megathrust geometry (strike/dip/rake: 245/20/90 from Hayes et al. (2018)) of similar seismic moment, is consistent with the WCMT. The necessary right-lateral strike-slip geometry is similar in strike ( $\sim 350$ ), but much steeper in dip ( $\sim 85$ ) than the originally inferred strike-slip geometry (Figure S4). We note a caveat of this analysis: because we infer slow rupture speeds on the megathrust (Figure 26b), a typical WCMT solution may not equally sample the contributions from both geometries. Therefore, we interpret this analysis simply as evidence that the true strike-slip orientation may be steeper-dipping, but do not hold ourselves to an exact strike and dip. Some trial and error is used to find a model that is reasonably consistent with the overall WCMT.

We explore the earthquake source that best describes all available observations (teleseismic, near-field seismic and geodetic), while allowing slip on the megathrust and steeply-dipping strike-slip plane (Figure S4). We use the Wavelet and simulated Annealing Slip (WASP) software package (see Data and Code Availability), a nonlinear simulated annealing method to model slip amplitude, rake, rupture time, and rise time in the wavelet domain (Goldberg, Koch, Melgar, Riquelme, & Yeck, 2022; Ji, Wald, & Helmberger, 2002; Koch, Bravo, Riquelme, & Crempien, 2019). The two planes are divided into 10 km x 10 km subfaults. The strike-slip geometry is comprised of 15 subfaults in the along-strike direction and 7 in the down-dip direction for a total of 105 subfaults. The megathrust geometry contains 20 subfaults in the along-strike direction and 15 in the down-dip direction for a total of 300 subfaults. These kinematic models (referred to as K1-3) follow

Model Name	Composite Moment Tensor			Kagan Angle	USGS MT
	Strike-Slip Mw7.6	Megathrust Mw7.5	Total MT Mw7.7		
K1			=	13.03°	
K2			=	18.85°	
K3			=	31.70°	

*Figure 28.* The associated moment tensors (MTs) for the strike-slip segment and megathrust segment for the four kinematic inversions and their composite MTs. The Kagan angle between each composite MT and the USGS-NEIC WCMT are given for each inversion model. The USGS-NEIC MT is shown for visual comparison.

the results of the S2 models by prescribing delayed rupture initiation at point N3 on the megathrust orientation (Figure 26). We calculate the Kagan angle to compare the similarity between the model moment tensor and the WCMT; a lower the Kagan angle implies better agreement with the moment tensor double-couple component (Figure 28 and D’Amico et al., 2011). WASP was designed to jointly invert data from a variety of earthquake-observing instruments, including broadband teleseismic, regional strong-motion accelerometer, GNSS, and/or interferometric synthetic aperture radar observations (Goldberg et al., 2022). For application to the Sand Point event, we extend the software’s capability

to allow for DART sea level observations by transforming the sea level Green’s functions calculated in GeoClaw to the frequency domain (see section 2). Models K1-3 consider both near-field and teleseismic observations of the earthquake, in addition to the DART tsunami observations. The earthquake observations include 42 teleseismic P waves, 16 teleseismic SH waves, and 53 long-period surface waves (15 Love waves and 38 Rayleigh waves), as well as regional data from 6 strong-motion accelerometers, 13 high-rate GNSS stations, and 11 static GNSS stations. The high-rate GNSS data was processed with GipsyX (Bertiger et al., 2020). The teleseismic broadband and near-field accelerometer data processing are described in Goldberg et al. (2022) and Koch et al. (2019). Teleseismic observations are considered such that P-waves receive half the weight of surface waves, and SH-waves receive half the weight of P-waves (e.g., Goldberg et al., 2022).

The K models have progressively longer allowable rise times (Table 1), as K1 and K2 kept selecting the longest allowable for their permitted ranges along the subduction zone interface. Results for K1 and K2 are viewable in Text S1. We focus on results from model K3, which we suggest has the most appropriate allowable rise times with “standard” rise times (up to 30 s) along the strike-slip geometry and “very long” rise times (up to 120 s) along the megathrust. The resulting model prefers slip equivalent to an Mw7.6 rupture occurring on the strike-slip geometry with a rupture duration of  $\sim 40$  s (Figure 29). The megathrust takes much longer to rupture,  $\sim 300$  s for a major portion of the subduction interface. The total slip on the megathrust is equivalent to an Mw7.8 rupture with peak slip

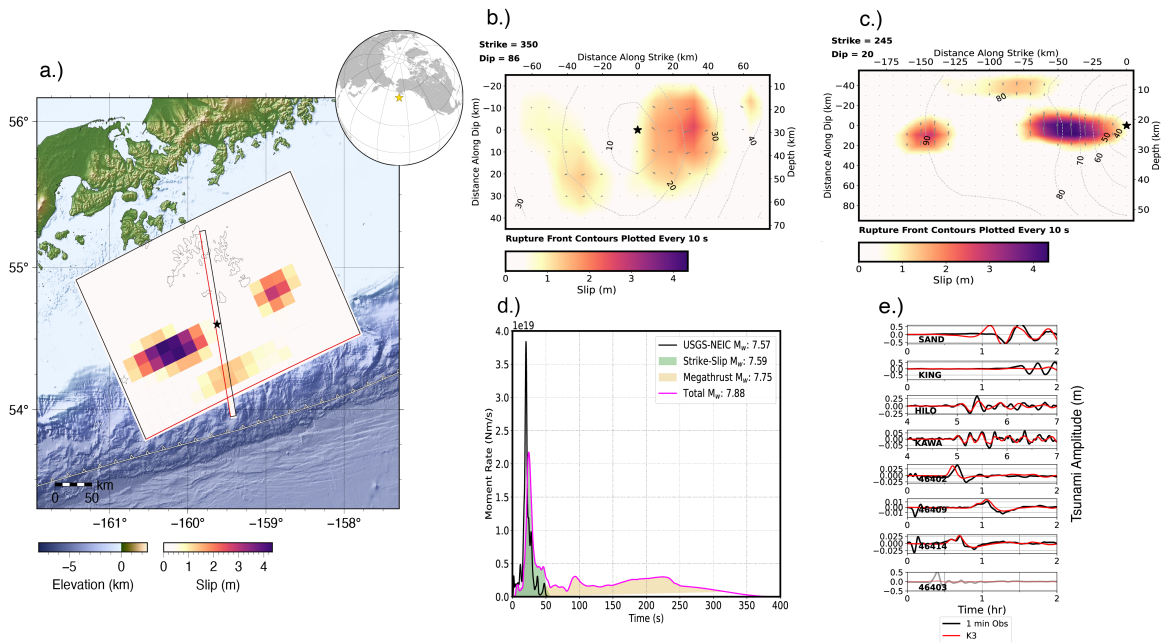


Figure 29. Model K3 results. a.) Map showing the geographical distribution of slip along the megathrust as well as the strike-slip geometry used in inversion K3. Black star show the hypocenter for the strike-slip and a blue star shows the nucleation point for the megathrust. Red lines indicate the updip edge of the two fault orientations. b.) Smoothed slip distribution and rupture time contours for the strike-slip segment. Small gray arrows indicate rake direction, scaled by amplitude of slip. Black star shows the hypocentral location. c.) Same as b.) but for the megathrust segment. Note that the rupture time contours start 29.5 s later, as we assume delayed slip to nucleation point N3. d.) The source time function for the published USGS-NEIC finite fault product (black; USGS Earthquake Hazards Program, 2017), the strike-slip segment of model K3 (green), the megathrust portion of model K3 (yellow), and the total source time function of model K3 (magenta) e.) Observed (black) and model K3 synthetic (red) tsunami waveforms.

of 4.5 m. The total resulting magnitude of both the strike-slip and megathrust orientations is Mw7.9.

The synthetic fit quality of the teleseismic arrivals is consistent with the weighting scheme applied, with surface waves being best fit and SH-waves being poorly fit. Synthetic P-waves for stations between  $0^\circ$  and  $40^\circ$  azimuth are low in amplitude compared to the observed waveforms (Figure S5). First arrivals improve considerably between azimuths of  $60^\circ$  and  $110^\circ$  but degrade again beyond that range. The synthetic Love and Rayleigh surface waves fit the shape and timing of the waveform packets yet are higher in amplitude than the observed waveforms (Figures S6 and S7). SH body waves fit the observed waveforms poorly, which is expected given their lower weights (Figure S8). High-rate GNSS waves for stations between azimuths  $330^\circ$  and  $25^\circ$  roughly follow the wave packet shape, yet they consistently underpredict the observed ground motion. Stations outside those azimuths are poorly fit (Figure S9). The strong motion synthetic fits to the observed data are fair (Figure S10). Model K3 fits the observations at DARTs 46409 and 46414 well (Figure 29e). However, the solitary gaussian lump at DART 46402 arrives 4 minutes early in model K3 compared to the observed data. The coastal sea level station fit for Sand Point is fair; the synthetic tsunami signal arrives 28 minutes early and with poor fit to the first arrival; however, later arrivals are more consistent with the observations. The observations at the King Cove, Alaska, site remain poorly fit, with the synthetic waveforms severely

underpredicting the observed sea level. The coastal sea level fits for the stations in Hawai'i are good, though slightly underestimated (Figure 29e).

## 4.5 Discussion

### 4.5.1 Hidden megathrust rupture.

The variety of inversions conducted in this study lead to an inescapable conclusion: it is infeasible that a strike-slip mechanism alone caused the tsunami observed following the 2020 Sand Point earthquake. Therefore, we posit that, in addition to strike-slip rupture, a slow rupture on the adjacent megathrust occurred as part of the earthquake. We recognize that this theory is somewhat at odds with teleseismic source characterization carried out shortly after the event, such as that performed by the USGS NEIC; it would require a large amount of slip to go undetected by traditional rapid characterization techniques. While we cannot fully account for how such a large quantity of slip could go undetected, we hypothesize that the slow megathrust slip radiates energy inefficiently at frequencies relevant to rapid response practices. It has been noted that near-trench “tsunami earthquakes” rupturing through the shallow, low rigidity portions of the megathrust can be depleted of both far-field (Newman, Hayes, Wei, & Convers, 2011) and near-field (Sahakian, Melgar, & Muzli, 2019) seismic radiation. A characteristic of these tsunami earthquakes is very slow rupture (e.g., Riquelme, Schwarze, Fuentes, & Campos, 2020). Our kinematic inversion results suggest that a slow rupture speed for the megathrust,  $\sim 1$  km/s, is preferred, however, regional ground motion intensities were not anomalously low for an Mw7.6, nor was far field radiated

energy. These seemingly conflicting observations may be explained by the strike-slip rupture (Mw7.6) radiating with the usual efficiency, and the megathrust rupture (Mw7.8) radiating inefficiently.

Explaining the larger seismic moment of model K3 compared to the moment of the USGS-NEIC solution (Mw7.9 vs. Mw7.6, respectively) is an outstanding challenge. However, we note that there is some precedent for a large-magnitude rupture evading traditional seismic response algorithms. A recent example of this is the 2021 Sandwich Islands sequence (Jia, Zhan, & Kanamori, 2022). That sequence consisted of multiple large, complex events occurring in close spatiotemporal proximity, which led to initial underestimation of the overall moment release, in which the USGS NEIC initially reported a Mw7.5 event, only to decipher the larger magnitude Mw8.1 mainshock, hidden in the coda of that first earthquake, the following day. While we have been unable to find similar evidence of a larger rupture hidden in the coda of the teleseismic data from the 2020 Sand Point event, the possibility remains that further scrutiny of the data may illuminate some previously undetected seismic signal.

Another tsunamigenic possibility is that rupture progresses at a more “traditional” speed and that tsunamigenesis occurs as a result of inelastic wedge deformation (Ma & Nie, 2019). This mechanism is feasible for Sand Point since most of the Shumagin segment is creeping in the interseismic period (Li, Wang, Wang, Jiang, & Dosso, 2018) and thus can reasonably be inferred to prefer rate-strengthening modes of rupture. Indeed, Crowell and Melgar (2020) imaged some

after-slip following the Simeonof earthquake. In this process, the rupture front propagates at a traditional speed, near shear-wave speeds, but very long rise times allow slip to accumulate slowly. These processes could ostensibly be enough to keep the true extent of the megathrust co-seismic slip "silent" in the seismic data.

#### **4.5.2 Potential Submarine Landslide.**

Finally, we note that none of the slip inversions considered in this work have been able to fit the tsunami waveforms at the King Cove coastal sea level station (Figures 2c, 3c, 6c, 8e). In addition, models K1-K3 had a notable timing misfit to DART station 46402 (e.g., Figure 29e, S11e, S18e). Recall that the hydrodynamic model (H0) showed evidence for a submarine landslide in the southwestern corner of the model space (Figure 25a), which we hypothesize may be necessary to improve fits to King Cove coastal sea level station and DART station 46402.

Submarine landslides produce a positive-negative dipole of seafloor deformation, wherein the negative portion (subsidence) corresponds to the area where mass is removed and the positive lobe corresponds to the area where the excavated mass moves downslope (e.g., A. L. Williamson, Melgar, Xu, & Milliner, 2020). The location of such a dipole signal is highlighted in Figure 25a. This area is on the steep section of the shelf-break and is within 20 km of the ALEUT-05 active source survey (Bécel et al., 2017). That study noted widespread evidence that this part of the continental slope is prone to submarine landslides. Thus, we posit that a submarine landslide could have contributed to the observed tsunami, particularly the signal observed at King Cove. However, we note that the occurrence of a

submarine landslide can only be confirmed by direct observation, for example by repeated multibeam bathymetry surveys.

We consider the cumulative effect of the kinematic earthquake slip model K3 with the submarine landslide signal observed in model H0 (Figure 30). We assume the submarine landslide occurs instantaneously, 180 s after earthquake origin, based on trial-and-error testing of landslide onset at various times after earthquake origin. While the fits to the King Cove waveform do improve with the addition of the landslide, the degradation of fits to 46402 shows the limitations of the assumption of an instantaneous landslide (Figure 30). In reality, landslides occur over many seconds — thought to be on the order of  $\sim 100$  s (Ten Brink, Geist, & Andrews, 2006). However, accounting for temporal evolution of the landslide is beyond our scope.

#### **4.5.3 Regional context and hazard considerations.**

The 2020 Sand Point earthquake shares some critical similarities with the 1946 Mw8.6 earthquake on the neighboring Sanak segment. The 1946 event was highly deficient in seismic radiation, with a teleseismic magnitude of only 7.4, indicating there may be some structural control on the megathrust that generates slow and long ruptures devoid of seismic radiation (López & Okal, 2006). Furthermore, López and Okal (2006) showed that the 1946 Sanak ruptured at a velocity of 1.12 km/s and required a submarine landslide to fit near-field tsunami data, mirroring what we propose here. Bécel et al. (2017) demonstrated that the Shumagin segment contains complex tsunamigenic structures and demonstrated

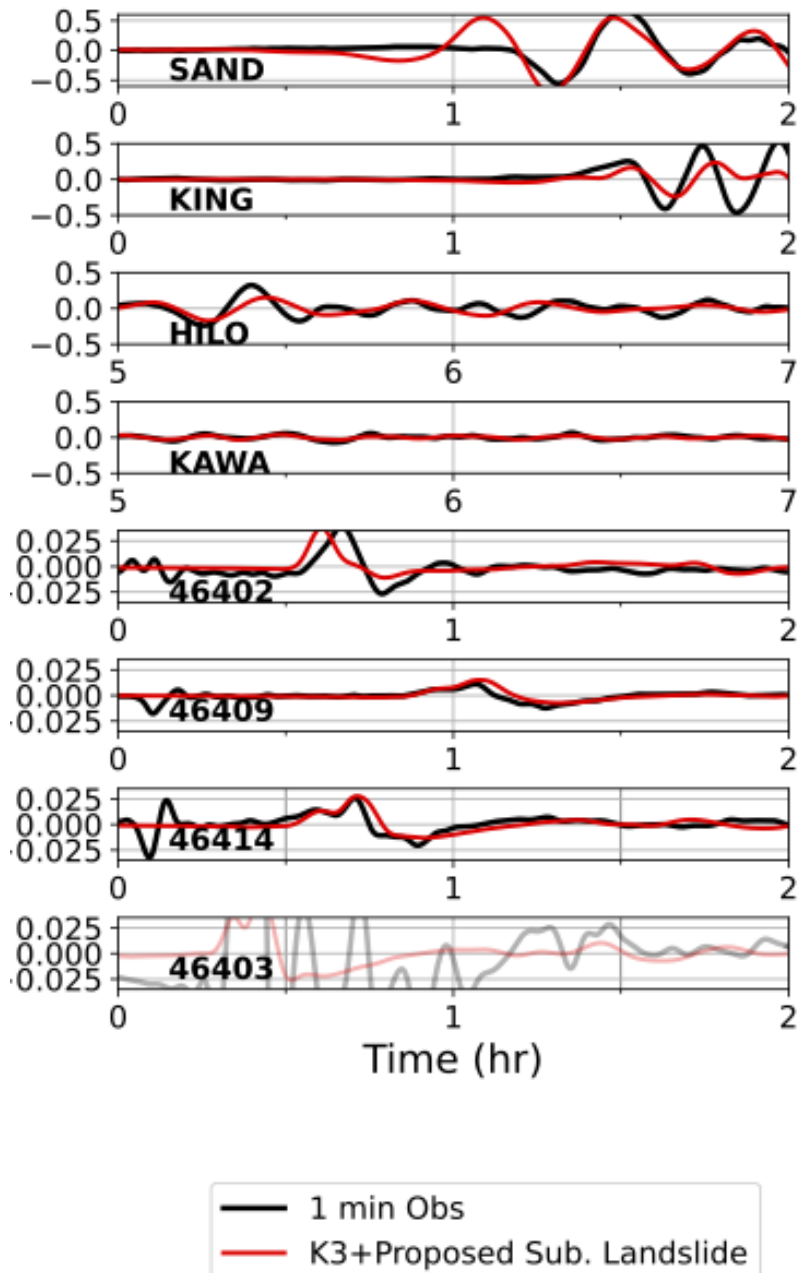


Figure 30. The observed tsunami waveforms (black) compared to synthetic tsunami waveforms (red) resulting from the combination of kinematic model K3 and a submarine landslide signal obtained from model H0.

that the small frontal prism and heterogeneous plate interface at shallow depth are prone to slow earthquakes. These factors may contribute to slow rupture velocities and large rise times in this area of the megathrust. In fact, Tanioka, Ruff, and Satake (1997) postulated that rupture could proceed in an erratic manner in the presence of a sediment starved corrugated interface. Both the 2020 Sand Point and 1946 Sanak earthquakes are poorly described by teleseismic data. López and Okal (2006) ascribed this feature to destructive interference in all azimuths for surface waves due to the directivity of the rupture and the limitations of historical instrument records to measure waves free from directivity effects. However, this limitation does not affect present day instrumentation. We posit that the source of this discrepancy could instead be due to the slow speed of rupture and slow rise times caused by the features described in Bécel et al. (2017). The similarities between the 1946 Sanak and 2020 Sand Point earthquakes may also extend to their coupling environment. Herman and Furlong (2021) show that spatial variations in displacements caused by coupling between the overriding plate and slab in the 1938 Semidi rupture area, and low coupling throughout the Shumagin segment, would likely cause large right-lateral shear stresses in the section of the segment that produced the strike-slip component of the 2020 Sand Point earthquake. The presence of a strike-slip plane may help illuminate the state of locking in this region of the megathrust. We posit that the dynamic triggering of the megathrust by the strike-slip component of the earthquake occurred in a region of low coupling (Figure 26; Li & Freymueller, 2018). Low coupling would allow shear waves

to cause displacements large enough to promote rupture in this region. The rupture front would then propagate unilaterally to the northeast into a region of potentially higher coupling and higher slip deficits where it would eventually stop (Li & Freymueller, 2018; Xiao et al., 2021). Co-seismic slip along the megathrust propagating from the southwest to northeast of the proposed rupture area is consistent with the Sand Point rupture arresting at the boundary of the July 2021 Chignik rupture area (Figure 31). The western downdip edge of the 2020 Sand Point rupture area also appears to delineate the edge of rupture of the July 2023 Mw7.2 Sand Point earthquake.

The total magnitude of the two-segment rupture from model K3 is Mw7.9 ( $M_o = 8.38 \times 10^{20}$  N-m): Mw7.6 on the strike-slip segment and Mw7.8 on the megathrust. DeSanto et al. (2023) observed with offshore GNSS-Acoustic data that the megathrust remained partially locked after the Mw7.8 Simeonof earthquake and that it potentially held unrelieved strain up-dip of the rupture zone. Xiao et al. (2021) found that the amount of slip deficit left to rupture after the 2020 Simeonof earthquake, updip of the rupture zone (Figure 7 of Xiao et al., 2021), is equivalent to a Mw7.8. Our work therefore seems to suggest that the Sand Point earthquake may have nearly exhausted the remaining slip deficit on the megathrust up-dip of the Simeonof rupture zone. However, we note that our proposed megathrust slip is off-centered from the Simeonof rupture zone and does not include slip up-dip of 20 km. Checkerboards test show that this portion of the inversion is well resolved in the hydrodynamic model but that there is also appreciable smearing in the

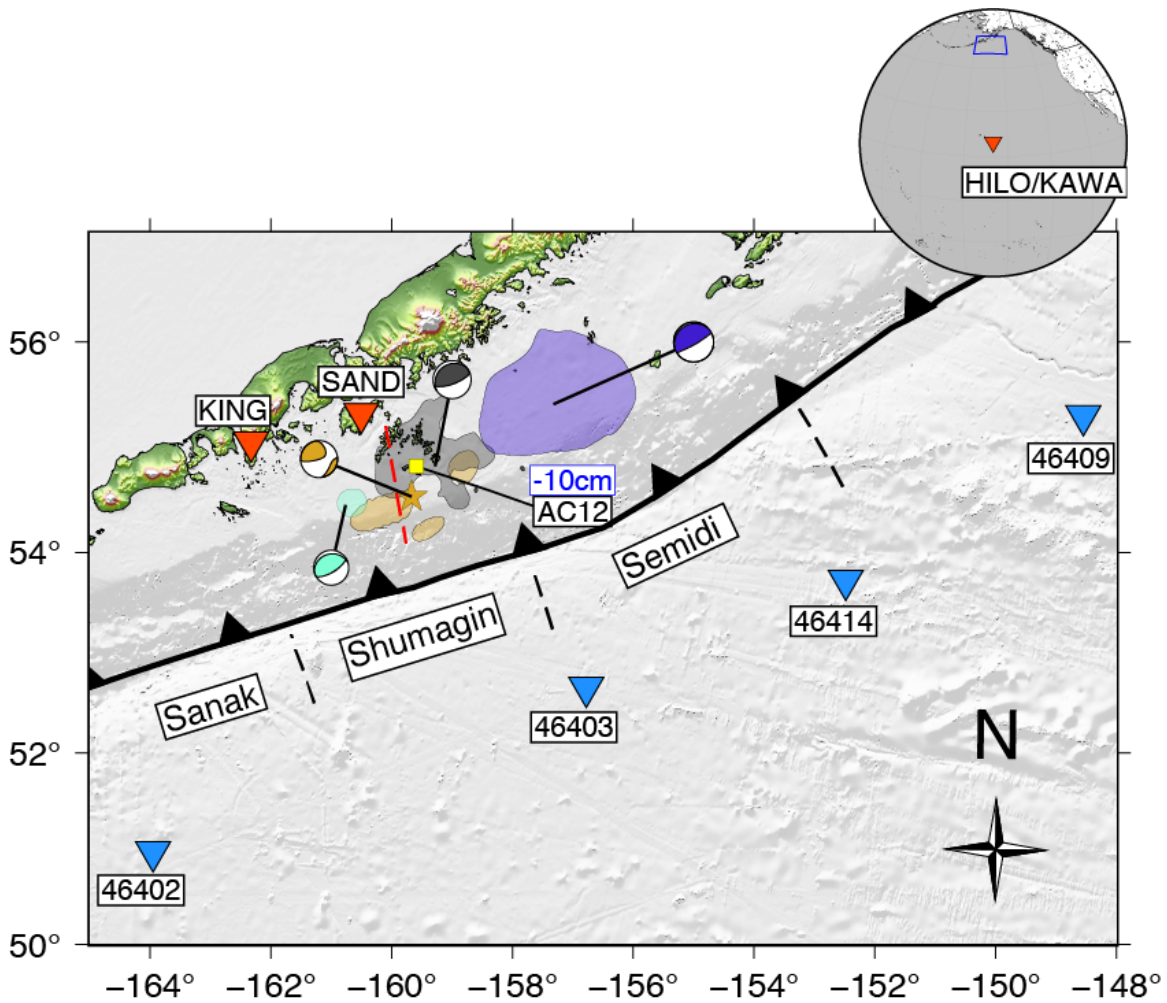


Figure 31. The proposed rupture zone for the 2020 Sand Point megathrust is shown in gold. The 2020 Simeonof rupture zone from Crowell and Melgar (2020) is shown in black, the 2021 Chignik rupture zone from the USGS-NEIC finite fault model for the event is shown in dark blue, and the rupture area for the July 15, 2023, Sand Point earthquake from the USGS-NEIC finite fault model is shown in aquamarine. The surface projection of the strike-slip plane associated with the 2020 Sand Point earthquake is delineated by a dashed red line. The King cove (KING) and Sand Point (SAND) sea level stations are shown in red. DART stations are shown in light blue. The amount of subsidence at GNSS station AC12 (yellow square) for the 2020 Sand Point earthquake is shown to be 10 cm. The inset shows the locations of the coastal sea level stations in Hawai'i. The blue box shows the location of the main study area.

slip inversion (Figure S3). So, whether the un-ruptured sections of the Shumagin segment will experience post-seismic relaxation, leading to decreased hazards, or continue to be loaded as a source of future tsunamigenic events to the Aleutian communities in this region is uncertain.

#### 4.6 Conclusion

We have shown that a strike-slip fault geometry alone is inadequate for generating the tsunami observed following the October 2020 Sand Point, Alaska, earthquake. Using hydrodynamic, static slip, and kinematic slip inversions, we find that there was likely slip along the megathrust in addition to strike-slip faulting. The sea surface deformation necessary to recreate the tsunami waveforms at the Alaskan and Hawaiian sea level stations, as well as the DART stations, requires slip consistent with the megathrust orientation. Our final model suggests that slip on a steeply-dipping strike-slip plane dynamically triggers slip on the megathrust  $\sim 30$  s after event origin time at a location 79 km southwest of the event hypocenter. While the strike-slip plane ruptures at typical speeds (up to 3 km/s), the megathrust likely ruptures at a much slower velocity of 1 km/s. The model results in slip equivalent to a Mw7.6 on the strike-slip plane and Mw7.8 on the megathrust plane, for a cumulative slip equivalent to an Mw7.9 earthquake. We hypothesize that the slow megathrust rupture does not contribute much seismic radiation— much like the 1946 Sanak earthquake— allowing it to go largely unnoticed in traditional teleseismic response. The rupture front propagates at low velocity into a region of high slip deficit updip of the Mw7.8 Simeonof

earthquake but does not slip updip of  $\sim 20$  km. Finally, a submarine landslide is likely necessary to explain the tsunami waveforms at the King Cove coastal sea level station and DART station 46402.

#### **4.7 Acknowledgements**

We would like to thank Diego Arcas for helpful discussions. We would like to thank Benjamin Brooks of the USGS and two anonymous peer reviewers for their helpful feedback on this paper. This work was partially funded by NSF OAC grant No. 1835661 and NASA DISASTERS grant 80NSSC19K1104

#### **4.8 Data and code availability**

The USGS Event Page for the 2020 Sand Point earthquake is available at <https://earthquake.usgs.gov/earthquakes/eventpage/us6000c9hg>. The water level data for the DART stations can be obtained from the DART website (<https://www.ndbc.noaa.gov/dart.shtml>) and for the coastal water level stations can be obtained from NOAA's CO-OP the Environmental Research Division's Data Access Program (ERDDAP) server (<https://opendap.co-ops.nos.noaa.gov/erddap/index.html>), the vertical offset for AC12 was obtained from the GAGE Facility operated by the EarthScope Consortium (<https://doi.org/10.7283/T5NV9G7P>). The sea level inversion code is available from GitHub (<https://github.com/ssantellanes/water-level-inversion>) and archived on Zenodo at Santellanes et al. (2021). The static slip inversions were generated using the FakeQuakes code which is part of the MudPy source modeling toolkit available on GitHub (<https://github.com/dmelgarm/MudPy>), the latest version is archived

on Zenodo at Melgar (2021). The WASP kinematic inversion code is available at (<https://code.usgs.gov/ghsc/neic/algorithms/neic-finitefault/-/releases>). Strong motion accelerometer data and broadband data are available from the Incorporated Research Institutions for Seismology (IRIS) Data Management Center (<https://ds.iris.edu/ds/nodes/dmc/data/types/waveform-data>). High-rate and static Global Navigation Satellite System Data are available from EarthScope (formerly UNAVCO, Inc.) (<https://data.unavco.org/archive/gnss/highrate/> and <https://gage-data.earthscope.org/archive/gnss/products/event>). The data, models, and supplementary figures in this study are available in a USGS ScienceBase data release: <https://www.sciencebase.gov/catalog/item/64c4162cd34e70357a33d4ab> .



## CHAPTER V

### COMPARISONS OF TSUNAMI INUNDATION BETWEEN HOMOGENEOUS AND HETEROGENEOUS EARTHQUAKE SOURCES AT SELECT SITES FOR THE CASCADIA SUBDUCTION ZONE.

#### 5.1 Motivation

Tsunamis of seismic origin have been among the deadliest natural hazards of the 21<sup>st</sup> century. The 2004 Sumatra and 2011 Tohoku-Oki tsunamis caused over 230,000 and 22,000 casualties (Mori et al., 2022). The proximity of these events to the near-shore environment meant that areas near the tsunami source had only minutes to prepare before the onset of inundation. That fact coupled with underestimation of the tsunamigenic potential of the earthquake sources were among some of the chief reasons for the high amount of casualties (Mori et al., 2022). In many ways, these past events mirror what a future Cascadia Subduction Zone (CSZ) megathrust earthquake could be like for the United States Pacific Northwest (USPNW).

Extensive effort has been done to reconstruct the paleoseismic history of the CSZ, leading it to have some of the most complete paleoseismic records for a subduction zone in the world (Atwater & Griggs, 2012; Goldfinger et al., 2012; Kelsey, Nelson, Hemphill-Haley, & Witter, 2005; Walton et al., 2021; Witter et al., 2013). From these records, we know of 19-20 full-margin rupture scenarios to have occurred over the previous 10,000 years (Goldfinger et al., 2012; Walton

et al., 2021). These rupture scenarios have then been translated into full-margin rupture models to produce a series of 15 rupture scenarios that are representative of the previous 10,000 years of tsunami hazards (Witter et al., 2011, 2013). These models produced by the Oregon Department of Geology and Mineral Industries (DOGAMI) have been called the "t-shirt" models as they detail a series of ruptures ranging from small ("SM") to extra extra large ("XXL") with three types of ruptures: splay fault ("1"), shallow buried rupture ("2"), and deep buried rupture ("3") (Witter et al., 2011, 2013). These models serve as the backbone for the hazard assessments performed by the states of Washington and Oregon.

Since the discovery the CSZ's tsunami hazards by those not of the First Nations, various state governments of the USPNW have mandated that hazard assessments be done to ensure the reduction of harm to civilians and economic centers (Priest, 1995). It was these mandates that led to creation of the first tsunami evacuation maps in 1995 by DOGAMI at the behest of the Oregon legislature with the rest of the USPNW states following in later years. These first assessments were limited by the science of their time, as knowledge about the CSZ fault structure was still in its infancy, bathymetry and topography data was still of limited resolution, and the paleoseismic record not yet fully established to discern its behavior. As the science has matured, the USPNW state legislatures are in the course of adopting building codes with focuses on flow depth ("inundation"), flow velocity, and extraordinary debris impacts (American Society of Civil Engineers, 2022; Priest & Allan, 2019).

DOGAMI was bound by Oregon law to consider the "Maximum Considered Tsunami" (MCT), until 2019 when this law was repealed. This former law had focused efforts by DOGAMI and university partners into performing research into discerning what the MCT of the CSZ is. The research done by Priest (1995) was later superseded by the work of Witter et al. (2011) and Witter et al. (2013) when it became clearer that the CSZ can produce XXL rupture scenarios of  $\sim M_w 9.2$ . From that research, the state of Oregon selected the XXL1 scenario as the basis for its tsunami evacuation lines, as it was legally bound to choose the MCT inundation elevation for its risk tolerance.

The state of Washington Department of Natural Resources (WaDNR) is likewise bound by its state government's law, in which they too refer to a MCT. However, whereas Oregon is concerned with a MCT with no mean return period (MRP) limit, WaDNR must consider a MCT within a 2,475-year mean MRP or a probabilistic tsunami not to exceed 2% over a 50 year period, or a deterministic MCT that can reasonably affect a site. In order to fulfil legal requirements, WaDNR worked together with DOGAMI and university partners to select the L1 model as its tsunami risk tolerance for the southern Washington coast. Even though the L model has a 3,333 MRP, WaDNR is required to treat it as a 2,475 MRP event (Eungard, Forson, Walsh, Gica, & Arcas, 2018).

The state of California unlike its USPNW neighbors does not give its state agencies a legal framework for tsunami risk. Instead, they choose a 975-year MRP exceedence for their risk (Thio & Somerville, 2009). The second generation tsunami

evacuation maps were produced at a time when paleoseismic and geodetic records had yet to be combined. And so, their maps are agnostic to the even more extreme MCT scenarios as seen in Witter et al. (2011) and Witter et al. (2013). However, further refinements to these maps have been done by AECOM and university partners since then, for which only the work of Thio and Somerville (2009) is referenced by. Thio and Somerville (2009) noted the limitations of their work and stated that the issue be revisited when more knowledge was available; however, this seems to have yet to occur for California.

In recent years, the five Pacific bordering states have started the process of adopting the American Society of Civil Engineers (ASCE) building codes regarding tsunamis (ASCE 7-22). They use a probabilistic event exceedence from 372 rupture scenarios wherein they use the 100 m depth contour tsunami amplitudes with projections onto the near-shore environment for inundation extent (American Society of Civil Engineers, 2022). The ASCE tsunami scenarios utilize the 1 cm/yr locking model; however, they neglect any other geodetic model, aside from the top of non-volcanic tremor, due to the assumptions made (American Society of Civil Engineers, 2022; Priest & Allan, 2019).

ASCE 7-22 criticizes the DOGAMI models for their lack of surface friction in tsunami inundation, claiming that the models artificially over extend the spatial extent of inundation. Instead, ASCE 7-22 relies on statistical calibration of tsunami inundation that includes land use/cover effects, which they claim is a more realistic representation of tsunami inundation behavior (American Society

of Civil Engineers, 2022). The DOGAMI models have recently been shown to produce realistic inundation models of sandy deposits in the Salmon River estuary by La Selle et al. (2024). So contemporary tsunami modeling setups should be able to produce realistic tsunami inundation extents to a better confidence than was what available in 2012/2013 (La Selle et al., 2024; Witter et al., 2013).

Both the DOGAMI and ASCE homogeneous earthquake sources are widely used by the scientific and engineering communities to establish best practices when it comes to land-use, building codes, and validation of paleoseismic data. However, as we will show in the next sections, both types of models rely on assumptions that underestimate tsunami inundation potential. It is this systemic under-simplification of earthquake source complexity that leads to errors in probabilistic assessments of tsunami hazards. In order to construct robust assessments, heterogeneous source complexity must be fully considered.

**5.1.1 Source complexity and coupling in local tsunami hazard estimates.** Whereas ASCE 7-22 considers extremely simplistic sources, it is not uncommon to use simple, homogeneous ruptures for the CSZ. The 1995 work of DOGAMI utilized a similar simplistic, homogeneous rupture for its first iteration of tsunami evacuation lines (Priest, 1995). Even as more was revealed about the CSZ, the second generation models only adopted a quasi-homogeneous source (Witter et al., 2011, 2013). Again, these works were limited by the science of their time. We know now that for earthquake sources  $> M_w 7$  that sources become increasingly

complex (Hayes, 2017; Mai & Thingbaijam, 2014; Ye, Lay, Kanamori, & Rivera, 2016).

Local tsunami hazard estimates performed by the USPNW states have yet to include source complexity (Eungard et al., 2018; Thio & Somerville, 2009; Witter et al., 2011). However, source complexity has been addressed by the tsunami community (Goda, 2022; LeVeque, Waagan, González, Rim, & Lin, 2017; Melgar, Williamson, & Salazar-Monroy, 2019; Small & Melgar, 2021, 2023). Complex earthquake sources can cause patches of high coseismic slip that can in turn cause areas of higher tsunami inundation runup (LeVeque et al., 2017; Small & Melgar, 2021); likewise, areas near patches of low coseismic slip may have lower tsunami inundation runup. It has been shown by previous works that earthquake source complexity can be potentially discerned by the coupling of the subduction zone fault interface: for Japan (Loveless & Meade, 2015), Alaska (Li & Freymueller, 2018), Chile (Barnhart et al., 2016; Métois et al., 2013), and Peru (Perfettini et al., 2010; Villegas-Lanza et al., 2016).

There exists several competing hypothesis about the current inter-seismic coupling behavior of the CSZ. Since the start of the 21<sup>st</sup> century, global navigation satellite system (GNSS) stations have been deployed en masse throughout the USPNW. The wealth of data they have provided has allowed for geodetic coupling models to be developed based on terrestrial movements (Frankel, Chen, Petersen, Moschetti, & Sherrod, 2015; Li et al., 2018; Schmalzle, McCaffrey, & Creager, 2014). Without adequate GNSS coverage of the CSZ trench, these models have

taken differing approaches to account for trench locking behaviors. These behaviors have been shown to lead to differing values for not only tsunami inundation but also coastal surface displacement (Small & Melgar, 2021). Despite this, we can use the abundance of geodetic models to explore a larger variation of potential tsunami inundation scenarios by generating stochastic models from them (Melgar, 2021; Small & Melgar, 2021)

**5.1.2 Are the ASCE 7-22 and DOGAMI "t-shirt" models still reasonable sources for hazards estimates?** Given what we have discussed about the state of homogeneous models in local tsunami hazards assessment, how accurate are they? The USPNW states are making preparations to use the ASCE 7-22 models as their de jure building codes. Meanwhile, the "t-shirt" models continue to serve as the backbone of tsunami evacuation risk tolerance for Washington and Oregon. Efforts are currently underway to make future ASCE 7 building codes informed with DOGAMI models (Petersen et al., 2024). While we cannot explore the ASCE 7-22 models due to their unpublished and undocumented nature. We can only gather what their models look like from conference proceedings and documents provided by tsunami-curious civil engineers. Of which, we know that the 372 models they claim to use for ASCE 7-22 are homogeneous models based on the 2014 and 2018 USGS National Seismic Hazard Maps, and that they select a 1-in-2475 exceedence (note the shift from MRP — previous legislation in the USPNW uses both interchangeably, which is incorrect) due to seismic hazard analysis using the same number (American Society of Civil

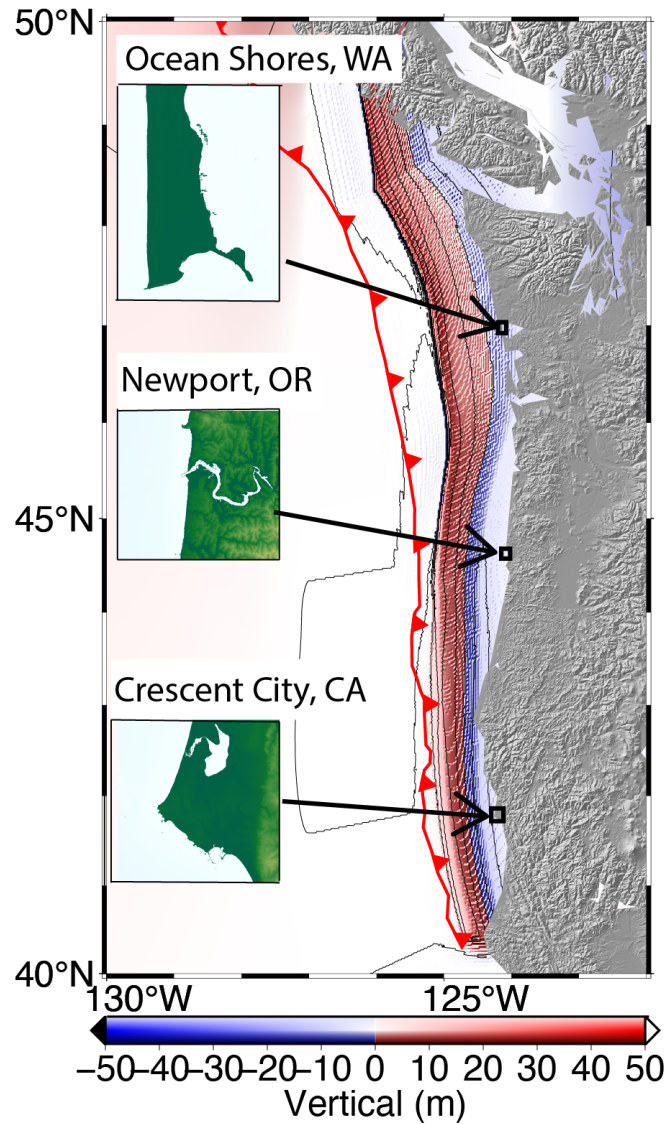


*Figure 32.* Map of the study area. Insets show the areas of interest that were used for modeling of tsunami inundation. Black arrows point from the inset to the locations of the areas of interest on the main map. CSZ is denoted by the red subduction zone symbols. The XXL1 "t-shirt" vertical deformation model is shown by the polar plot. Contours are plotted at 5 m intervals.

Engineers, 2022; Priest & Allan, 2019). The logic tree for ASCE 7-16/22 (Can be seen as Figure 2-8 in Priest & Allan, 2019) details that use two variations of the 1 cm/yr model: mid-point of fully locked zone and 1 cm/yr contour and the 1

cm/yr models. The third they use is the top of non-volcanic tremor zone. However, these models are not publicly available for scholarly use. We can only analyze the publicly available DOGAMI "t-shirt" models.

When we compare the XXL1 "t-shirt" from Figure 32 with the heterogeneous sources seen in Figure 33, we see the spatial variations between slip and vertical displacement between the two, and how that poses significant differences between tsunami inundation behaviors. The "t-shirt" models have three major caveats: (1) they model slip quasi-homogeneously, (2) they lack geodetic constraints, and (3) they do not consider more frequent ruptures on either the northern (Atwater & Griggs, 2012) or southern sections (Goldfinger et al., 2012) of the CSZ. We know likewise that ASCE 7-22 must suffer from similar issues, as they claim to use the 2014 and 2018 USGS National Seismic Hazard Maps for their events, which do not make use of any advances proposed by Goldfinger et al. (2017); Nelson et al. (2021).

In this study, we show that heterogeneous slip from 200 stochastic earthquake sources changes the risks faced by three sites — Ocean Shores, WA; Newport, OR; and Crescent City, CA — by varying degrees compared to the DOGAMI rupture models (Figure 32). We show that the XL1 scenario has inundation  $> 90^{\text{th}}$  percentile compared to heterogeneous sources. Meanwhile, the L1 scenario has inundation that is in the  $45^{\text{th}}$ - $55^{\text{th}}$  percentile. We then compute probabilistic tsunami hazard curves and maps for the three sites following the standard set by DOGAMI in Witter et al. (2013). Our maps differ slightly from the

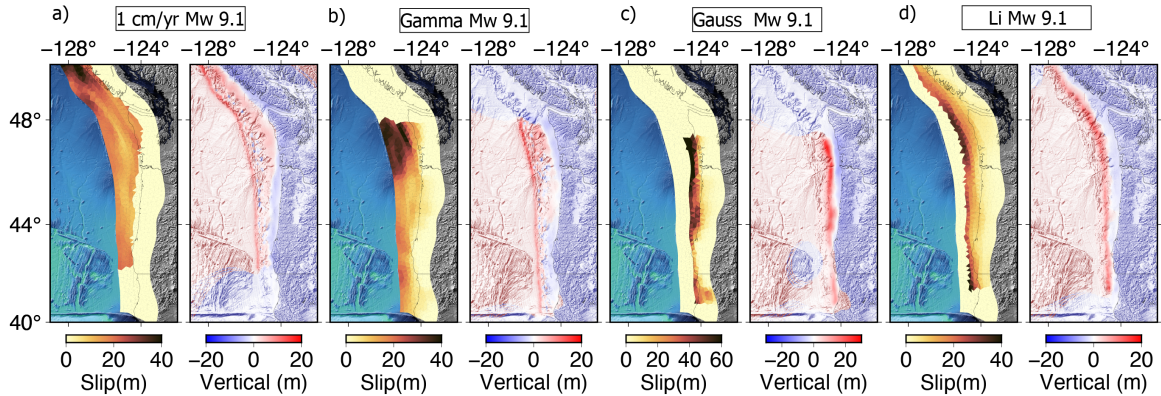


*Figure 33.* Heterogeneous slip and vertical deformation maps for the four geodetic families used in this study.  $M_w$ 9.1 source ruptures for a.) 1 cm/yr, b) Gamma, c) Gauss, and d) Li geodetic models. Subduction zone interface geometry comes from Hayes et al. (2018).

official tsunami evacuation lines for Newport, OR and Ocean Shores, WA. However, we find that Crescent City, CA’s tsunami evacuation lines do not adequately capture the risk faced by heterogeneous rupture of the CSZ.

## 5.2 Data and Methods

### 5.2.1 Stochastic modeling of geodetically constrained ruptures.

We use the FakeQuake methodology described by Melgar, LeVeque, et al. (2016) and Goldberg and Melgar (2020) and applied by Small and Melgar (2021) and Small and Melgar (2023) for modeling of stochastic sources used in this study.

However, we limit ourselves to ruptures generated by four geodetic rupture models:

”1 cm/yr” (Frankel et al., 2015), ”Gauss” (Schmalzle et al., 2014), ”Gamma” (Schmalzle et al., 2014), and ”Li” (Li et al., 2018). The ”1 cm/yr” model details the 1cm/yr coupling contour (25% coupling) limit of slip as shown by Frankel et al. (2015). This model follows the assumption that no coseismic slip extends

deeper than the 1 cm/yr contour (Frankel et al., 2015). As a result, the model has no along-strike variability, meaning that slip is likely everywhere where mean slip is not 0 (Frankel et al., 2015; Melgar, Fan, et al., 2016). The "Gauss" model enforces a Gaussian distribution of locking with depth, and it penalizes slip to enforce mean locking above the 30 km depth contour (Schmalzle et al., 2014). The "Gamma" model enforces that the slab is fully locked with large slip deficits at the CSZ trench, and that they decay monotonically with an assumed shape factor gamma (Schmalzle et al., 2014). The "Li" model assumes a viscoelastic approach to locking along the trench (Li et al., 2018). These three models have varying along-strike maximum depth, and they vary the strength of locking along-dip and along-strike (Li et al., 2018; Schmalzle et al., 2014), which can be best visualized by Figure 33. Small and Melgar (2021) note that models constrained by geodetic locking do not have coseismic slip that follows the pattern of interseismic locking. Instead, they detail that higher locking areas have more frequent high slip. By using these geodetic constraints we make the assumption that the slip in the next CSZ earthquake will be correlated with one of these models. Unfortunately, the validity of these models is unknown at the present moment because of the absence of seafloor geodetic measurements, so we include the "1 cm/yr" model, which makes minimal assumptions.

For each of the four mean models of choice, we generate 25 ruptures with moment magnitudes that fall into either the L or XL classifications described by Witter et al. (2011) and Witter et al. (2013) for a total of 200 inundation scenarios.

We select the XL scenario over the XXL scenario for one reason: coseismic subsidence of Crescent City was so substantial that it rendered the vast majority of Crescent City below mean high water. The XL scenario tapers off coseismic slip for the southern section of the CSZ (Witter et al., 2013), so we select it in order to compare against the heterogeneous sources. As the only difference between the XL and XXL classes is this tapering, the heterogeneous XL-like sources can take on behavior akin to an XXL class event, which we permit to allow for a full exploration of tsunami inundation range. We set the  $M_w$  bins for the L scenarios as  $9.0 \leq M_w < 9.1$ , and for the XL scenarios  $9.1 \leq M_w \leq 9.2$ . We disregard length and width estimates of the L and XL classes so as to allow for large slip, compact area events in the northern and southern sections of the CSZ. We follow the logic of Witter et al. (2013) and set the annualized rate of occurrence for L-like scenarios to 1-in-3,333 years and for XL-like scenarios to 1-in-5,000 years. It is important to note that we do not choose to follow the Gutenberg-Richter relationship for probabilistic hazard analysis, as we are exploring the range of possible tsunami inundation behavior from various heterogeneous sources. Finally, we calculate the total coseismic deformation for each rupture model. We then use it as the initial condition for tsunami modeling.

**5.2.2 Tsunami modeling.** As stated prior, we use the total coseismic deformation from each rupture model as the initial condition for tsunami propagation. This deformation is obtained by combining the vertical displacement from elastic dislocation with the "pseudo-vertical" response from horizontal

displacement of sloping bathymetry (Tanioka et al., 1997). We do not consider secondary sources of tsunamigenesis such as submarine landslides, splay faulting, or plastic deformation of the shallow wedge in the tsunami initial condition. These quantities — though they do contribute to total tsunami energy and increased tsunami amplitudes (Ma & Nie, 2019) — are difficult to systemically and stochastically model. Thus, underestimation of tsunami amplitudes and inundation from each of these sources may be likely should they occur locally near any of the three areas of interest.

Following the definition of the initial tsunami condition, we use the finite volume depth-averaged tsunami modeling code GeoClaw (Clawpack Development Team, 2020). It is able to numerically solve the two-dimensional non-linear shallow water equations. It utilizes adaptive mesh refinement (AMR) such that areas of large tsunami complexity are automatically refined to higher discretization levels. The model domain is shown as the extent of Figure 32. For propagation in the open ocean, we use SRTM15, which provides resolution of bathymetry and topography at 15 arcsecs (Tozer et al., 2019) which is what we use for AMR levels 1-3. We interpolate up from the 1/9 arcsec provided by continuously updated digital elevation model (CUDEM) for Ocean Shores, WA and Newport, OR to 1 arcsec (Cooperative Institute for Research in Environmental Sciences, n.d.). We interpolate up from the 1/3 arcsec mean high water digital elevation model (DEM) for Crescent City, CA (NOAA National Geophysical Data Center, n.d.) to 1 arcsec. These 1 arcsec grids are then used for our finest discretization and

for our inundation regions. Lastly, we permit inundation up to elevations of 80 m. We recognize that this value is two times higher than the maximum inundation surveyed from the Tohoku-Oki tsunami (Mori, Takahashi, Yasuda, & Yanagisawa, 2011); however, our focus is to examine all potential inundation behaviors.

We run the tsunami models for 2 hours of model time. Time-stepping is allowed to vary such that the Courant-Friedrich-Levy condition stays at a constant 0.75. For tsunami inundation, we employ a Manning coefficient of 0.025 (which is held constant), and we utilize the drying and wetting feature of GeoClaw to allow changes to our grid cells as the simulation progresses.

We make the assumption that rupture velocities are faster than the tsunami wave velocities so that we can have instantaneous coseismic deformation for the tsunami initial condition. The assumption has little effect on the near-shore tsunami amplitudes (A. Williamson et al., 2019).

**5.2.3 Comparisons of hazards between homogeneous and heterogeneous ruptures.** Although we make use of the probabilistic tsunami hazard analysis (PTHA) framework for inundation, we strongly state that this work does not constitute a PTHA assessment. Merely, we are interested in average variation of inundation that comes from heterogeneous earthquake sources. As stated prior, we do not utilize a Gutenberg-Richer distribution, so this immediately rules out a true PTHA for the region. Also, as stated prior, we operate on the assumption that each rupture that falls in to either the L-like or XL-like class and has either a 1-in-3,333 or 1-in-5000 chance of occurring during a year.

Rather than use the PTHA equation formulated by Geist and Parsons (2006), we adopt a much more simpler probabilistic equation. Suppose we have events  $E_1, E_2, E_3, \dots, E_k$  each with an annual probability  $p_k$ . Since each realization is an independent event, we can produce the following equation:

$$\hat{p} = 1 - (1 - p_1)(1 - p_2)\dots(1 - p_k), \quad (5.1)$$

Where  $\hat{p}$  is the probability that at least one of the events happens. From this equation, we can show that for any exceedence value  $h$ , the probability  $P(h)$  that inundation occurs at a point on the grid for events  $E_k$  where  $h_k > h$  becomes:

$$P(h) = 1 - (1 - p_1)\dots(1 - p_n), \quad (5.2)$$

where  $n$  are the number of times the grid point is inundated.  $n$  can be  $\leq$  the total number of events  $k$ . From these equations we are able to produce hazard curves and maps for each of our three sites of interest. In addition to these maps, we construct violin plots that show the probability distribution function of the mean for all grid points that are inundated by each rupture scenario. Violin plots show the breakdown of inundation behavior by geodetic model and by the grand total.

We create maps that show the spatial differences of inundation behavior for the three sites. We compare the results of the heterogeneous L-like and XL-like models to their respective deterministic (e.g., one model run per "t-shirt" class), homogeneous models. We take the mean of the L-like and XL-like models and make them into geospatial raster files. We assert that grid cells that have a mean

inundation  $\geq 0.3$  m to be "wet" and assert that grid cells below this threshold to be "dry." This threshold is introduced to remove the effects of extreme events that skew the mean behavior of the inundated grid cells. We utilize the Jaccard similarity index (JSI) for computing the similarity between the homogeneous raster files and the L-like and XL-like heterogeneous rupture mean inundation raster datasets (Jaccard, 1912). JSI values range from 0 – 1, with 0 indicating no overlap between datasets and 1 indicating a perfect match.

Lastly, we create hazard maps that show the probability of inundation above 0 m. We set three decision exceedence boundaries: 0.004 ( $\sim$  1-in-2,475 years), 0.01 ( $\sim$  1-in-100 years), and 0.02 ( $\sim$  1-in-50 years). The latter two boundaries are selected based on the various probabilities of interest considered by the ASCE for flooding and surge hazards (American Society of Civil Engineers, 2022). We then use equations 1 and 2 to produce exceedence maps that show the spatial variation of the L-like and XL-like heterogeneous source models compared to the official tsunami evacuation lines used by Washington, Oregon, and California.

### 5.3 Results

We start our analysis by first comparing the mean inundation of the 200 ruptures to the two "t-shirts" of interest. We then progress to explore the spatial variations in inundation between the homogeneous and heterogeneous source models. Lastly, we show what new hazard maps look like when accounting for heterogenic behavior.

**5.3.1 Mean tsunami inundation behavior.** The mean tsunami inundation behavior for the three sites of interest shows that there does not appear to be a correlation between geodetic locking models and inundation (Figure 34). What is clearly evident is that the L1 model consistently ranks between the 45<sup>th</sup> - 55<sup>th</sup> percentiles of heterogeneous L-like sources for Ocean Shores and Newport. Crescent City has the L1 mean inundation at the 75<sup>th</sup> percentile. Overall, this behavior means that the L1 scenario represents only the mean behavior that can be expected from heterogeneous rupture sources. The XL1 scenario constantly ranks > the 90<sup>th</sup> percentile for all geodetic families and even in the grand total. The XL1 scenario thereby represents an extreme scenario with its average of all inundated points being between 12-15 m among the three sites of interest.

While Figure 34 shows the top-level view of the tsunami inundation behavior, it neglects to account for the spatial variability of the percentile of inundation for each grid cell. Figure 35 shows the extent the L1 percentile of inundation. Again, we see that the vast majority of pixels are in 45<sup>th</sup>-55<sup>th</sup> percentiles for the three sites of interest. However, we start to see differences in expected behavior compared to the official tsunami evacuation lines. Pockets of low percentile inundation are noticeable for Ocean Shores, especially on the bay side section of the peninsula, which may suggest little-to-no inundation in those regions. Newport is expected to depart from the tsunami evacuation lines here, as they use the XXL1 scenario — highlighted by Figure 35 inset. Crescent City's percentile of inundation does not seem to match its tsunami evacuation lines at all

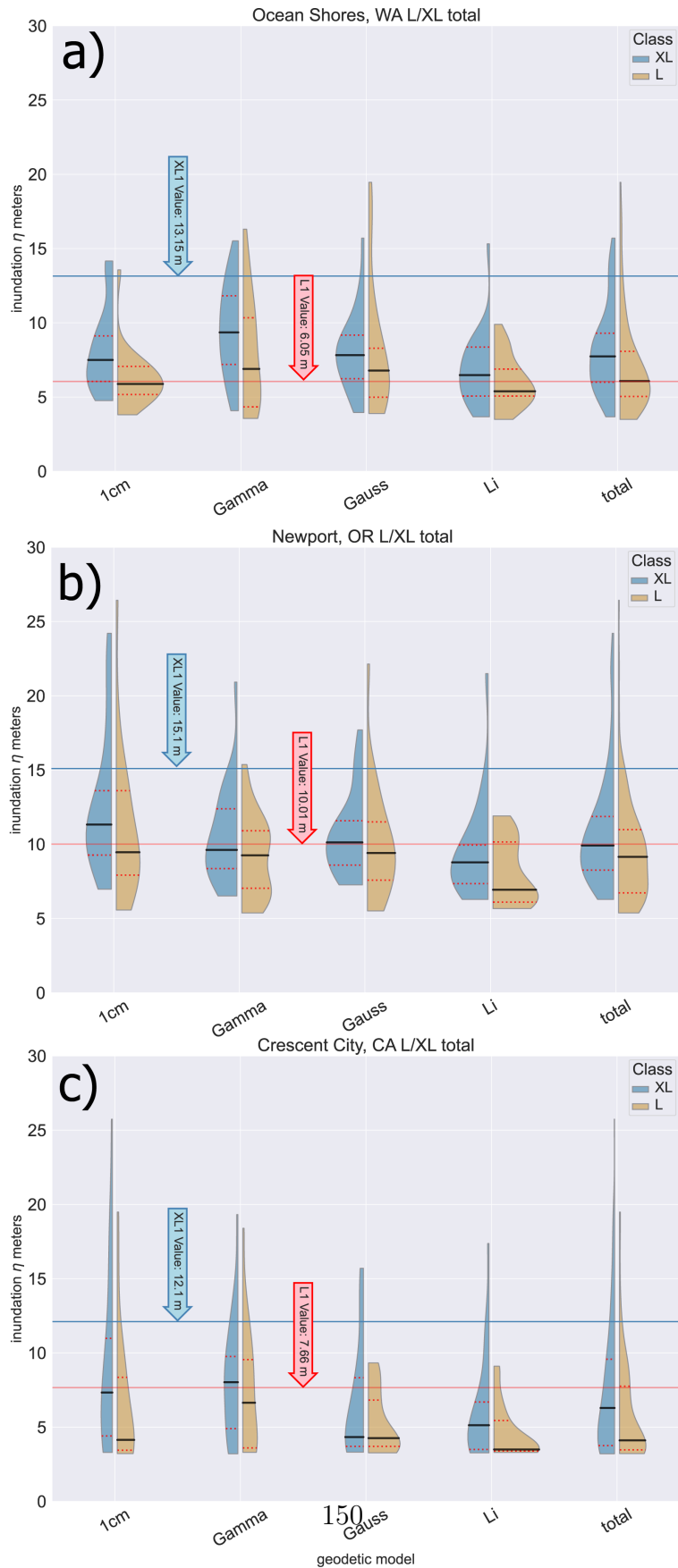
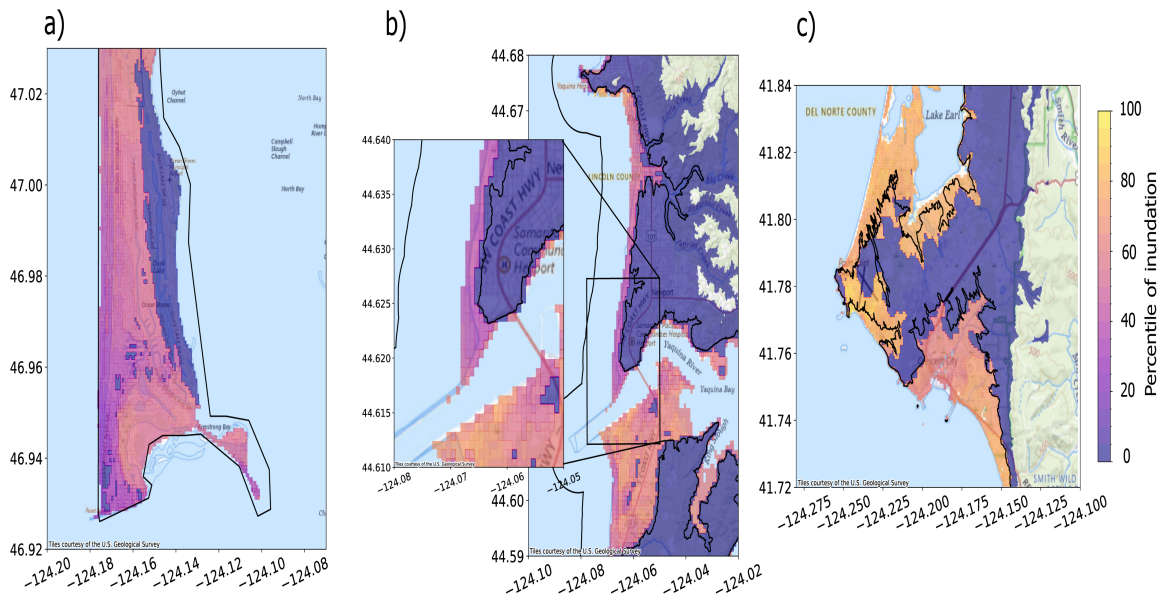


Figure 34. Violin plots of the mean tsunami inundation behavior for each geodetic model and all models. Probability distribution functions shows distribution of the

on the western perimeter and near Lake Earl; however, they do a decent job on the downtown and southern section area. As stated before, the grid cells are close to the 75<sup>th</sup> percentile of inundation.



*Figure 35.* Maps that show the L1 percentile of inundation for each grid cell for a) Ocean Shores, WA; b) Newport, OR; and c) Crescent City, CA. Black lines denote the official tsunami evacuation lines used for by the states of Washington, Oregon, and California. Streets and geographic information tiles are provided by the USGS.

Figure 36 shows the spatial extent of the XL1 percentile of inundation. All of the three sites appear to have the deep yellow coloring indicative of percentile of inundation > 90<sup>th</sup> percentile. Ocean Shores is entirely inundated in this scenario. We see that more grid cells inundate past the tsunami evacuation lines for Newport: noticeably, to the north of Yaquina Bay (Figure 36 inset). Crescent City has further inundation inland; however, here as well shows that the XL1 scenario represents a high percentile outcome.

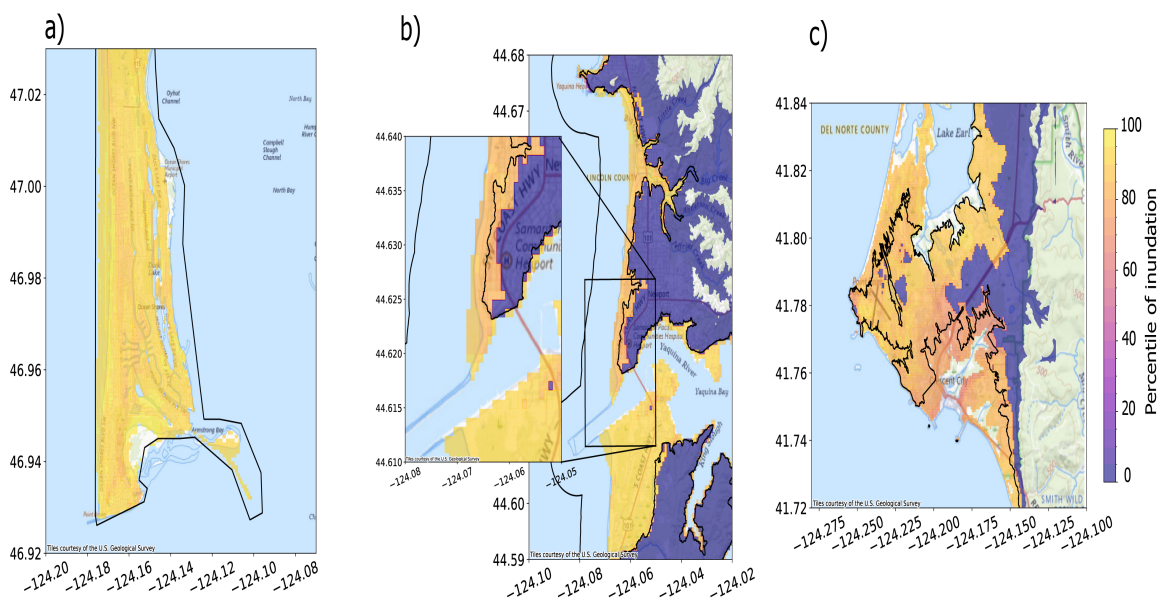


Figure 36. Maps that show the XL1 percentile of inundation for each grid cell for a) Ocean Shores, WA; b) Newport, OR; and c) Crescent City, CA. Black lines denote the official tsunami evacuation lines used for by the states of Washington, Oregon, and California. Streets and geographic information tiles are provided by the USGS.

### 5.3.2 Differences between homogeneous and heterogeneous

**ruptures..** Figure 37 shows the difference between the L1 source rupture model and the L-like heterogeneous models. Grid cells are considered to be "dry" if the mean inundation value is  $< 30$  cm and "wet" if  $\geq 30$  cm. We see that for Ocean Shores that there are pockets of "dry" grid cells from the L1 model on the southern and eastern extents of the peninsula. With the L-like heterogeneous sources, the entirety of Ocean Shores is "wet." The JSI for Ocean Shores is 0.92 (Table 2), indicating that the homogeneous and heterogeneous sources cause tsunami inundation that are similar yet not exact. In the case of Newport, we see the largest differences in North Newport (Figure 37 inset). The L1 scenario fails to "wet" to the first streets; however, the L-like heterogeneous sources are able to "wet" past the tsunami evacuation line. South Newport, which has steep topographic variations, does not see as many differences. This reflects in the overall JSI of 0.93 (Table 2). Crescent City is the site with largest differences between the homogeneous L1 and heterogeneous L-like sources with a JSI of 0.80 (Table 2). In these scenarios, all of downtown Crescent City is considered "wet" with only the central area remaining "dry."

Figure 38 shows the differences between the XL1 source rupture model and the XL-like heterogeneous models. In this case, there is no difference in "wet" and "dry" inundation behavior for Ocean Shores. The JSI is 1 — a perfect match (Table 2). For Newport, the majority of differences between the homogeneous and heterogeneous cases continues to be in North Newport (Figure 38 inset). Grid

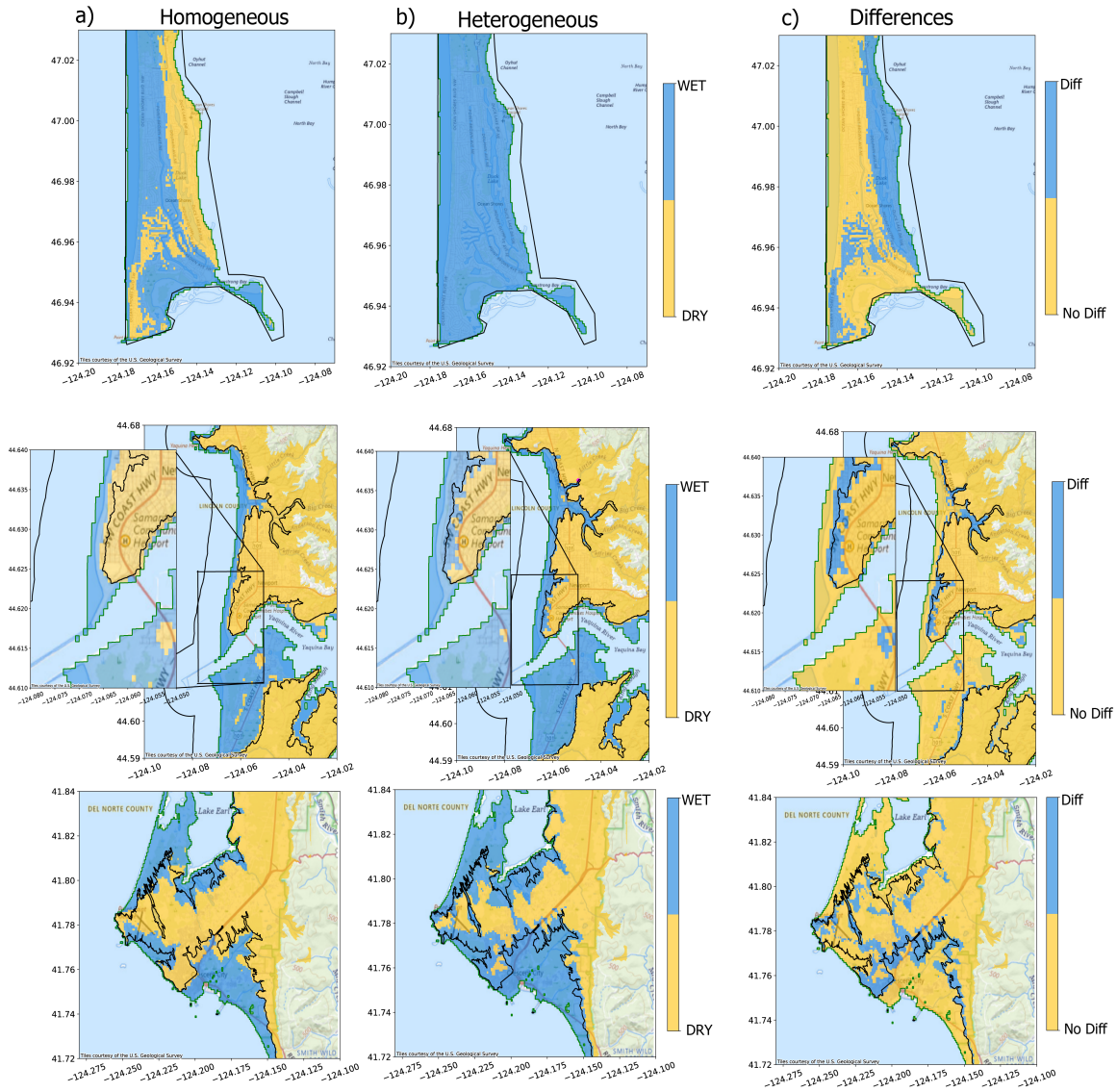


Figure 37. Maps that show the L1 homogeneous where "wet" is  $\geq 30$  cm and dry is  $< 30$  cm (a), average of 200 heterogeneous where "wet" is  $\geq 30$  cm and dry is  $< 30$  cm (b), and difference between "wet" and "dry" grid cells for Ocean Shores, WA; Newport, OR; and Crescent City, CA. Black lines denote the official tsunami evacuation lines used for by the states of Washington, Oregon, and California. Streets and geographic information tiles are provided by the USGS.

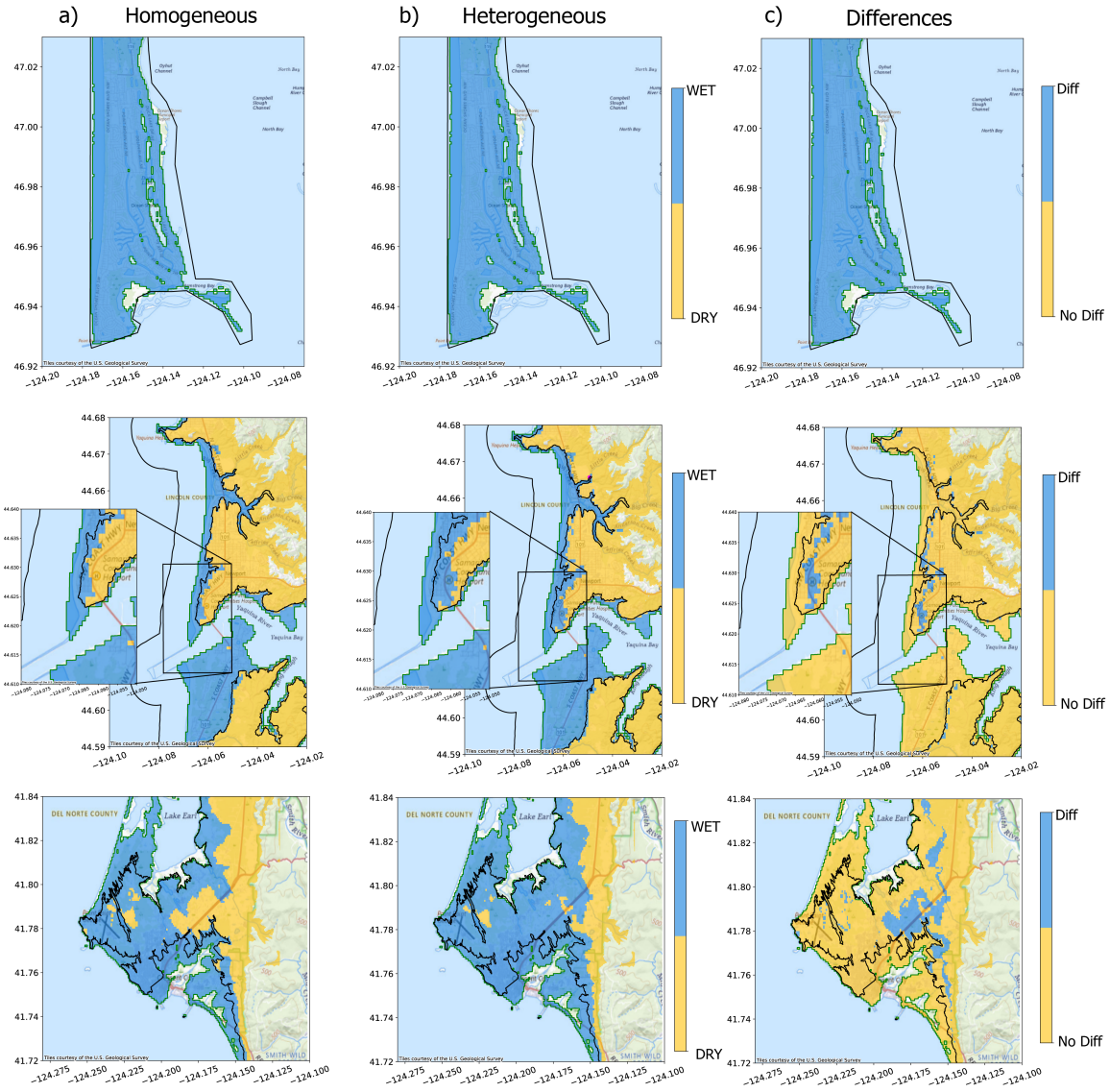


Figure 38. Maps that show the XL1 homogeneous where "wet" is  $\geq 30$  cm and dry is  $< 30$  cm (a), average of 200 heterogeneous where "wet" is  $\geq 30$  cm and dry is  $< 30$  cm (b), and difference between "wet" and "dry" grid cells of a) and b) for Ocean Shores, WA; Newport, OR; and Crescent City, CA. Black lines denote the official tsunami evacuation lines used for by the states of Washington, Oregon, and California. Streets and geographic information tiles are provided by the USGS.

Site	L-like (0-1)	XL-like (0-1)
Ocean Shores	0.92	1
Newport	0.93	0.97
Crescent City	0.80	0.93

Table 2. Jaccard similarity indices for for Ocean Shores, Newport, and Crescent City of the homogeneous and heterogeneous spatial rasters of "wet" and "dry" tsunami inundation.

cells continue to be "wetted" further inland than by the XL1 case, even "wetting" past US Highway 101. The JSI is 0.97, which indicates a greater similarity between the spatial extents of "wet"/"dry" behavior of the homogeneous and heterogeneous ruptures; however, the majority of differences are in locations of non-negligible population density (Table 2 and Figure 38). Crescent City continues to see extraordinary spatial extent of inundation further inland with both XL homogeneous and heterogeneous models. The difference between the two being mostly in the total coverage of "wet" cells around US Highway 101. The JSI is 0.93 indicating that the two are roughly similar to each other; however, again, the differences appear to be in areas of non-negligible population density (Table 2 and Figure 38).

**5.3.3 Tsunami hazard maps.** When we plot the tsunami hazard maps against the tsunami evacuation lines for the three sites of interest, we see the limits of using homogeneous source models as the basis for a MCT

exceedence estimates. As seen in Figures 39 and 40 insets, North Newport's tsunami evacuation lines, which are set to the XXL1 scenario, fail to constrain the hazard extent of heterogeneous L-like and XL-like scenarios to the immediate north of Yaquina Bay. However, areas with steeper variations of topography constrain inundation extent similar to the DOGAMI evacuation lines. Crescent City, which uses a 975 MRP event exceedence, fails to encapsulate the extent of hazards and risks of the CSZ for any of the L-like and XL-like sources. Either sources' 1-in-2475 exceedence is far beyond the extent of the official California evacuation lines. Moreover, one thing is clearly evident. Heterogeneous sources on average and with MRPs of the L and XL homogeneous events inundate further than their respective homogeneous events' exceedences.

## **5.4 Discussion**

The primary focus of this study is the comparison between homogeneous and heterogeneous earthquake sources to be used as the tsunami initial condition for inundation of three sites of interest. Our results have shown that while the XL1 scenario represents an extreme case with its inundation its inundation extent is less than that of the heterogeneous sources. We discuss the implications of this result below.

### **5.4.1 Differences of homogeneous and heterogeneous models.**

The results appear to be paradoxical. The XL1 scenario produces high amounts of tsunami inundation on average for all of the grid cell it inundates. However, the spatial inundation extent is less than those by the mean and probabilistic behavior

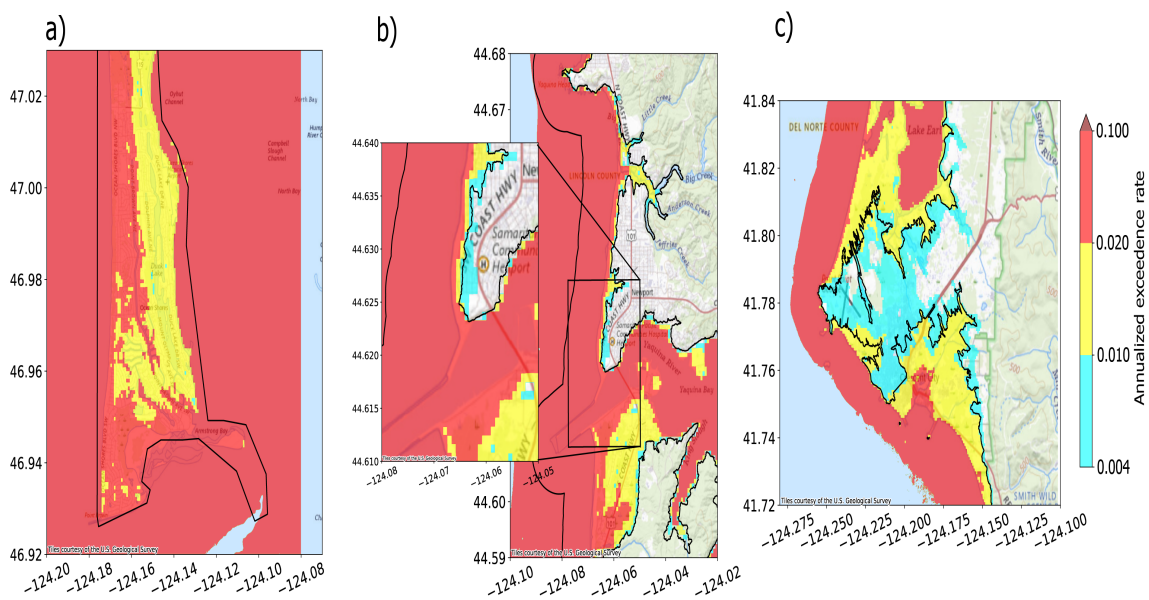
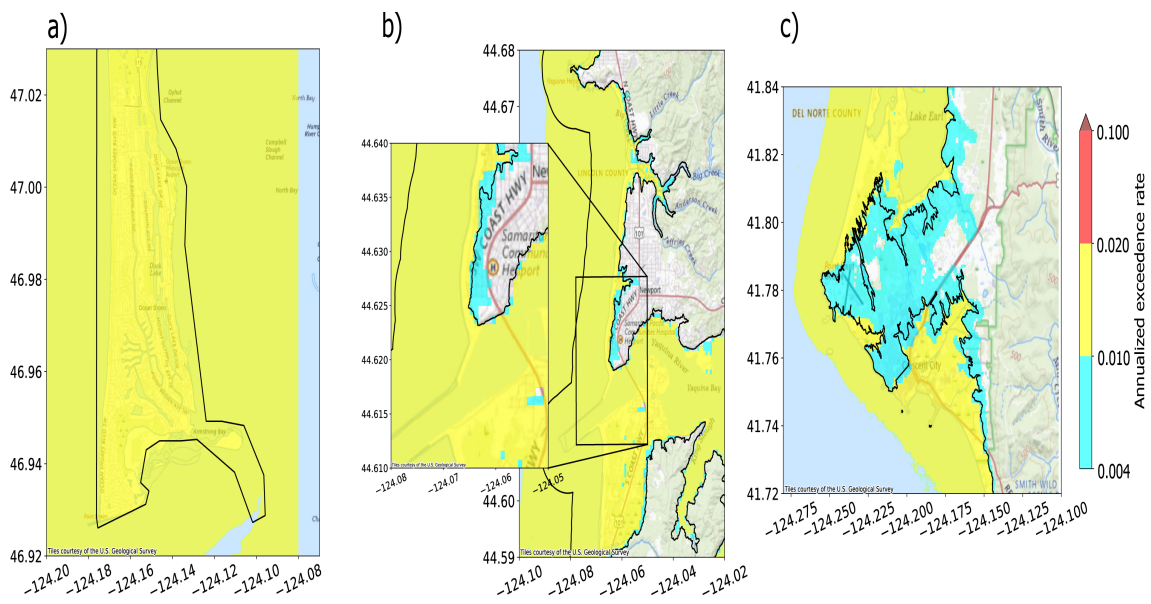


Figure 39. Maps that show the 1-in-50, 1-in-100, and 1-in-2475 year exceedences for the L-like heterogeneous sources for a) Ocean Shores, WA; b) Newport, OR; and c) Crescent City, CA. Black lines denote the official tsunami evacuation lines used for by the states of Washington, Oregon, and California. Streets and geographic information tiles are provided by the USGS.



*Figure 40.* Maps that show the 1-in-50, 1-in-100, and 1-in-2475 year exceedences for the XL-like heterogeneous sources for a) Ocean Shores, WA; b) Newport, OR; and c) Crescent City, CA. Black lines denote the official tsunami evacuation lines used for by the states of Washington, Oregon, and California. Streets and geographic information tiles are provided by the USGS.

of the heterogeneous sources. There are two drivers of the increased tsunami inundation extent: (1) source complexity in the near trench zone and (2) coseismic coastal subsidence.

Small and Melgar (2021) showed that high slip deficits in coupling lead to more frequent high slip in stochastically generated events. These areas of high slip tend to happen more in the near trench area for the 1 cm/yr and Gamma models, thereby producing more tsunamigenic scenarios. This correlation is modestly seen in Figure 34c with Crescent City, where it experiences higher tsunami inundation from these two geodetic families. However, this fact alone does not explain the further inland extent of tsunami inundation seen across all models for Newport and Crescent City.

All of these rupture families are more likely to produce coseismic coastal subsidence than coastal uplift, which is widely believed to have occurred during the 1700 rupture (Melgar, 2021; Walton et al., 2021; Witter et al., 2013). Coseismic coastal subsidence allows for more area to be below sea level thereby allowing for tsunami waves to inundate further inland. This manifests in the XL1 scenario for Ocean Shores and Crescent City (Figure 39). Heterogeneous sources of L- and XL-like categories also produce various amounts of coseismic coastal subsidence. It can be so severe that the entire sites of interest can be fully below mean high water before the first tsunami wave arrives. The only site that did not have this event occur was Newport, which only saw modest coastal coseismic subsidence of 0-8 m for the 200 rupture scenarios. Due to the source complexity of these scenarios,

it was common for the two out of the three sites furthest from the main rupture asperity to have 0-3 m of tsunami inundation while the other site local to the main asperity had 10-20 m of tsunami inundation. This behavior was seen in the 2011 Tohoku-Oki tsunami wherein local tsunami runup was  $> 40$  m for places near the main rupture asperity (Mori et al., 2022, 2011).

The ASCE 7-22 tsunami inundation model appears to further inundate Crescent City compared to the official tsunami evacuation lines (see ASCE 7 TsunamiDatabase). Their model makes use 1 cm/yr and top of the non-volcanic tremor zone. The latter of which has been shown by Small and Melgar (2021) to produce substantial coseismic coastal uplift to the point where it represents a much less likely scenario. The ASCE 7-22 codes only assign a probability of 0.3 to this model; however, it should be weighed much lower given its inability to recreate paleoseismic data. The 1 cm/yr model, as has been shown by Small and Melgar (2021) and this study, produces much larger tsunami inundation values on the southern section of the CSZ. While this model makes the fewest assumptions, it can lead to an overestimation of tsunami inundation extent if not properly accounted for with the suite of other likely geodetic models.

#### **5.4.2 Moving towards a probabilistic maximum considered**

**tsunami.** For two of the three sites of interest, the probabilistic maps do not differ much from the official tsunami evacuation lines used by their state emergency planners. WaDNR and DOGAMI have done extensive research into preparing for the next CSZ event, and it is reflected in the similarity of the tsunami evacuation

lines to even the XL-like heterogeneous ruptures. Only Crescent City does not have tsunami evacuation lines — at the present moment — that encapsulate the risks of homogeneous or heterogeneous ruptures of the CSZ. Even ASCE 7-22 goes further inland with its tsunami run-up elevation than the model used by California (American Society of Civil Engineers, 2022). Our results cannot be generalized outside of these three sites of interest. Local bathymetry and topography vary substantially throughout the USPNW, so it remains unclear how other population centers may fair with a heterogeneous CSZ rupture. Their risk may be able to be estimated to a high confidence like with Ocean Shores and Newport, or to a low confidence as shown by Crescent City.

While the approach by the ASCE for their tsunami model is un-published and un-peer reviewed, there is use in considering what a MCT with fixed MRP may pose for the USPNW. While they describe a 1-in-2,475 MRP event, with no-to-little paleoseismology, geodetic, or other geophysical backing, the work done by this study can be used in the future framework currently under development that satisfies both the civil engineering need for a reference MCT and the CSZ science community's need for geophysical-based rupture models for earthquake and tsunami modeling. The various USPNW state legislatures are in the process of ratifying new building codes that choose a MCT of 1-in-2,475 MRP. It is imperative that this reference event contain the best knowledge of the tsunami inundation behavior if substantial casualties are to be avoided in the next CSZ rupture. Although, they must come to terms that each great earthquake rupture is different, and that

building in the currently known tsunami inundation zone is a dangerous task. While earthquake sources are the largest source of uncertainty in PTHA (Geist & Parsons, 2006), inundation physics of the anthropogenic environment is the next (Mori et al., 2022; Small & Melgar, 2021).

## 5.5 Conclusion

We have shown the range of tsunami inundation behaviors from 200 stochastically generated heterogenic ruptures scenarios for the sites of Ocean Shores, WA; Newport, OR; and Crescent City, CA. We find that while the homogeneous scenarios have mean tsunami inundation values between the 45<sup>th</sup>-75<sup>th</sup> percentiles (L1) and > 90<sup>th</sup> percentile (XL1), the L-like and XL-like heterogenic sources have a greater spatial extent on average. This greater spatial extent is constrained well by the tsunami evacuation lines of Ocean Shores and Newport; however, Crescent City's lines fail to account for the greater spatial extent of both homogeneous and heterogeneous rupture sources.

We would like to thank Jason "Jay" Patton of the California Geological Survey and Jonathan Allan and Lalo Guerrero of the Oregon Department of Geological and Mineral Industries for providing access to the tsunami evacuation lines used by California and Oregon. We also wish to thank Randall "Randy" J LeVeque for providing us with the python notebook to create the initial tsunami conditions from the "t-shirt" models for use in GeoClaw, as well as his PTHA tutorial. We wish to thank two anonymous civil engineers for sharing and discussing the methodology of ASCE 7-22 with the authors of the study.



## CHAPTER VI

### CONCLUSION

This dissertation has described in detail the data collected from the worldwide tsunami observing network for the HTHH event including 35 DART buoys and 114 tide gauge stations. The eruption of HTHH produced the largest volcanic source tsunami in the modern age of tsunami observation and it was recorded on a global scale. This dissertation has identified three potential phases of the tsunami. The first arrival is almost certainly a Lamb wave phase which travels faster than a traditional tsunami. Secondary phases are most likely a complex amalgam of traditional tsunami and atmospheric effects such as internal gravity waves. Additionally, the tsunami codas are long, we posit that the Pacific basin portion of the tsunami is likely to have been the result of processes like those in meteotsunamis such as Proudman resonance induced by the Lamb wave front, with various coastal areas seeing also effects from Greenspan and shelf resonance. Overall, this dissertation believes, that, while processes at the volcanic edifice, such as caldera collapse, likely contribute to tsunamigenesis, the evidence does not support this being responsible the predominant source mechanism. The hazards implications of this are important, the tsunami traveled faster than expected making characterizing it and communicating the threat to the public very challenging.

This dissertation has shown that the BOOTS slope does not universally

follow a reference power law of  $\omega^{-2}$ . This dissertation found that it experiences substantial seasonal variations in the east Pacific from the Gulf of Alaska down to Peru. The chief contributor to its variation are meteorologically induced IGW events. These events interact with the BOOTS to lower the slope value to be  $< 2$ . In the absence of these events, BOOTS slope values are  $\geq 2$ , with values being closer to 2 in areas outside of the east Pacific. This dissertation proposed that IGW events and their absence may have some interactions with tsunami events that may affect aleatory and epistemic uncertainties for tsunami source models. We have shown that, in addition to extratropical systems in the north and south Pacific, tropical systems in the east Pacific cause IGW events that can be recorded across the Pacific. Finally, this dissertation recommends that automatic detection algorithms take into account IGW events, particularly in the Gulf of Alaska and CSZ, as they may eclipse small tsunami signals.

This dissertation has shown that a strike-slip fault geometry alone is inadequate for generating the tsunami observed following the October 2020 Sand Point, Alaska, earthquake. Using hydrodynamic, static slip, and kinematic slip inversions, this dissertation found that there was likely slip along the megathrust in addition to strike-slip faulting. The sea surface deformation necessary to recreate the tsunami waveforms at the Alaskan and Hawaiian sea level stations, as well as the DART stations, requires slip consistent with the megathrust orientation. The final model suggests that slip on a steeply-dipping strike-slip plane dynamically triggers slip on the megathrust  $\sim 30$  s after event origin time at a location 79

km southwest of the event hypocenter. While the strike-slip plane ruptures at typical speeds (up to 3 km/s), the megathrust likely ruptures at a much slower velocity of 1 km/s. The model results in slip equivalent to a Mw7.6 on the strike-slip plane and Mw7.8 on the megathrust plane, for a cumulative slip equivalent to an Mw7.9 earthquake. It is hypothesized that the slow megathrust rupture does not contribute much seismic radiation— much like the 1946 Sanak earthquake— allowing it to go largely unnoticed in traditional teleseismic response. The rupture front propagates at low velocity into a region of high slip deficit updip of the Mw7.8 Simeonof earthquake but does not slip updip of  $\sim 20$  km. Finally, a submarine landslide is likely necessary to explain the tsunami waveforms at the King Cove coastal sea level station and DART station 46402.

## REFERENCES CITED

- American Society of Civil Engineers. (2022). *Minimum design loads and associated criteria for buildings and other structures*. American Society of Civil Engineers.
- Arai, N., Iwakuni, M., Watada, S., Imanishi, Y., Murayama, T., & Nogami, M. (2011). Atmospheric boundary waves excited by the tsunami generation related to the 2011 great tohoku-oki earthquake. *Geophysical Research Letters*, *38*(7).
- Aster, R., Borchers, B., & Thurber, C. (2018). *Parameter estimation and inverse problems*. Cambridge, MA: Elsevier.
- Atwater, B. F., & Griggs, G. B. (2012). *Deep-sea turbidites as guides to holocene earthquake history at the cascadia subduction zone: Alternative views for a seismic-hazard workshop*. US Department of the Interior, US Geological Survey.
- Aucan, J., & Arduin, F. (2013, July). Infragravity waves in the deep ocean: An upward revision: INFRAGRAVITY WAVES IN THE DEEP OCEAN. *Geophysical Research Letters*, *40*(13), 3435–3439. Retrieved 2023-04-12, from <http://doi.wiley.com/10.1002/grl.50321> doi: 10.1002/grl.50321
- Barnhart, W. D., Murray, J. R., Briggs, R. W., Gomez, F., Miles, C. P., Svarc, J., ... Stressler, B. J. (2016). Coseismic slip and early afterslip of the 2015 Illapel, Chile, earthquake: Implications for frictional heterogeneity and coastal uplift. *Journal of Geophysical Research: Solid Earth*, *121*(8), 6172–6191.

- Bernard, E., & Titov, V. (2015). Evolution of tsunami warning systems and products. *Philosophical Transactions of the Royal Society A: Mathematical, Physical and Engineering Sciences*, 373(2053), 20140371.
- Bertiger, W., Bar-Sever, Y., Dorsey, A., Haines, B., Harvey, N., Hemberger, D., . . . Willis, P. (2020, August). GipsyX/RTGx, a new tool set for space geodetic operations and research. *Advances in Space Research*, 66(3), 469–489. Retrieved 2023-07-02, from <https://linkinghub.elsevier.com/retrieve/pii/S0273117720302532> doi: 10.1016/j.asr.2020.04.015
- Blaylock, B. K. (2024, March). *Herbie: Retrieve Numerical Weather Prediction Model Data*. Zenodo. Retrieved from <https://doi.org/10.5281/zenodo.10759470> doi: 10.5281/zenodo.10759470
- Blaylock, B. K., Horel, J. D., & Liston, S. T. (2017). Cloud archiving and data mining of High-Resolution Rapid Refresh forecast model output. *Computers & Geosciences*, 109, 43–50. Retrieved from <https://www.sciencedirect.com/science/article/pii/S0098300417305083> doi: <https://doi.org/10.1016/j.cageo.2017.08.005>
- Blom, P. S., Dannemann, F. K., & Marcillo, O. E. (2018). Bayesian characterization of explosive sources using infrasonic signals. *Geophysical Journal International*, 215(1), 240–251.

- Bécel, A., Shillington, D. J., Delescluse, M., Nedimović, M. R., Abers, G., Saffer, D. M., ... Kuehn, H. (2017, August). Tsunamigenic structures in a creeping section of the Alaska subduction zone. *Nature Geoscience*, *10*(8), 609–613. Retrieved 2022-12-14, from <http://www.nature.com/articles/ngeo2990> doi: 10.1038/ngeo2990
- Carvajal, M., Sepúlveda, I., Gubler, A., & Garreaud, R. (2022). Worldwide signature of the 2022 tonga volcanic tsunami. *Geophysical Research Letters*, *49*(6), e2022GL098153.
- Clawpack Development Team. (2020, September). *Clawpack version 5.7.1*. Zenodo. Retrieved from <https://doi.org/10.5281/zenodo.4025432> doi: 10.5281/zenodo.4025432
- Cooperative Institute for Research in Environmental Sciences. (n.d.). *Continuously Updated Digital Elevation Model (CUDEM) - 1/9 Arc-Second Resolution Bathymetric-Topographic Tiles*. NOAA National Centers for Environmental Information. Retrieved 2024-07-26, from <https://www.ncei.noaa.gov/metadata/geoportal/rest/metadata/item/gov.noaa.ngdc.mgg.dem:999919/html> doi: 10.25921/DS9V-KY35
- Crowell, B. W., & Melgar, D. (2020, October). Slipping the Shumagin Gap: A Kinematic Coseismic and Early Afterslip Model of the Mw 7.8 Simeonof Island, Alaska, Earthquake. *Geophysical Research Letters*, *47*(19). Retrieved 2022-12-14, from <https://onlinelibrary.wiley.com/doi/10.1029/2020GL090308> doi: 10.1029/2020GL090308

- D'Amico, S., Orecchio, B., Presti, D., Gervasi, A., Zhu, L., Guerra, I., ...  
Herrmann, R. (2011). Testing the Stability of Moment Tensor Solutions for  
Small Earthquakes in the Calabro-Peloritan Arc Region (Southern Italy).  
Retrieved 2023-03-02, from <https://doi.org/10.4430/bgta0009> doi:  
10.4430/bgta0009
- Davies, J., Sykes, L., House, L., & Jacob, K. (1981). Shumagin Seismic Gap,  
Alaska Peninsula: History of great earthquakes, tectonic setting, and  
evidence for high seismic potential. *Journal of Geophysical Research*,  
86(B5), 3821. Retrieved 2022-12-14, from  
<http://doi.wiley.com/10.1029/JB086iB05p03821> doi:  
10.1029/JB086iB05p03821
- Deep-ocean assessment and reporting of tsunamis (dart(r))* [dataset]. (2005).  
NOAA National Centers for Environmental Information. Retrieved from  
<https://www.ngdc.noaa.gov/hazard/dart/> (Accessed: 2024/02/24) doi:  
10.7289/V5F18WNS
- DeSanto, J. B., Webb, S. C., Nooner, S. L., Schmidt, D. A., Crowell, B. W.,  
Brooks, B. A., ... Chadwell, C. D. (2023, August). Limited Shallow Slip for  
the 2020 Simeonof Earthquake, Alaska, Constrained by GNSS-Acoustic.  
*Geophysical Research Letters*, 50(16), e2023GL105045. Retrieved  
2023-10-26, from  
<https://agupubs.onlinelibrary.wiley.com/doi/10.1029/2023GL105045>  
doi: 10.1029/2023GL105045

DOC/NOAA/NOS/CO-OPS ; Center for Operational Oceanographic Products and Services, National Ocean Service, NOAA, U.S. Department of Commerce. (2007). *CO-OPS 1-minute tsunami water level data*. NOAA National Centers for Environmental Information.

Eungard, D., Forson, C., Walsh, T., Gica, E., & Arcas, D. (2018). *Tsunami hazard maps of southwest washington—model results from a ~ 2,500-year cascadia subduction zone earthquake scenario: Washington geological survey map series 2018-01, originally published march 2018, 6 sheets, scale 1: 48,000, 11 p. text*. March.

Filloux, J. H., Luther, D., & Chave, A. (1991). Long-term seafloor measurement of water pressure: Normal modes and infragravity waves. *Proceedings of the XXth General Assembly IUGG*.

Flanders Marine Institute (VLIZ), Belgium, & Intergovernmental Oceanographic Commission-UNESCO, France. (2021). *Sea level station monitoring facility*. VLIZ.

Frankel, A., Chen, R., Petersen, M., Moschetti, M., & Sherrod, B. (2015). 2014 update of the pacific northwest portion of the us national seismic hazard maps. *Earthquake Spectra*, *31*(1\_suppl), S131–S148.

Fujii, Y., Satake, K., Sakai, S., Shinohara, M., & Kanazawa, T. (2011). Tsunami source of the 2011 off the pacific coast of tohoku earthquake. *Earth, planets and space*, *63*, 815–820.

Geist, E. L., & Parsons, T. (2006). Probabilistic analysis of tsunami hazards. *Natural Hazards*, *37*, 277–314.

- Goda, K. (2022). Stochastic source modeling and tsunami simulations of cascadia subduction earthquakes for canadian pacific coast. *Coastal Engineering Journal*, 64(4), 575–596.
- Goldberg, D. E., Koch, P., Melgar, D., Riquelme, S., & Yeck, W. L. (2022, November). Beyond the Teleseism: Introducing Regional Seismic and Geodetic Data into Routine USGS Finite-Fault Modeling. *Seismological Research Letters*, 93(6), 3308–3323. Retrieved 2022-12-12, from <https://pubs.geoscienceworld.org/srl/article/93/6/3308/615951/Beyond-the-Teleseism-Introducing-Regional-Seismic> doi: 10.1785/0220220047
- Goldberg, D. E., & Melgar, D. (2020). Generation and validation of broadband synthetic p waves in semistochastic models of large earthquakes. *Bulletin of the Seismological Society of America*, 110(4), 1982–1995.
- Goldfinger, C., Galer, S., Beeson, J., Hamilton, T., Black, B., Romsos, C., . . . Morey, A. (2017). The importance of site selection, sediment supply, and hydrodynamics: A case study of submarine paleoseismology on the northern cascadia margin, washington usa. *Marine Geology*, 384, 4–46.
- Goldfinger, C., Nelson, C. H., Morey, A. E., Johnson, J. E., Patton, J. R., Karabanov, E. B., . . . others (2012). *Turbidite event history—methods and implications for holocene paleoseismicity of the cascadia subduction zone* (Tech. Rep.). US Geological Survey.

- Hanafin, J., Quilfen, Y., Arduin, F., Vandemark, D., Chapron, B., Feng, H., . . . others (2012). Phenomenal sea states and swell radiation: a comprehensive analysis of the 12-16 february 2011 north atlantic storms. *Bull. Amer. Meterol. Soc*, *93*, 1825–1832.
- Harkrider, D., & Press, F. (1967). The krakatoa air—sea waves: an example of pulse propagation in coupled systems. *Geophysical Journal International*, *13*(1-3), 149–159.
- Hayes, G. P. (2017). The finite, kinematic rupture properties of great-sized earthquakes since 1990. *Earth and Planetary Science Letters*, *468*, 94-100. Retrieved from <https://www.sciencedirect.com/science/article/pii/S0012821X17301826> doi: <https://doi.org/10.1016/j.epsl.2017.04.003>
- Hayes, G. P., Moore, G. L., Portner, D. E., Hearne, M., Flamme, H., Furtney, M., & Smoczyk, G. M. (2018, October). Slab2, a comprehensive subduction zone geometry model. *Science*, *362*(6410), 58–61. Retrieved 2022-12-14, from <https://www.science.org/doi/10.1126/science.aat4723> doi: 10.1126/science.aat4723
- Hedlin, M., Walker, K., Drob, D., & de Groot-Hedlin, C. (2012). Infrasound: Connecting the solid earth, oceans, and atmosphere. *Annual Review of Earth and Planetary Sciences*, *40*(1), 327–354.
- Heidarzadeh, M., Gusman, A. R., Ishibe, T., Sabeti, R., & Šepić, J. (2022). Estimating the eruption-induced water displacement source of the 15 january 2022 tonga volcanic tsunami from tsunami spectra and numerical modelling. *Ocean Engineering*, *261*, 112165.

- Herman, M. W., & Furlong, K. P. (2021, March). Triggering an unexpected earthquake in an uncoupled subduction zone. *Science Advances*, 7(13), eabf7590. Retrieved 2022-12-14, from <https://www.science.org/doi/10.1126/sciadv.abf7590> doi: 10.1126/sciadv.abf7590
- Herring, T. A., Melbourne, T. I., Murray, M. H., Floyd, M. A., Szeliga, W. M., King, R. W., . . . Wang, L. (2016, December). Plate Boundary Observatory and related networks: GPS data analysis methods and geodetic products. *Reviews of Geophysics*, 54(4), 759–808. Retrieved 2023-12-01, from <https://agupubs.onlinelibrary.wiley.com/doi/10.1002/2016RG000529> doi: 10.1002/2016RG000529
- Jaccard, P. (1912). The distribution of the flora in the alpine zone. 1. *New phytologist*, 11(2), 37–50.
- Ji, C., Wald, D. J., & Helmberger, D. V. (2002, May). Source Description of the 1999 Hector Mine, California, Earthquake, Part I: Wavelet Domain Inversion Theory and Resolution Analysis. *Bulletin of the Seismological Society of America*, 92(4), 1192–1207. Retrieved 2022-12-12, from <https://pubs.geoscienceworld.org/bssa/article/92/4/1192-1207/120765> doi: 10.1785/0120000916
- Jia, Z., Zhan, Z., & Kanamori, H. (2022, February). The 2021 South Sandwich Island  $M_w$  8.2 Earthquake: A Slow Event Sandwiched Between Regular Ruptures. *Geophysical Research Letters*, 49(3). Retrieved 2022-12-14, from <https://onlinelibrary.wiley.com/doi/10.1029/2021GL097104> doi: 10.1029/2021GL097104

- Kalnay, E. (2002). *Atmospheric modeling, data assimilation and predictability*. Cambridge University Press.
- Kelsey, H. M., Nelson, A. R., Hemphill-Haley, E., & Witter, R. C. (2005). Tsunami history of an oregon coastal lake reveals a 4600 yr record of great earthquakes on the cascadia subduction zone. *Geological Society of America Bulletin*, 117(7-8), 1009–1032.
- Koch, P., Bravo, F., Riquelme, S., & Crempien, J. G. F. (2019, August). Near-Real-Time Finite-Fault Inversions for Large Earthquakes in Chile Using Strong-Motion Data. *Seismological Research Letters*. Retrieved 2022-12-12, from <https://pubs.geoscienceworld.org/ssa/srl/article/573077/NearRealTime-FiniteFault-Inversions-for-Large> doi: 10.1785/0220180294
- Kohler, M. D., Bowden, D. C., Ampuero, J.-P., & Shi, J. (2020). Globally scattered 2011 tohoku tsunami waves from a seafloor sensor array in the northeast pacific ocean. *Journal of Geophysical Research: Solid Earth*, 125(11), e2020JB020221.
- Kubota, T., Saito, T., & Nishida, K. (2022). Global fast-traveling tsunamis driven by atmospheric lamb waves on the 2022 tonga eruption. *Science*, 377(6601), 91–94.
- Kulikov, E. A., Rabinovich, A. B., Spirin, A. I., Poole, S. L., & Soloviev, S. L. (1983, January). Measurement of tsunamis in the open ocean. *Marine Geodesy*, 6(3-4), 311–329. Retrieved 2023-09-22, from <http://www.tandfonline.com/doi/abs/10.1080/15210608309379465> doi: 10.1080/15210608309379465

- Larson, K. M., Lay, T., Yamazaki, Y., Cheung, K. F., Ye, L., Williams, S. D., & Davis, J. L. (2021, February). Dynamic Sea Level Variation From GNSS: 2020 Shumagin Earthquake Tsunami Resonance and Hurricane Laura. *Geophysical Research Letters*, *48*(4). Retrieved 2022-12-14, from <https://onlinelibrary.wiley.com/doi/10.1029/2020GL091378> doi: 10.1029/2020GL091378
- La Selle, S. M., Nelson, A. R., Witter, R. C., Jaffe, B. E., Gelfenbaum, G., & Padgett, J. S. (2024). Testing megathrust rupture models using tsunami deposits. *Journal of Geophysical Research: Earth Surface*, *129*(5), e2023JF007444.
- LeVeque, R. J., George, D. L., & Berger, M. J. (2011, May). Tsunami modelling with adaptively refined finite volume methods. *Acta Numerica*, *20*, 211–289. Retrieved 2022-12-14, from [https://www.cambridge.org/core/product/identifier/S0962492911000043/type/journal\\_article](https://www.cambridge.org/core/product/identifier/S0962492911000043/type/journal_article) doi: 10.1017/S0962492911000043
- LeVeque, R. J., Waagan, K., González, F. I., Rim, D., & Lin, G. (2017). Generating random earthquake events for probabilistic tsunami hazard assessment. *Global Tsunami Science: Past and Future, Volume I*, 3671–3692.
- Li, S., & Freymueller, J. T. (2018, April). Spatial Variation of Slip Behavior Beneath the Alaska Peninsula Along Alaska-Aleutian Subduction Zone. *Geophysical Research Letters*, *45*(8), 3453–3460. Retrieved 2022-12-14, from <http://doi.wiley.com/10.1002/2017GL076761> doi: 10.1002/2017GL076761

- Li, S., Wang, K., Wang, Y., Jiang, Y., & Dosso, S. E. (2018). Geodetically inferred locking state of the cascadia megathrust based on a viscoelastic earth model. *Journal of Geophysical Research: Solid Earth*, *123*(9), 8056–8072.
- Lin, J.-T., Aslam, K. S., Thomas, A. M., & Melgar, D. (2020, August). Overlapping regions of coseismic and transient slow slip on the Hawaiian décollement. *Earth and Planetary Science Letters*, *544*, 116353. Retrieved 2022-12-14, from <https://linkinghub.elsevier.com/retrieve/pii/S0012821X20302971> doi: 10.1016/j.epsl.2020.116353
- Liu, C., Lay, T., & Xiong, X. (2022, February). The 29 July 2021  $M_w$  8.2 Chignik, Alaska Peninsula Earthquake Rupture Inferred From Seismic and Geodetic Observations: Re-Rupture of the Western 2/3 of the 1938 Rupture Zone. *Geophysical Research Letters*, *49*(4). Retrieved 2023-02-09, from <https://onlinelibrary.wiley.com/doi/10.1029/2021GL096004> doi: 10.1029/2021GL096004
- Loveless, J. P., & Meade, B. J. (2015). Kinematic barrier constraints on the magnitudes of additional great earthquakes off the east coast of japan. *Seismological Research Letters*, *86*(1), 202–209.
- López, A. M., & Okal, E. A. (2006, June). A seismological reassessment of the source of the 1946 Aleutian ‘tsunami’ earthquake. *Geophysical Journal International*, *165*(3), 835–849. Retrieved 2023-02-03, from <https://academic.oup.com/gji/article-lookup/doi/10.1111/j.1365-246X.2006.02899.x> doi: 10.1111/j.1365-246X.2006.02899.x

- Ma, S., & Nie, S. (2019, August). Dynamic Wedge Failure and Along-Arc Variations of Tsunamigenesis in the Japan Trench Margin. *Geophysical Research Letters*, *46*(15), 8782–8790. Retrieved 2023-02-09, from <https://onlinelibrary.wiley.com/doi/abs/10.1029/2019GL083148> doi: 10.1029/2019GL083148
- Mai, P. M., & Thingbaijam, K. K. S. (2014, October). SRCMOD: An Online Database of Finite-Fault Rupture Models. *Seismological Research Letters*, *85*(6), 1348–1357. Retrieved from <https://doi.org/10.1785/0220140077> (eprint: <https://pubs.geoscienceworld.org/ssa/srl/article-pdf/85/6/1348/2769875/1348.pdf>) doi: 10.1785/0220140077
- Matoza, R. S., Fee, D., Assink, J. D., Iezzi, A. M., Green, D. N., Kim, K., . . . others (2022). Atmospheric waves and global seismoacoustic observations of the january 2022 hunga eruption, tonga. *Science*, *377*(6601), 95–100.
- McNamara, D. E., & Buland, R. (2004, August). Ambient Noise Levels in the Continental United States. *Bulletin of the Seismological Society of America*, *94*(4), 1517–1527. Retrieved 2023-09-25, from <https://pubs.geoscienceworld.org/bssa/article/94/4/1517-1527/121021> doi: 10.1785/012003001
- Melgar, D. (2021). Was the january 26th, 1700 cascadia earthquake part of a rupture sequence? *Journal of Geophysical Research: Solid Earth*, *126*(10), e2021JB021822.

Melgar, D., & Bock, Y. (2013, November). Near-field tsunami models with rapid earthquake source inversions from land- and ocean-based observations: The potential for forecast and warning: TSUNAMI MODELS WITH RAPID INVERSIONS. *Journal of Geophysical Research: Solid Earth*, *118*(11), 5939–5955. Retrieved 2022-12-14, from <http://doi.wiley.com/10.1002/2013JB010506> doi: 10.1002/2013JB010506

Melgar, D., & Bock, Y. (2015, May). Kinematic earthquake source inversion and tsunami runup prediction with regional geophysical data: MELGAR AND BOCK. *Journal of Geophysical Research: Solid Earth*, *120*(5), 3324–3349. Retrieved 2022-12-14, from <http://doi.wiley.com/10.1002/2014JB011832> doi: 10.1002/2014JB011832

Melgar, D., Fan, W., Riquelme, S., Geng, J., Liang, C., Fuentes, M., . . . Fielding, E. J. (2016, February). Slip segmentation and slow rupture to the trench during the 2015,  $M_w$  8.3 Illapel, Chile earthquake. *Geophysical Research Letters*, *43*(3), 961–966. Retrieved 2022-12-14, from <https://onlinelibrary.wiley.com/doi/10.1002/2015GL067369> doi: 10.1002/2015GL067369

Melgar, D., LeVeque, R. J., Dreger, D. S., & Allen, R. M. (2016). Kinematic rupture scenarios and synthetic displacement data: An example application to the cascadia subduction zone. *Journal of Geophysical Research: Solid Earth*, *121*(9), 6658–6674.

Melgar, D., & Ruiz-Angulo, A. (2018). Long-lived tsunami edge waves and shelf resonance from the m8. 2 tehuantepec earthquake. *Geophysical Research Letters*, *45*(22), 12–414.

- Melgar, D., Williamson, A. L., & Salazar-Monroy, E. F. (2019). Differences between heterogenous and homogenous slip in regional tsunami hazards modelling. *Geophysical Journal International*, *219*(1), 553–562.
- Métois, M., Socquet, A., Vigny, C., Carrizo, D., Peyrat, S., Delorme, A., . . . Ortega, I. (2013). Revisiting the north chile seismic gap segmentation using gps-derived interseismic coupling. *Geophysical Journal International*, *194*(3), 1283–1294.
- Montserrat, S., Vilibić, I., & Rabinovich, A. B. (2006). Meteotsunamis: atmospherically induced destructive ocean waves in the tsunami frequency band. *Natural hazards and earth system sciences*, *6*(6), 1035–1051.
- Mori, N., Satake, K., Cox, D., Goda, K., Catalan, P. A., Ho, T.-C., . . . others (2022). Giant tsunami monitoring, early warning and hazard assessment. *Nature Reviews Earth & Environment*, *3*(9), 557–572.
- Mori, N., Takahashi, T., Yasuda, T., & Yanagisawa, H. (2011). Survey of 2011 tohoku earthquake tsunami inundation and run-up. *Geophysical research letters*, *38*(7).
- National geophysical data center / world data service: Ncei/wds global historical tsunami database* [dataset]. (n.d.). NOAA National Centers for Environmental Information. (Accessed: 2024/03/14) doi: 10.7289/V5PN93H7

- Nelson, A. R., DuRoss, C. B., Witter, R. C., Kelsey, H. M., Engelhart, S. E., Mahan, S. A., . . . Padgett, J. S. (2021). A maximum rupture model for the central and southern cascadia subduction zone—reassessing ages for coastal evidence of megathrust earthquakes and tsunamis. *Quaternary Science Reviews*, *261*, 106922.
- Newman, A. V., Hayes, G., Wei, Y., & Convers, J. (2011, March). The 25 October 2010 Mentawai tsunami earthquake, from real-time discriminants, finite-fault rupture, and tsunami excitation: THE 2010 MENTAWAI TSUNAMI EARTHQUAKE. *Geophysical Research Letters*, *38*(5), n/a–n/a. Retrieved 2023-06-14, from <http://doi.wiley.com/10.1029/2010GL046498> doi: 10.1029/2010GL046498
- Nishida, K., Kobayashi, N., & Fukao, Y. (2014). Background lamb waves in the earth's atmosphere. *Geophysical Journal International*, *196*(1), 312–316.
- NOAA National Geophysical Data Center. (n.d.). *2010: Crescent city, california 1/3 arc-second mhw coastal digital elevation model*. NOAA National Centers for Environmental Information.
- Nomanbhoy, N., & Satake, K. (1995). Generation mechanism of tsunamis from the 1883 Krakatau eruption. *Geophysical Research Letters*, *22*(4), 509–512.
- Okada, Y. (1985). Surface deformation due to shear and tensile faults in a half-space. *Bulletin of the Seismological Society of America*, *75*(4), 1135–1154. doi: <https://doi.org/10.1785/BSSA0750041135>
- Okal, E. A., & Synolakis, C. E. (2003). A theoretical comparison of tsunamis from dislocations and landslides. *Pure and applied geophysics*, *160*, 2177–2188.

- Pararas-Carayannis, G. (2003). Near and far-field effects of tsunamis generated by the paroxysmal eruptions, explosions, caldera collapses and massive slope failures of the krakatau volcano in indonesia on august 26-27, 1883. *Science of Tsunami Hazards*.
- Paris, R., Wassmer, P., Lavigne, F., Belousov, A., Belousova, M., Iskandarsyah, Y., ... Mazzoni, N. (2014). Coupling eruption and tsunami records: the krakatau 1883 case study, indonesia. *Bulletin of Volcanology*, 76, 1–23.
- Pasyanos, M. E., Masters, T. G., Laske, G., & Ma, Z. (2014, March). LITHO1.0: An updated crust and lithospheric model of the Earth. *Journal of Geophysical Research: Solid Earth*, 119(3), 2153–2173. Retrieved 2022-12-14, from <https://onlinelibrary.wiley.com/doi/abs/10.1002/2013JB010626>  
doi: 10.1002/2013JB010626
- Perfettini, H., Avouac, J.-P., Tavera, H., Kositsky, A., Nocquet, J.-M., Bondoux, F., ... others (2010). Seismic and aseismic slip on the central peru megathrust. *Nature*, 465(7294), 78–81.
- Petersen, M. D., Shumway, A. M., Powers, P. M., Field, E. H., Moschetti, M. P., Jaiswal, K. S., ... others (2024). The 2023 us 50-state national seismic hazard model: Overview and implications. *Earthquake Spectra*, 40(1), 5–88.
- Press, F., & Harkrider, D. (1966). Air-sea waves from the explosion of krakatoa. *Science*, 154(3754), 1325–1327.
- Priest, G. R. (1995). *Explanation of mapping methods and use of the tsunami hazard maps of the oregon coast* (No. 0-67). State of Oregon, Department of Geology and Mineral Industries.

- Priest, G. R., & Allan, J. C. (2019). *Comparison of oregon tsunami hazard scenarios to a probabilistic tsunami hazard analysis (ptha)*. Oregon Department of Geology and Mineral Industries.
- Prieto, G. A. (2022, May). The *Multitaper* Spectrum Analysis Package in Python. *Seismological Research Letters*, *93*(3), 1922–1929. Retrieved 2023-09-25, from <https://pubs.geoscienceworld.org/srl/article/93/3/1922/612834/The-Multitaper-Spectrum-Analysis-Package-in-Python> doi: 10.1785/0220210332
- Prieto, G. A., Parker, R. L., & Vernon Iii, F. (2009). A fortran 90 library for multitaper spectrum analysis. *Computers & Geosciences*, *35*(8), 1701–1710.
- Rabinovich, A. B. (1997, June). Spectral analysis of tsunami waves: Separation of source and topography effects. *Journal of Geophysical Research: Oceans*, *102*(C6), 12663–12676. Retrieved 2023-09-21, from <https://agupubs.onlinelibrary.wiley.com/doi/10.1029/97JC00479> doi: 10.1029/97JC00479
- Rabinovich, A. B., Candella, R. N., & Thomson, R. E. (2011, November). Energy Decay of the 2004 Sumatra Tsunami in the World Ocean. *Pure and Applied Geophysics*, *168*(11), 1919–1950. Retrieved 2022-11-18, from <http://link.springer.com/10.1007/s00024-011-0279-1> doi: 10.1007/s00024-011-0279-1

- Rabinovich, A. B., Candella, R. N., & Thomson, R. E. (2013, June). The open ocean energy decay of three recent trans-Pacific tsunamis: TSUNAMI ENERGY DECAY. *Geophysical Research Letters*, *40*(12), 3157–3162. Retrieved 2022-11-18, from <http://doi.wiley.com/10.1002/grl.50625> doi: 10.1002/grl.50625
- Rabinovich, A. B., & Eblé, M. C. (2015, December). Deep-Ocean Measurements of Tsunami Waves. *Pure and Applied Geophysics*, *172*(12), 3281–3312. Retrieved 2023-09-22, from <http://link.springer.com/10.1007/s00024-015-1058-1> doi: 10.1007/s00024-015-1058-1
- Rawat, A., Ardhuin, F., Ballu, V., Crawford, W., Corela, C., & Aucan, J. (2014, November). Infragravity waves across the oceans: Following Infra-Gravity Wave Bursts. *Geophysical Research Letters*, *41*(22), 7957–7963. Retrieved 2023-04-12, from <http://doi.wiley.com/10.1002/2014GL061604> doi: 10.1002/2014GL061604
- Revelle, D. O., & Whitaker, R. (1996). *Lamb waves from airborne explosion sources: Viscous effects and comparisons to ducted acoustic arrivals* (Tech. Rep.). Los Alamos National Lab.(LANL), Los Alamos, NM (United States).
- Riquelme, S., Schwarze, H., Fuentes, M., & Campos, J. (2020, June). Near-Field Effects of Earthquake Rupture Velocity Into Tsunami Runup Heights. *Journal of Geophysical Research: Solid Earth*, *125*(6). Retrieved 2023-06-12, from <https://onlinelibrary.wiley.com/doi/10.1029/2019JB018946> doi: 10.1029/2019JB018946

- Ruppert Jr, J. H., Koch, S. E., Chen, X., Du, Y., Seimon, A., Sun, Y. Q., . . .  
Bosart, L. F. (2022). Mesoscale gravity waves and midlatitude weather: A  
tribute to fuqing zhang. *Bulletin of the American Meteorological Society*,  
*103*(1), E129–E156.
- Sahakian, V., Melgar, D., & Muzli, M. (2019, August). Weak Near-Field Behavior  
of a Tsunami Earthquake: Toward Real-Time Identification for Local  
Warning. *Geophysical Research Letters*, *46*(16), 9519–9528. Retrieved  
2022-12-14, from  
<https://onlinelibrary.wiley.com/doi/10.1029/2019GL083989> doi:  
10.1029/2019GL083989
- Saito, T., Inazu, D., Miyoshi, T., & Hino, R. (2014). Dispersion and nonlinear  
effects in the 2011 tohoku-oki earthquake tsunami. *Journal of Geophysical  
Research: Oceans*, *119*(8), 5160–5180.
- Santellanes, S. R. (2024, March). *ssantellanes/BOOTS: v1.0.0*. Zenodo. Retrieved  
from <https://doi.org/10.5281/zenodo.10835239> doi:  
<https://doi.org/10.5281/zenodo.10835239>
- Satake, K., Wang, K., & Atwater, B. F. (2003). Fault slip and seismic moment of  
the 1700 cascadia earthquake inferred from japanese tsunami descriptions.  
*Journal of Geophysical Research: Solid Earth*, *108*(B11).
- Schmalzle, G. M., McCaffrey, R., & Creager, K. C. (2014). Central cascadia  
subduction zone creep. *Geochemistry, Geophysics, Geosystems*, *15*(4),  
1515–1532.

- Small, D. T., & Melgar, D. (2021). Geodetic coupling models as constraints on stochastic earthquake ruptures: An example application to ptha in cascadia. *Journal of Geophysical Research: Solid Earth*, 126(7), e2020JB021149.
- Small, D. T., & Melgar, D. (2023). Can stochastic slip rupture modeling produce realistic m9+ events? *Journal of Geophysical Research: Solid Earth*, 128(3), e2022JB025716.
- Tanioka, Y., Ruff, L., & Satake, K. (1997, September). What controls the lateral variation of large earthquake occurrence along the Japan Trench? *The Island Arc*, 6(3), 261–266. Retrieved 2023-02-09, from <https://onlinelibrary.wiley.com/doi/10.1111/j.1440-1738.1997.tb00176.x>  
doi: 10.1111/j.1440-1738.1997.tb00176.x
- Ten Brink, U. S., Geist, E. L., & Andrews, B. D. (2006, June). Size distribution of submarine landslides and its implication to tsunami hazard in Puerto Rico. *Geophysical Research Letters*, 33(11), 2006GL026125. Retrieved 2023-06-13, from <https://onlinelibrary.wiley.com/doi/10.1029/2006GL026125>  
doi: 10.1029/2006GL026125
- Thio, H. K., & Somerville, P. (2009). A probabilistic tsunami hazard analysis of california. In *Tclee 2009* (p. 1-12). ASCE. Retrieved from <https://ascelibrary.org/doi/abs/10.1061/41050%28357%2957> doi: 10.1061/41050(357)57

- Titov, V. V., Gonzalez, F. I., Bernard, E. N., Eble, M. C., Mofjeld, H. O., Newman, J. C., & Venturato, A. J. (2005, May). Real-Time Tsunami Forecasting: Challenges and Solutions. *Natural Hazards*, *35*(1), 35–41. Retrieved 2022-12-14, from <http://link.springer.com/10.1007/s11069-004-2403-3> doi: 10.1007/s11069-004-2403-3
- Tozer, B., Sandwell, D. T., Smith, W. H. F., Olson, C., Beale, J. R., & Wessel, P. (2019, October). Global Bathymetry and Topography at 15 Arc Sec: SRTM15+. *Earth and Space Science*, *6*(10), 1847–1864. Retrieved 2023-12-01, from <https://agupubs.onlinelibrary.wiley.com/doi/10.1029/2019EA000658> doi: 10.1029/2019EA000658
- Tsai, V. C., Ampuero, J.-P., Kanamori, H., & Stevenson, D. J. (2013, February). Estimating the effect of Earth elasticity and variable water density on tsunami speeds: ELASTIC COMPRESSIBLE TSUNAMI SPEED. *Geophysical Research Letters*, *40*(3), 492–496. Retrieved 2022-12-14, from <http://doi.wiley.com/10.1002/grl.50147> doi: 10.1002/grl.50147
- Tsushima, H., Hino, R., Fujimoto, H., Tanioka, Y., & Imamura, F. (2009, June). Near-field tsunami forecasting from cabled ocean bottom pressure data. *Journal of Geophysical Research*, *114*(B6), B06309. Retrieved 2022-12-14, from <http://doi.wiley.com/10.1029/2008JB005988> doi: 10.1029/2008JB005988

- U. S. Geological Survey. (2017). *Advanced National Seismic System (ANSS) Comprehensive Catalog*. Retrieved 2023-07-24, from <http://earthquake.usgs.gov/earthquakes/search/> (Publisher: U.S. Geological Survey) doi: 10.5066/F7MS3QZH
- Villegas-Lanza, J. C., Chlieh, M., Cavalié, O., Tavera, H., Baby, P., Chire-Chira, J., & Nocquet, J.-M. (2016). Active tectonics of peru: Heterogeneous interseismic coupling along the nazca megathrust, rigid motion of the peruvian sliver, and subandean shortening accommodation. *Journal of Geophysical Research: Solid Earth*, *121*(10), 7371–7394.
- Walton, M. A., Staisch, L. M., Dura, T., Pearl, J. K., Sherrod, B., Gomberg, J., ... others (2021). Toward an integrative geological and geophysical view of cascadia subduction zone earthquakes. *Annual Review of Earth and Planetary Sciences*, *49*(1), 367–398.
- Watada, S. (2009). Radiation of acoustic and gravity waves and propagation of boundary waves in the stratified fluid from a time-varying bottom boundary. *Journal of fluid mechanics*, *627*, 361–377.
- Watada, S., & Kanamori, H. (2010). Acoustic resonant oscillations between the atmosphere and the solid earth during the 1991 mt. pinatubo eruption. *Journal of Geophysical Research: Solid Earth*, *115*(B12).
- Webb, S. C., Zhang, X., & Crawford, W. (1991, February). Infragravity waves in the deep ocean. *Journal of Geophysical Research: Oceans*, *96*(C2), 2723–2736. Retrieved 2022-11-22, from <http://doi.wiley.com/10.1029/90JC02212> doi: 10.1029/90JC02212

- Williamson, A., Melgar, D., & Rim, D. (2019, November). The Effect of Earthquake Kinematics on Tsunami Propagation. *Journal of Geophysical Research: Solid Earth*, *124*(11), 11639–11650. Retrieved 2022-12-14, from <https://onlinelibrary.wiley.com/doi/10.1029/2019JB017522> doi: 10.1029/2019JB017522
- Williamson, A. L., Melgar, D., Xu, X., & Milliner, C. (2020). The 2018 palu tsunami: Coeval landslide and coseismic sources. *Seismological Research Letters*, *91*(6), 3148–3160.
- Witter, R. C., Briggs, R. W., Engelhart, S. E., Gelfenbaum, G., Koehler, R. D., & Barnhart, W. D. (2014, April). Little late Holocene strain accumulation and release on the Aleutian megathrust below the Shumagin Islands, Alaska. *Geophysical Research Letters*, *41*(7), 2359–2367. Retrieved 2022-12-14, from <http://doi.wiley.com/10.1002/2014GL059393> doi: 10.1002/2014GL059393
- Witter, R. C., Zhang, Y., Wang, K., Priest, G. R., Goldfinger, C., Stimely, L. L., ... Ferro, P. A. (2011). Simulating tsunami inundation at bandon, coos county, oregon, using hypothetical cascadia and alaska earthquake scenarios. *Oregon department of geology and mineral industries special paper*, *43*, 57.

- Witter, R. C., Zhang, Y. J., Wang, K., Priest, G. R., Goldfinger, C., Stimely, L., . . . Ferro, P. A. (2013, December). Simulated tsunami inundation for a range of Cascadia megathrust earthquake scenarios at Bandon, Oregon, USA. *Geosphere*, 9(6), 1783–1803. Retrieved from <https://doi.org/10.1130/GES00899.1> (eprint: <https://pubs.geoscienceworld.org/gsa/geosphere/article-pdf/9/6/1783/3346666/1783.pdf>) doi: 10.1130/GES00899.1
- Xiao, Z., Freymueller, J. T., Grapenthin, R., Elliott, J. L., Drooff, C., & Fusso, L. (2021, December). The deep Shumagin gap filled: Kinematic rupture model and slip budget analysis of the 2020 Mw 7.8 Simeonof earthquake constrained by GNSS, global seismic waveforms, and floating InSAR. *Earth and Planetary Science Letters*, 576, 117241. Retrieved 2022-12-14, from <https://linkinghub.elsevier.com/retrieve/pii/S0012821X21004970> doi: 10.1016/j.epsl.2021.117241
- Ye, L., Lay, T., Kanamori, H., & Rivera, L. (2016). Rupture characteristics of major and great (m7.0) megathrust earthquakes from 1990 to 2015: 1. source parameter scaling relationships. *Journal of Geophysical Research: Solid Earth*, 121(2), 826-844. Retrieved from <https://agupubs.onlinelibrary.wiley.com/doi/abs/10.1002/2015JB012426> doi: <https://doi.org/10.1002/2015JB012426>

- Yeck, W. L., Shelly, D. R., Materna, K. Z., Goldberg, D. E., & Earle, P. S. (2023, March). Dense geophysical observations reveal a triggered, concurrent multi-fault rupture at the Mendocino Triple Junction. *Communications Earth & Environment*, *4*(1), 94. Retrieved 2023-04-06, from <https://www.nature.com/articles/s43247-023-00752-2> doi: 10.1038/s43247-023-00752-2
- Yokoyama, I. (1987). A scenario of the 1883 Krakatau tsunami. *Journal of Volcanology and Geothermal Research*, *34*(1-2), 123–132.
- Yue, H., Lay, T., Li, L., Yamazaki, Y., Cheung, K. F., Rivera, L., . . . Muhari, A. (2015, March). Validation of linearity assumptions for using tsunami waveforms in joint inversion of kinematic rupture models: Application to the 2010 Mentawai  $M_w$  7.8 tsunami earthquake. *Journal of Geophysical Research: Solid Earth*, *120*(3), 1728–1747. Retrieved 2022-12-14, from <http://doi.wiley.com/10.1002/2014JB011721> doi: 10.1002/2014JB011721
- Yuen, D. A., Scruggs, M. A., Spera, F. J., Zheng, Y., Hu, H., McNutt, S. R., . . . others (2022). Under the surface: Pressure-induced planetary-scale waves, volcanic lightning, and gaseous clouds caused by the submarine eruption of Hunga Tonga-Hunga Ha'apai volcano. *Earthquake Research Advances*, *2*(3), 100134.